# THE EFFECTS OF TERRAIN ON LANDFALLING TROPICAL CYCLONES: AN MM5 SIMULATION OF TYPHOON HERB (1996)

by

DAVID BRYAN RADELL, B.S.

A THESIS

IN

ATMOSPHERIC SCIENCE

Submitted to the Graduate Faculty
of Texas Tech University in
Partial Fulfillment of
the Requirements for
the Degree of

MASTER OF SCIENCE

Approved

Dean of the Graduate School

August, 2001

ACKNOWLEDGEMENTS

I owe a debt of gratitude to Dr. Chia-Bo Chang, whose support and guidance was instrumental in the completion of this project. I also thank committee members Drs. Richard E. Peterson and Arthur L. Doggett IV for their insightful comments which vastly improved the overall quality of this work. Also, Dr. C.-C. Wu of National Taiwan University is thanked for providing the MM5 output, on which this study is based.

I am also thankful to my parents, David and Susan Radell whose constant support in all my endeavors has provided me motivation and encouragement to persevere.

Finally, I wish to thank my student colleagues in the Atmospheric Science Group at Texas Tech. In particular, Jason Branz, Kevin Manross and Al Pietrycha have made my time here much more enjoyable. Their professional and personal friendships have made a world of difference.

This work was partially supported by the Texas Higher Education Coordinating Board under Grant 003644-042.

TABLE OF CONTENTS

ACKNOWLEDGEMENTS..... ii

ABSTRACT..... vi

LIST OF FIGURES..... vii

CHAPTER

1. LITERATURE REVIEW..... 1

1.1 Introduction..... 1

1.2 The Early Modeling Years..... 3

1.3 Numerical Simulations of Tropical Tropical Cyclones..... 4

1.4 Vertical Velocity Fields..... 6

1.5 Potential Vorticity Fields..... 8

2. SYNOPTIC OVERVIEW OF HERB..... 13

2.1 Overview..... 13

2.2 Track Analysis..... 14

2.3 Typhoon Translational Speed..... 16

2.4 Surface Pressure and Wind Analysis.. 19

2.5 Precipitation Distribution..... 25

3. THE MESOSCALE MODEL DESIGN AND DESCRIPTION 28

3.1 Background..... 28

3.2 Physics Options for the Simulation.. 29

3.2.1 Cumulus Parameterization..... 30

3.2.2 Planetary Boundary Layer Scheme..... 30

3.2.3 Explicit Moisture Scheme..... 30

3.2.4 Radiation Scheme..... 31

3.3 Preprocessing Programs..... 31

3.4 Vertical Coordinate System..... 36

3.5 Viewing the Output..... 37

4. VERTICAL MOTION ANALYSIS..... 39

4.1 The Conceptual Model..... 39

4.2 Vertical Motion Well Before Landfall..... 42

4.3 Vertical Motion Just Before Landfall..... 53

4.4 Vertical Motion Over Land..... 62

5. POTENTIAL VORTICITY ANALYSIS..... 70

5.1 PV Structure Analysis..... 70

5.1.1 Well Before Landfall..... 70

5.1.2 Just Before Landfall..... 73

5.1.3 Over Land..... 78

5.2 Lee Potential Vorticity Generation.. 80

5.2.1 Horizontal Cross Section Analysis..... 80

5.2.2 Probing the Positive PV Generation..... 95

5.2.3 Graphical Analysis of PV Generation..... 99

5.2.4 Static Stability and PV Generation..... 107

6. CONCLUSIONS AND RECOMMENDATIONS..... 118

6.1 Conclusions..... 118

6.2 Recommendations..... 121

LIST OF REFERENCES..... 123

# ABSTRACT

A series of numerical simulations using the Penn State University/National Center for Atmospheric Research Mesoscale Model 5 (MM5) Version 2 were conducted to simulate Supertyphoon Herb, a devastating tropical cyclone that made landfall on Taiwan in July of 1996. The interaction of the tropical cyclone (TC) and Taiwan's Central Mountain Range (CMR) is examined through analysis of the vertical motion and potential vorticity (PV) fields as the typhoon approaches the terrain feature. The generation of PV on the lee-side of the CMR is also observed. Comparisons are presented between model output of the TC as it nears Taiwan to a conceptual model; previous research for each of these features is also summarized.

# LIST OF FIGURES


1.1 Topographic map of Taiwan with 200 m contour intervals..... 2

2.1 Best track of Supertyphoon Herb (1996) in 6 hr intervals..... 15

2.2 Translational speed (kt) versus time (DDHH) with distance from landfall (km) in ovals..... 17

2.3 Average minimum central pressure and surface winds at two reporting stations..... 20

2.4 Maximum surface winds and minimum central pressure as a function of time..... 22

3.1 Flow chart of MM5 modeling system..... 32

3.2 Schematic diagram of the vertical layers of the MM5..... 38

4.1 Reproduction of the Liu et al. 1999 schematic radial-height model of the inner core of a mature tropical cyclone..... 40

4.2 Upward (dashed) and downward (solid) motion in an east-west cross section at 0800 UTC, 30 July..... 43

4.3 Best estimate of updraft (solid arrow) and downdraft (dotted arrow) regions relative to the eye at 0800 UTC, 30 July..... 44

4.4 Upward motion (solid) and RH (dashed) in an east-west cross section at 0800 UTC, 30 July..... 47

4.5 Upward (dashed) and downward (solid) motion in a north-south cross section at 0800 UTC, 30 July..... 50

4.6 Horizontal plot of upward motion (solid) in 1.0 m s intervals and wind vectors (60 km spacing) at 3 km at 0800 UTC 30 July..... 52

4.7 Same as in Figure 4.2 but for 0400 UTC 31 July..... 54

4.8 Same as in Figure 4.3 but for 0400 UTC 31 July..... 55

4.9 Same as in Figure 4.4 but for 0400 UTC 31 July..... 57

4.10 Same as in Figure 4.5 but for 0400 UTC 31 July..... 59

4.11 Same as in Figure 4.6 but for 0400 UTC 31 July..... 60

4.12 Same as in Figure 4.2 but for 1000 UTC 31 July..... 63

4.13 Same as in Figure 4.3 but for 1000 UTC 31 July..... 64

4.14 Same as in Figure 4.4 but for 1000 UTC 31 July..... 65

4.15 Same as in Figure 4.5 but for 1000 UTC 31 July..... 68

4.16 Same as in Figure 4.6 but for 1000 UTC 31 July..... 69

5.1 Vertical east-west cross section of positive PV well before landfall, 0800 UTC 30 July 1996..... 71

5.2 Vertical east-west cross section of positive absolute vorticity and potential temperature well before landfall, 0800 UTC 30 July 1996..... 74

5.3 Same as in Figure 5.1 but for 0400 UTC 31 July 1996..... 75

5.4 Vertical east-west cross section of positive absolute vorticity and potential temperature well before landfall, 0800 UTC 30 July 1996..... 77

5.5 Same as in Figure 5.1 but for 1000 UTC 31 July 1996..... 79

5.6 Vertical east-west cross section of positive absolute vorticity and potential temperature over land, 1000 UTC 30 July 1996..... 81

5.7 Horizontal plot of positive PV and wind vectors (60 km spacing) at 1 km well before landfall, 0800 UTC 30 July 1996..... 82

5.8 Horizontal plot of positive PV and wind vectors (60 km spacing) at 3 km well before landfall, 0800 UTC 30 July 1996..... 85

5.9 Same as Figure 5.8 except for 2000 UTC 30 July July 1996..... 87

5.10 Same as Figure 5.7 except for 0400 UTC 31 July July 1996..... 90

5.11 Same as Figure 5.8 except for 0400 UTC 31 July July 1996..... 91

5.12 Same as Figure 5.7 except for 1000 UTC 31 July July 1996..... 93

5.13 Same as Figure 5.8 except for 1000 UTC 31 July July 1996..... 94

5.14 Three PV probe locations..... 96

5.15 North probe at 1 km..... 100

5.16 North probe at 3 km..... 101

5.17 South probe at 1 km..... 102

5.18 South probe at 3 km..... 103

5.19 East probe at 1 km..... 105

5.20 East probe at 3 km..... 106

5.21 Vertical NW-SE cross section of positive absolute vorticity and potential temperature well before landfall, 0800 UTC 30 July 1996..... 108

5.22 Same as Figure 5.21 except for 2200 UTC 30 July 1996..... 110

5.23 Same as Figure 5.21 except for 0000 UTC 31 July 1996..... 111

5.24 Same as Figure 5.21 except for 0200 UTC 31 July 1996..... 112

5.25 Same as Figure 5.21 except for 0400 UTC 31 July 1996..... 113

5.26 Same as Figure 5.21 except for 0600 UTC 31 July 1996..... 114

5.27 Same as Figure 5.21 except for 0800 UTC 31 July 1996..... 115

5.28 Same as Figure 5.21 except for 1000 UTC 31 July 1996..... 116

# CHAPTER 1

# LITERATURE REVIEW AND INTRODUCTION

## 1.1 Introduction

Numerous research projects have dealt with the complex interaction between landfalling tropical cyclones and a significant terrain feature. Only a few such places exist in tropical locations, most of which lack an organized meteorological observing network. Thus, much attention has been paid to furthering meteorological knowledge in this area through numerical simulation. The mesoscale modeling research community has simulated landfalling tropical cyclones on numerous mountainous regions such as Hispañola, the Philippines (Luzon, for example) and Taiwan. The bulk of the research in this area has dealt with Taiwan, due to its large population as well as a mountain range that spans the central portion of the country. The Northwest Pacific is also home to the highest occurrence of tropical cyclones of any other ocean basin in the world. As displayed in Figure 1.1, Taiwan's Central Mountain Range (CMR) is on the same horizontal scale (meso-$\beta$, several hundred kilometers)

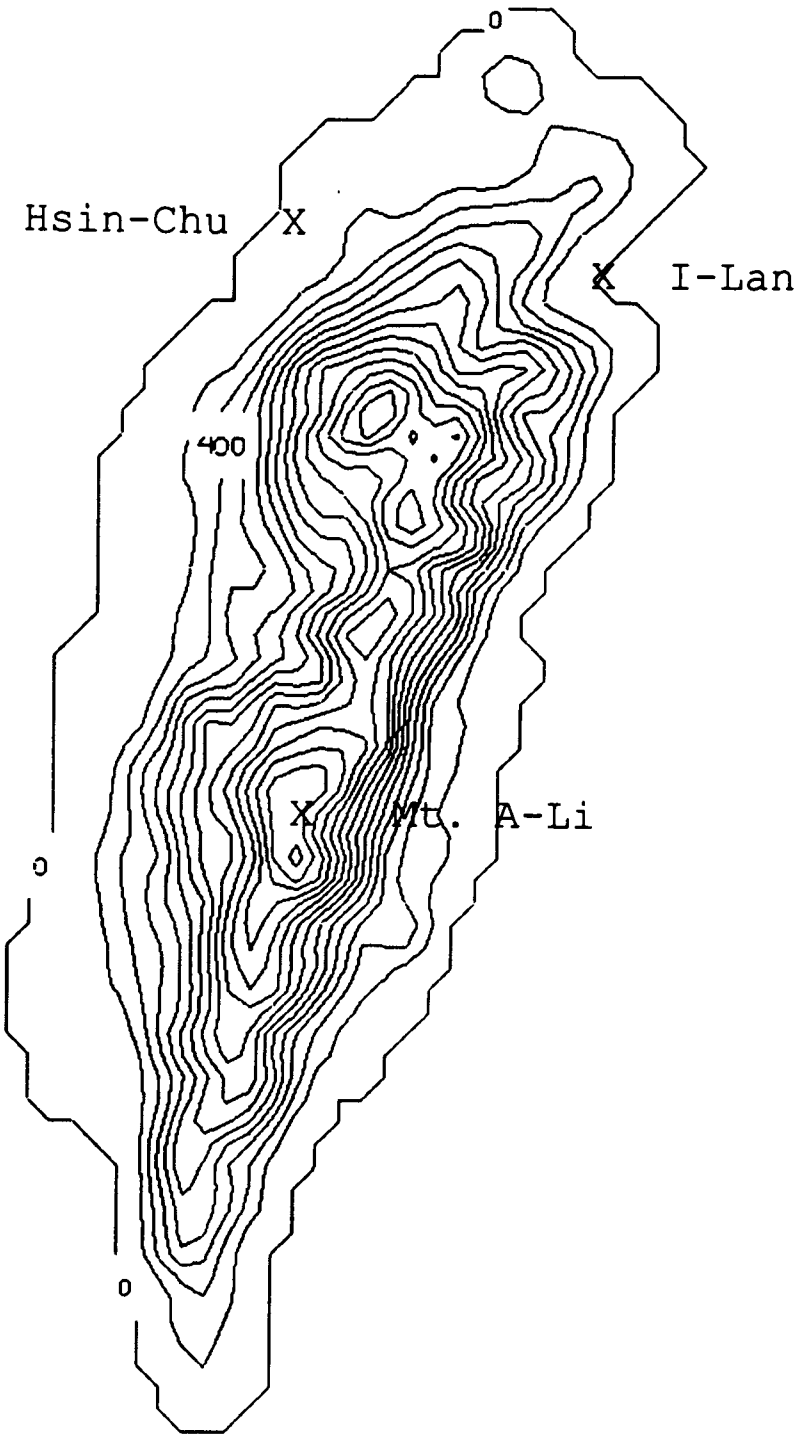


Figure 1.1. Topographic map of Taiwan with 200 m contour intervals.

as that of a tropical cyclone, thus providing unique case study opportunities.

Tropical cyclone track and variations in strength, structure and environment have led to significant forecasting problems for meteorologists attempting to accurately predict landfall in mountainous regions. It was this issue that motivated the numerical weather prediction community to attempt to gain further insight into the intricate interaction between landfalling tropical cyclones and a terrain feature through mesoscale model simulations.

## 1.2 The Early Modeling Years

Early observational and numerical studies conducted in the mid 1970s and early 1980s documented the paths, intensities and life histories of typhoons impacting Taiwan. Brand and Blelloch (1974) published a paper concluding that westward propagating typhoons tended to move cyclonically around the northern end of Taiwan's CMR, and begun to decrease in intensity well before landfall. In 1980, S. T. Wang of National Taiwan University reported on his findings of 53 landfalling typhoons from 1946-1975 that affected Taiwan (Chang, 1982). He resolved that most of the tropical cyclones took a northern track around the

island as shown by Brand and Blelloch. Wang also noted that the weaker typhoons tended to form a secondary low on the lee side of the CMR, resulting in a discontinuous track as it traversed the mountainous island. These two papers were the first to document such occurrences with landfalling tropical cyclones in the Northwest Pacific.

## 1.3 Numerical Simulations of Tropical Cyclones

Chang (1982) used a coarse resolution primitive equation model (60 km horizontal resolution) to simulate a westward propagating tropical cyclone embedded in an easterly flow. An idealized symmetric, oval mountain range resembling Taiwan's CMR with peaks of 2000 m was used in the study. Five experiments were conducted with changes to several parameters such as cumulus heating, suppressed friction and the addition of topography. This modeling study made several important conclusions reinforcing previous work. First, the center of circulation of the tropical cyclone (TC) tended to move cyclonically around the north end of the mountain. Second, the vertical motion fields associated with the circulation were found to be modified orographically by the Taiwan topography. Finally, upward motion regions occurring on the windward slopes of

the terrain were found to exist only in regions of positive potential vorticity.

Bender et al. (1987) used the Geophysical Fluid Dynamics Lab (GFDL) model with an initial easterly basic flow of 5 m $s^{-1}$ and 10 m $s^{-1}$ in two studies to simulate a tropical cyclone impinging on an idealized Taiwan. A simulated mountain range with a height of 2000 m was used. The study made several interesting conclusions. Through sensitivity experiments, it was noted that the basic flow (that not associated with the cyclone itself) was affected by the topography well upstream. As the tropical cyclone traversed the island, its translational speed was shown to increase as it was deflected. The surface pressure was shown to fill significantly as the cyclone made landfall, while the lower and upper level centers of circulation became vertically skewed.

The work of Zehnder (1993) dealt with a large-scale topography interaction with barotropic vortex motion. In this simulation, among other results it was shown that the potential vorticity (PV) gradient pointed perpendicular to lines of constant topographical height except where the terrain was level (i.e., no height change along the surface).

## 1.4 Vertical Velocity Fields

Atmospheric vertical motion, the net upward and downward transport of air through a finite distance, both allows and inhibits convective processes within the TC environment. Numerous studies have investigated the role of vertical motion in various aspects of TCs, from genesis to intensification to storm motion. Specifically, Chang (1982) correlated regions of intense upward motion with positive potential vorticity regions in a numerically simulated TC as it approached an idealized terrain feature.

Molinari and Vollaro (1990) examined averaged vertical motion fields over three time steps in Hurricane Elena (1985). They related maxima within the upward motion fields to changes in the vertical structure and response of the hurricane's vortex through Eliassen's balanced vortex equation. More recently, Liu et al. (1999) devised a conceptual model of the inner-core region of a mature TC, based on an MM5 simulation of Hurricane Andrew (1992). It is presented in Chapter 4 and will be used in this study as a comparative tool for a vertical motion field analysis of an MM5 simulation of Supertyphoon Herb (1996).

For large-scale systems, Holton (1992) defines vertical motion as

$$\frac{Dp}{Dt} = \omega = \frac{\partial p}{\partial t} + \vec{V} \bullet \nabla p + w\left(\frac{\partial p}{\partial z}\right), \qquad 1.1$$

where

$$w = \frac{dZ}{dt}. \qquad 1.2$$

As described in further detail in Chapter 3, MM5 uses a terrain-following (normalized pressure) or σ-coordinate system and thus a transfer of coordinates is needed. In σ-coordinates, the vertical motion (Dudhia et al., 1999) becomes

$$\dot{\sigma} = -\frac{\rho g}{p^*} w - \frac{\sigma}{p^*}\left\{u\frac{\partial p^*}{\partial x} + v\frac{\partial p^*}{\partial y}\right\}, \qquad 1.3$$

where $p^*$ represents p(x,y). Thus, MM5 calculates vertical motion in this fashion, where positive and negative values indicate sinking and rising motion, respectively.

Flow over terrain has also been linked to significant upward motion and precipitation enhancement (Wu et al., 1998) on the windward side of a mountain as well as sinking motion and precipitation minimums on the lee side with a passing TC.

Liu et al. (1999) note that the eyewall of a mature tropical cyclone contains slantwise regions of upward motion with velocities greater than 1.6 m $s^{-1}$. They also note the presence of sinking motion along the inner edge of the eyewall. This air is returned to the marine boundary layer (MBL, $z < 1.5$ km), where it eventually reenters the eyewall region updrafts.

## 1.5 Potential Vorticity Fields

Potential vorticity (PV) concepts have been widely used in tropical NWP to explore the dynamics of a tropical cyclone (TC) as well as its environment. A TC has been described as a "localized positive PV anomaly" (Wu and Wang, 2000, p. 1901), which tends to "follow closely the positive PV tendency associated with the flow field" (Shapiro, 1996, p. 2497). In primitive equation form, Stoelinga (1996) defines Ertel's form of PV as

$$q = \eta \, \rho^{-1} \bullet \nabla\theta \qquad 1.4$$

Here, q is the PV, $\rho$ is density, $\eta$ is the three-dimensional absolute vorticity vector, $\theta$ is the potential temperature, and $\nabla$ represents a three-dimensional gradient operator. In an isentropic coordinate system, PV is conserved and thus is often used in budget calculations to

determine the relative contributions of its various terms. For example, Shapiro and Franklin (1995) note in their findings that the diabatic heating term ($\partial\theta/\partial t$) contributed to relatively low PV anomaly values to the east of a TC. Wu and Kurihara (1996) performed a budget analysis using the GFDL on Hurricane Bob to explore the redistribution of PV due to condensational heating within the vortex of a TC. In this case of Supertyphoon Herb, equation 1.4 is used in the PV analysis to determine how each component contributes to the overall PV anomaly. Future implications in typhoon path may be deduced with from the preliminary findings of this study.

As PV is not a measured quantity, often times a "piecewise inversion" is produced to recover the wind fields at various levels. In one study, Shapiro (1996) deduced separate contributions of individual PV anomalies to the total steering flow. Emanuel and Wu (1995), Shapiro (1996), Molinari and Vollaro (1997), and others have all used the PV piecewise inversion technique extensively to examine TC deep layer mean flows and their relationship to PV anomalies and mean TC motion.

Another, more recently studied aspect of PV analysis in tropical cyclones is the generation of positive PV that

is hypothesized to occur both within the storm environment and as a result of its associated flow over a terrain feature. May and Holland (1999) evaluated positive PV generation within convective rainband regions of a TC and Lin et al. (1999) documented positive PV changes that occurred on the mountain lee side (western side of the terrain feature in an easterly flow) with the landfall of a TC.

Until the beginning of the last decade, relatively little modeling research presented in the literature deals with the PV point of view on the interaction of a TC with a significant terrain feature. More specifically, little or no documentation of the symmetric positive PV structure or PV tendency fields associated with a landfalling TC in a mountainous region has been examined. The subsequent lee side PV generation that is hypothesized to occur with the approach and passing of a TC has been unexplored as well. This study examines the terrain interaction of a mature tropical cyclone and the subsequent environmental changes that occur in the process.

In this study, an MM5 simulation of Supertyphoon Herb is examined from both a vertical motion and potential vorticity perspective and compared to the conceptual model

proposed by Liu as it encounters a terrain feature. A "zone of transition" is found to have occurred four to six hours prior to landfall as Herb began to lose characteristics exemplified by the conceptual model. Other comparisons to the conceptual model are made in moisture fields as the TC approaches the CMR.

Two "PV ways of thinking" are investigated as well. First, the structure of the TC in terms of a positive PV anomaly will be examined as it encounters Taiwan's CMR. East-west cross sections through the center of the typhoon will be presented as changes occur upon landfall. These changes are then compared and contrasted with that of the vertical motion fields for the same time period. Second, as the TC reaches the CMR, an increase in positive PV is found to "generate" on the lee side of the mountain. Newly formed "bulls eyes," or mesoscale areas of positive PV are then advected into the TC as it approaches the CMR. When the typhoon is over the mountain, these regions of positive PV are shown to decrease both in number and magnitude. Based on equation 1.4, it is then hypothesized that this generation is mainly due to an increase in the vertical potential temperature change ($\partial\theta/\partial z$). As in the vertical velocity analysis, a "zone of transition" is found to occur

within the 0400-0600 UTC window 31 July, when the TC is approximately 200-300 km prior to landfall. It remains unclear, however, the extent the effect of this new PV has on the TC and its environment.

# CHAPTER 2

# SYNOPTIC OVERVIEW OF SUPERTYPHOON HERB (1996)

## 2.1 Overview

The island of Taiwan is located in the North Pacific and contains a significant mountain range (average elevation 3000 m), appropriately labeled the Central Mountain Range (CMR) as it spans the center of the country oriented north to south. The length and width of the most significant terrain making up the CMR is approximately 300 km by 100 km, respectively. As this scale is on the same order of magnitude as that of a tropical cyclone, it provides an interesting opportunity to perform analysis of the interaction of two "mesoscale" features.

Taiwan is affected annually by an average of four typhoons, based on data collected over a 20-year period (Wu and Kuo, 1999). The 1996 typhoon season was no exception. Supertyphoon Herb was the eighth tropical cyclone to attain "typhoon" status that year and the third storm on which Taiwan's Central Weather Bureau (CWB) had issued a "warning" (Wu and Kuo, 1999). Herb made landfall on Taiwan as a Saffir-Simpson Scale category five storm. In a period of just over seven hours, Typhoon Herb wreaked havoc on the island, causing numerous landslides, debris flows and

significant flooding (Wu et al., 1998). In the end, over $5 billion (U.S.) in property and agriculture damage was recorded, as well as 51 deaths and 22 missing persons. This extreme event became the most destructive single meteorological event to impact the island to that date (Wu and Kuo, 1999). This chapter will attempt to lay the meteorological groundwork surrounding this tropical event on which the numerical study is based.

## 2.2 Track Analysis

Figure 2.1 displays Typhoon Herb's best track as identified by the CWB based on minimum central pressure estimates and surface wind fields. Herb began as tropical wave composed of a cluster of thunderstorms and became more organized, developing into a tropical depression located at 16°N 153°E on 23 July 1996 (Fung, 1997). A Pacific anticyclone was located to the north of the tropical cyclone (Wu and Kuo, 1999) and kept it moving steadily west. While riding the Pacific High's southern edge, Herb strengthened to a tropical storm on 0600 UTC 24 July. As the tropical cyclone continued on a west-southwest course it continued to deepen, reaching typhoon status on 26 July with maximum sustained winds of 65 kt, as shown in Figure

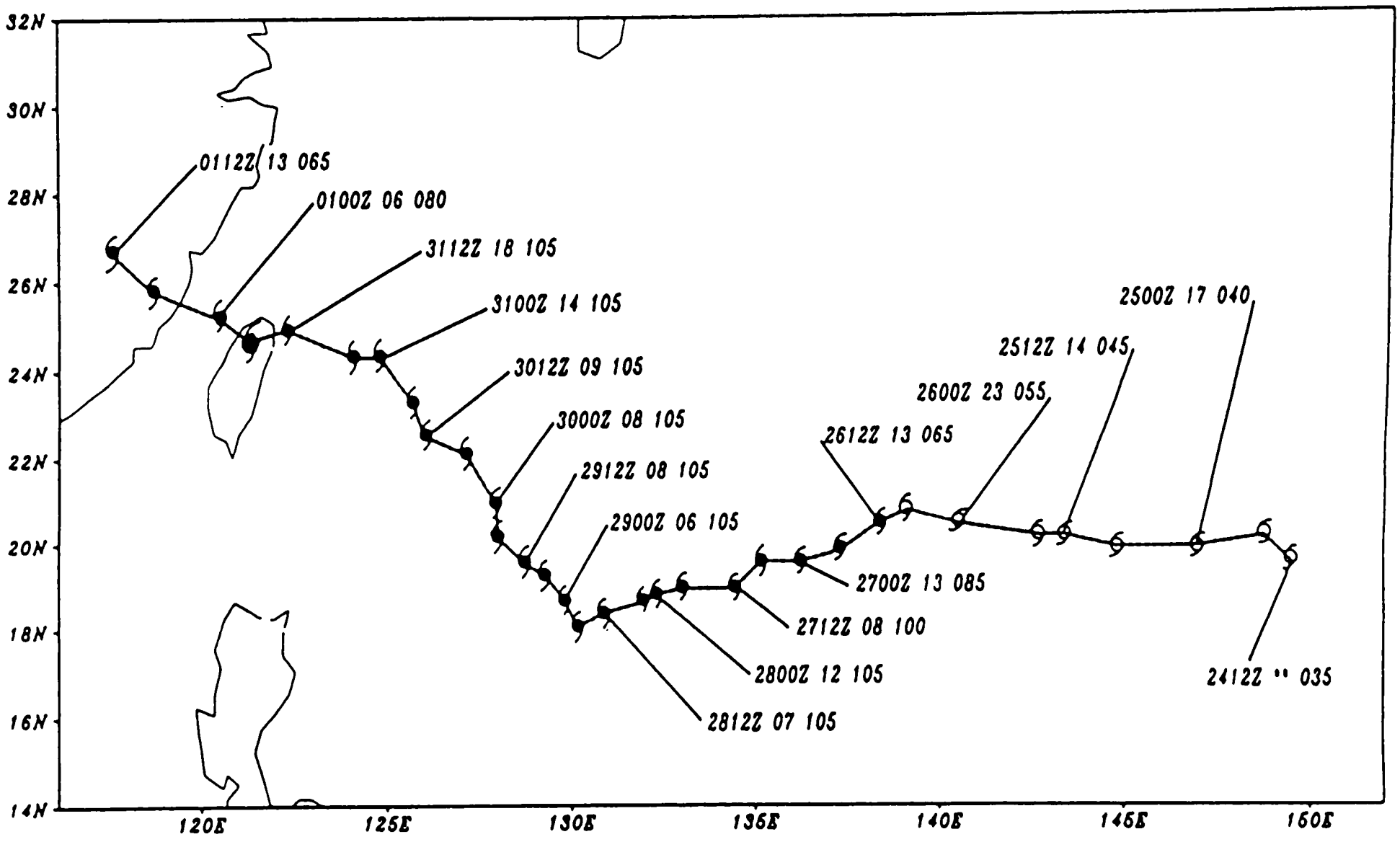


Figure 2.1 Best track of Supertyphoon Herb (1996) in 6 hr intervals. Solid (open) symbol indicates typhoon (tropical storm) with translation speed (kt) and intensity (kt) at each time (from Wu et al., 1999).

2.1. Herb's translational speed remained constant during this stage, averaging approximately 12 kt.

By 0600 UTC on 27 July, Taiwan's CWB estimated a 300 km radius of gale force winds of about 100 kts (Wu and Kuo, 1999). Twelve hours later, the CWB again estimated a maximum surface wind of 100 kt along with a minimum central pressure of 925 hPa (Wu and Kuo, 1999). On 29 July, the Pacific high moved on to the east (Wu and Kuo, 1999) allowing Typhoon Herb to shift on a more north-northwesterly track. Herb continued along this north-northwest path for approximately the next three days, while continuing to gain intensity.

## 2.3 Typhoon Translational Speed

Figure 2.2 displays Herb's translational speed (in kt) plotted against time from 0000 UTC 29 July to 1200 UTC 1 August. The approximate distance from the eye of the typhoon to the CMR is shown for each point in kilometers (km). The approximate distance to the CMR was then calculated from Figure 2.1 by an estimated latitude and longitude position of the typhoon's eye every 12 hours through the period. A point in the middle of the CMR at 25°N 121°E was chosen as an endpoint for the distance

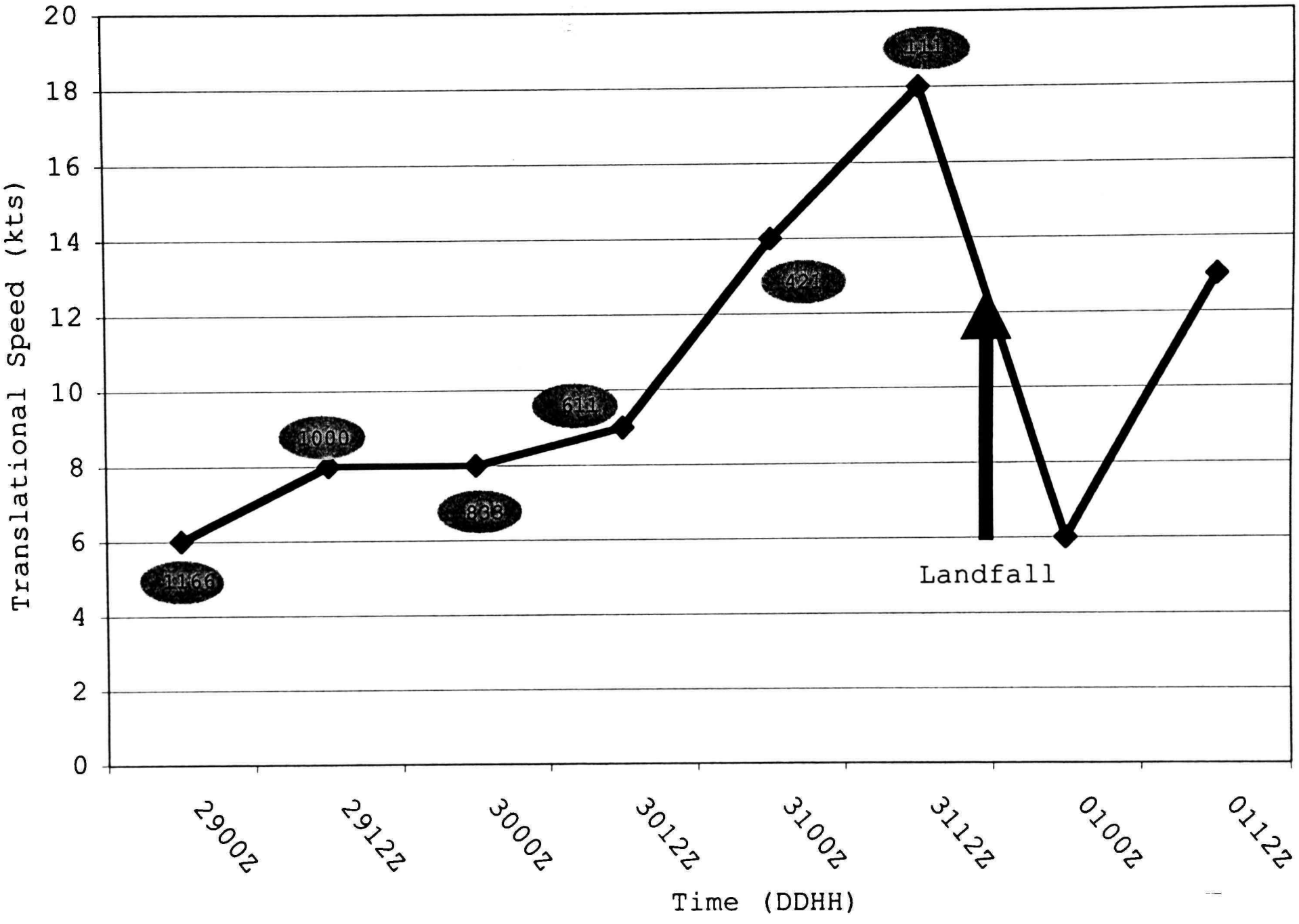


Figure 2.2 Translational speed (kt) versus time (DDHH) with distance from landfall (km) in ovals. Landfall is marked with a heavy arrow.

calculation due to its position in northern Taiwan directly in the path of the impending typhoon. The Pythagorean theorem, given as

$$C^2 = \sqrt{(A^2+B^2)} \qquad 2.1$$

was then used to calculate Herb's distance from the CMR. A and B represent an estimated X and Y distance from the CMR (25°N 121°E), and C is the resulting cyclone distance. The estimated position for the landfall of the storm is shown on Figure 2.1, just after 1200 UTC. This time period covers the typhoon's approach toward as well as landfall onto the island.

Herb's landfall on Taiwan is marked on Figure 2.2 with a dark arrow just after 1200 UTC 31 July, south of Taipei (pop. ~2,000,000), the nation's capital. This graphic clearly shows that the tropical cyclone steadily increased in forward motion on approach to the island with an average speed of about 11 kt. A maximum translational speed of 18 kt is estimated when the tropical cyclone eye is a mere 111 km from the island.

By landfall, Herb's forward speed began to decrease rapidly, by about one-third in just under 12 hours. This is consistent with the work of other numerical and observational experiments (Chang, 1982; Yeh, 1993). All

are in agreement that the translational speed of a typhoon incident on Taiwan will increase until just prior to landfall, when a significant decrease in speed and intensity is observed. Generally, it is hypothesized that the mountain range acts as a physical barrier to the lower and mid-level steering flow, causing the typhoon to deflect to the north portion of the island while retarding its forward motion (Chang, 1982; Bender et al., 1985).

## 2.4 Surface Pressure and Wind Analysis

Typhoon Herb continued to weaken to a category 1 storm until re-emerging on the west side of the island into the Taiwan Strait. The observed decrease in translational speed is accompanied by an overall weakening in the storm's intensity, as shown in Figures 2.3 and 2.4. Figure 2.3 displays two reporting stations on Taiwan with pressure (hPa) and average surface wind speed (m $s^{-1}$) and direction plotted versus time every hour for 28 hours. Station Hsin-Chu is located on the northwestern side of the island while station I-Lan is located in northeastern Taiwan as displayed by Figure 1.1. Herb passed directly over Hsin-Chu upon landfall. As shown in Figure 2.3, both reporting stations exhibit a similar profile. The pressure at each

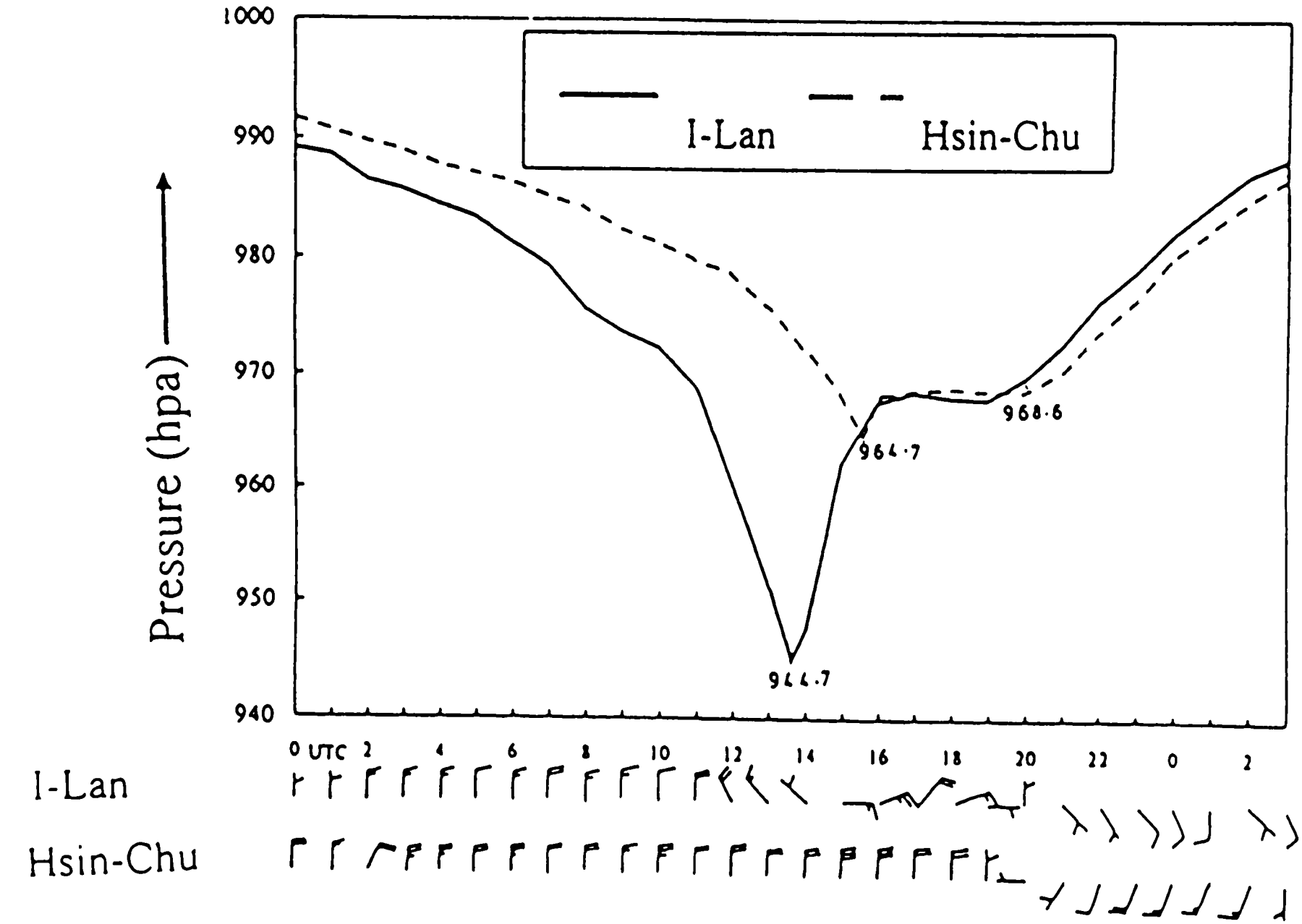


Figure 2.3 Average minimum central pressure and surface winds at two reporting stations. Pressure in units of hPa and winds in m $s^{-1}$ (from Wu et al., 1999).

station continued to rapidly decrease with the approaching typhoon, at an average of 3.5 hPa per hour for the first 14 hours. Just after initial landfall at about 1300 UTC on July 31, both reporting stations measured a rapidly increasing central pressure, indicative of the storm's weakening intensity.

Also of interest is the wind shift that occurred with the cyclone's passage. At I-Lan, the first of the two stations to be affected by the typhoon, a somewhat gradual backing (over 10 hours, 1200 UTC to 2200 UTC 31 July) of the surface winds from north-northwest to a south-southeast is observed. A minimum pressure of 944.7 hPa, as displayed on Figure 2.3, is observed at 1300 UTC just after landfall.

Further to the west at Hsin Chu, a more rapid backing of the winds is observed. A sharp transition from north to southwest occurs in just over 3 hours (1900 UTC to 2200 UTC 31 July). One would expect this more rapidly defined wind shift as the eye of Herb passed directly over the reporting station.

Figure 2.4 is adapted from Wu and Kuo (1999) as well. A vertical profile of the terrain of Taiwan with two curves indicating measured minimum central pressure (dashed) and maximum surface winds (solid) are also shown both before

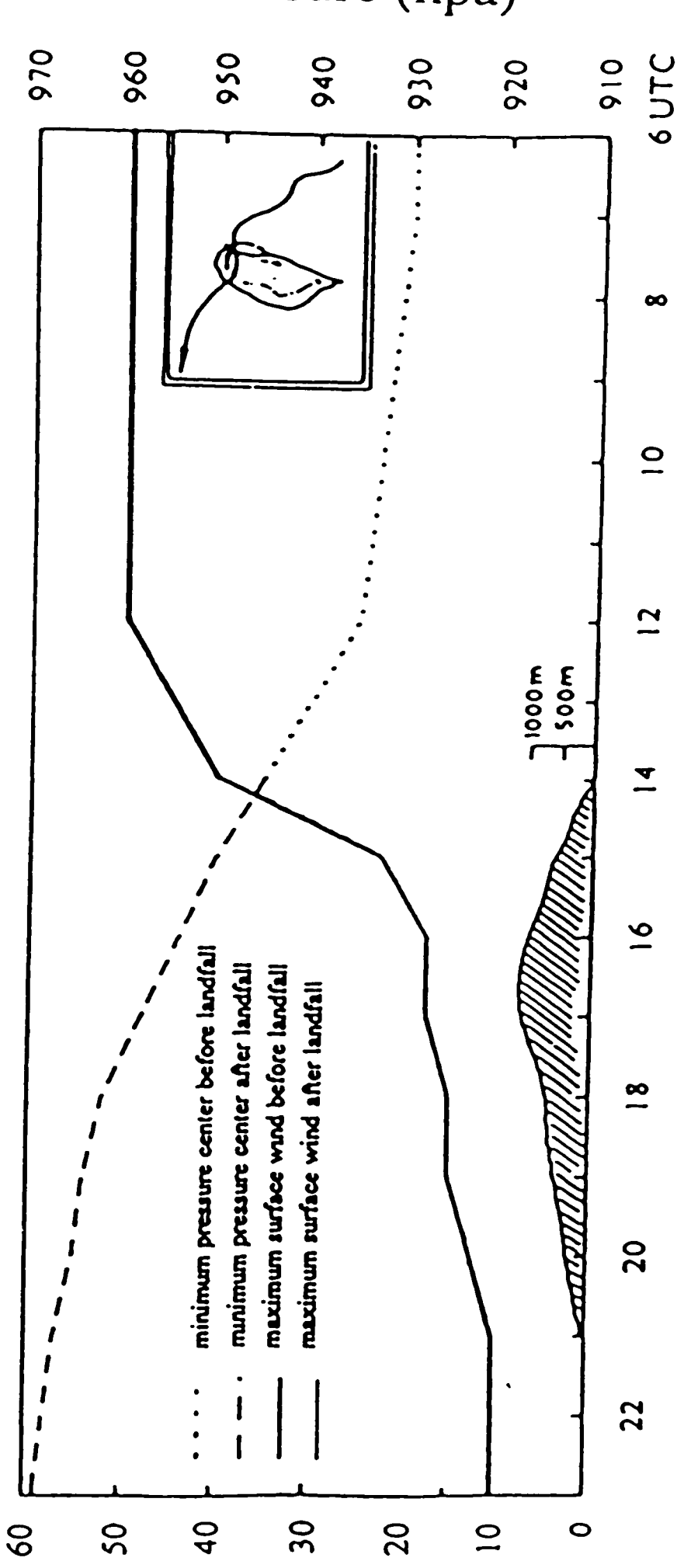


Figure 2.4 Maximum surface winds and minimum central pressure as a function of time. Pressure is in units of hPa and winds in m $s^{-1}$ (from Wu et al., 1999).

and after the typhoon landfall. A caveat exists for this figure. Time is increasing to the left on the abscissa from 0600 UTC 31 July to 0000 UTC 1 August, contrary to conventional methodology. Herb's eye makes landfall where the two curves intersect, just before 1400 UTC. This graphic reinforces the previous notion that the overall intensity of Typhoon Herb lessened just before and more significantly over the steep terrain of the CMR.

As early as two hours prior to landfall, both the maximum winds and minimum central pressure associated with the tropical cyclone began to decrease and increase, respectively. In those two hours (from 1200 to 1400 UTC), the pressure increased about 15 hPa (an average rate of 7.5 hPa $hr^{-1}$) while the maximum wind decreased about 12 m $s^{-1}$ (an average of 6 m $s^{-1}$ per hour) over the same time period. Comparatively, for the next seven hours over Taiwan, Herb's maximum wind speed and minimum pressure trends continued. Wind speeds fell another 30 m $s^{-1}$ (or at a rate of 4.3 m $s^{-1}$ per hour) while pressure increased an additional 20 hPa (at a rate of 2.9 hPa per hour). This strengthens the argument of the overall rapid weakening of the typhoon just before landfall.

In evaluating the rates of change of each parameter, both before and during landfall, an interesting result surfaces. The rate at which the minimum central pressure increased was more than twice for the two hours just prior to landfall than that for the seven hours the typhoon spent over land. The same result held true for the maximum winds. In the two hours before Herb made landfall, the rate at which the maximum winds decreased was 1.5 times greater when compared with the seven-hour rate of decrease over land. These results indicate that the advection of dry, stable air originating over the CMR into the typhoon environment played a significant role in its overall weakening. As the tropical cyclone continued to traverse the island, dry air was still advected into the storm, providing further weakening, albeit at a slower rate.

By 0600 UTC on 1 August, Typhoon Herb had completely traversed Taiwan and began to slowly intensify to a category 2 storm as it traveled over the Taiwan Strait. After reaching mainland China at 1000 UTC on 1 August, Herb became extratropical and continued on a west-northwestern path (Fung, 1997).

## 2.5 Precipitation Distribution

As with most tropical systems enriched with large quantities of moisture, Herb produced a significant amount of precipitation in a relatively short period of time. According to Wu et al. (1998), the Central Mountain Range enhanced the total rainfall amount, particularly in the southcentral areas of the island. As Herb traveled over the northern part of the island (refer to Figure 2.4 insert), a northwestern flow associated with the typhoon environment converged with a more westerly flow over the central area of the island. This convergence combined with significant orographic lifting over the central and western slopes of the CMR resulted in precipitation enhancement along the central and western portions of Taiwan.

Record rainfall totals (Wu et al., 1998) were measured in two 24-hour periods beginning on 31 July. An observing station on A-Li mountain, located in central Taiwan, reported 1094.5 mm (approximately 43 in) of precipitation on 31 July and an additional 892 mm (35 in) on 1 August (Wu et al., 1998). Maximum rainfall amounts were recorded to the immediate west of the highest peaks of the CMR (Wu et al., 1998). In fact, the northern Taiwan station of Nio-

Drag recorded an astounding 1044 mm (41 in) of precipitation over the same 24-hour time period. In examining the rainfall distribution, the eastern side of the CMR remained relatively dry due to a persistent downsloping wind component as the typhoon traversed the island. This will be examined further in later chapters.

Three factors led to the significant amount of precipitation received in the north and central mountain regions of Taiwan from Herb (Wu and Kuo, 1998). These are:

1. The large amount of water vapor associated with the tropical cyclone, feeding convective systems within the typhoon environment,

2. The typhoon's rather slow (> 7 hours) movement across the island, allowing a longer duration of precipitation,

3. The landfall on the northern side of the island, preventing any significant airflow blocking, thus not destroying the typhoon completely.

Finally, this tropical event is of significant interest to the discipline of tropical mesoscale meteorology. With the lack of observations in the tropical Pacific Ocean and previous model simulations (Chang, 1982, for example) containing coarse horizontal resolution (Wu

and Kuo, 1999) detailed descriptions of mesoscale processes are not easily obtained. Further, the interaction of the typhoon with Taiwan's CMR is quite complicated, and a numerical study with a fine horizontal mesh is of significant value to gain further insight into the physical processes and structure. The remainder of this project will focus on an analysis of the model simulation of Typhoon Herb, with special attention paid to the vertical motion and potential vorticity fields as it approaches the CMR.

# CHAPTER 3

# THE MESOSCALE MODEL DESIGN AND DESCRIPTION

## 3.1 Background

This project employs version 2 of the fifth-generation National Center for Atmospheric Research (NCAR)/Penn State University (PSU) Mesoscale Model (MM5). The MM5 is a three-dimensional, non-hydrostatic model suite. It is used operationally in real-time as well as in a variety of synoptic and mesoscale theoretical studies (Dudhia et al., 1999). The model includes some 50,000 lines of Fortran and C code and contains over 200 subroutines. It also involves the use of several preprocessing programs to be described later.

MM5's usefulness stems from its ability to simulate a wide variety of meteorological phenomena over various horizontal scales. Horizontal domains ranging from the synoptic (1000's of kilometers) to the mesoscale (10's to 100's of kilometers) are routinely used in forecast simulations. In particular, MM5's ability to reproduce meso-$\beta$ and meso-$\gamma$ features (scales from approximately 2-200 kilometers) make it an extremely useful tool for gaining deeper insight into such meteorological features as frontal zones, mesoscale convective systems, or land-sea breeze

circulations. In this study, a tropical cyclone (scale of 500 to 1000 kilometer radius on average) traversing the island of Taiwan in the Pacific Ocean is simulated. The actual MM5 simulation was run on a DEC ALPHA workstation by Professor C.-C. Wu at National Taiwan University. The model simulation was originally run to examine the detailed precipitation distribution over Taiwan as a result of Typhoon Herb (Wu and Kuo, 1999). The subsequent output was then shared with Texas Tech University. In the following sections, the specific model design is outlined to provide insight into its operation as well as the current study to be examined.

## 3.2 Physics Options for the Simulation

MM5 contains numerous physics options for heating, ice physics, planetary boundary (PBL) characteristics and cumulus parameterization. There are also a plethora of options to assimilate surface and/or upper-air observations into the initialization process for a more realistic forecast simulation. In this tropical cyclone forecast study, certain options were chosen over others based on the meteorological features to be analyzed.

### 3.2.1 Cumulus Parameterization

The Betts-Miller cumulus was chosen as a cumulus parameterization. It is based on a relaxation adjustment to a referenced post-convective thermodynamic vertical profile (Dudhia et al., 1999). This option is a good approximation for horizontal scales greater than 30 km and does not contain an explicit downdraft in its features (Dudhia et al., 1999). While this scheme would not be the best choice for an intensely convective feature such as a supercell thunderstorm or MCS, it is often used in tropical simulations.

### 3.2.2 Planetary Boundary Layer (PBL) Scheme

The Blackadar PBL was used in this study. It produces a high resolution layer containing 5 vertical levels in the lowest 1 km for the run. The surface layer is less than 100 m deep. A free-convective mixed layer also exists.

### 3.2.3 Explicit Moisture Scheme

The simple ice scheme of Dudhia et al. (1999) is used. In this option, ice does not exist above the freezing level and instantly freezes below. Thus, supercooled water droplets do not form in the model atmosphere.

### 3.2.4 Radiation Scheme

The cloud-radiation scheme of Dudhia is used. This option accounts for both shortwave and longwave radiation as well as any interaction with clouds or clear-air. Surface radiation fluxes and atmospheric temperature tendencies are both accounted for in this option.

## 3.3 Preprocessing Programs

A schematic diagram (Figure 3.1) displays the various preprocessing programs involved in the model suite. These programs that users to take virtually any set of observational or pre-simulated data and incorporate it into a new forecast simulation. All six programs are used in a specific order, depending on the input data and desired result. Each individual program separately performs a certain function to run the MM5 from initialization until the final output product is available visually.

A complete MM5 simulation begins with the TERRAIN program, which is chiefly responsible for creating output files of land-use categories as well as identifying the topography of the area of interest. Numerous topographic input files are available from such organizations as the United States Geological Survey (USGS) and are given in

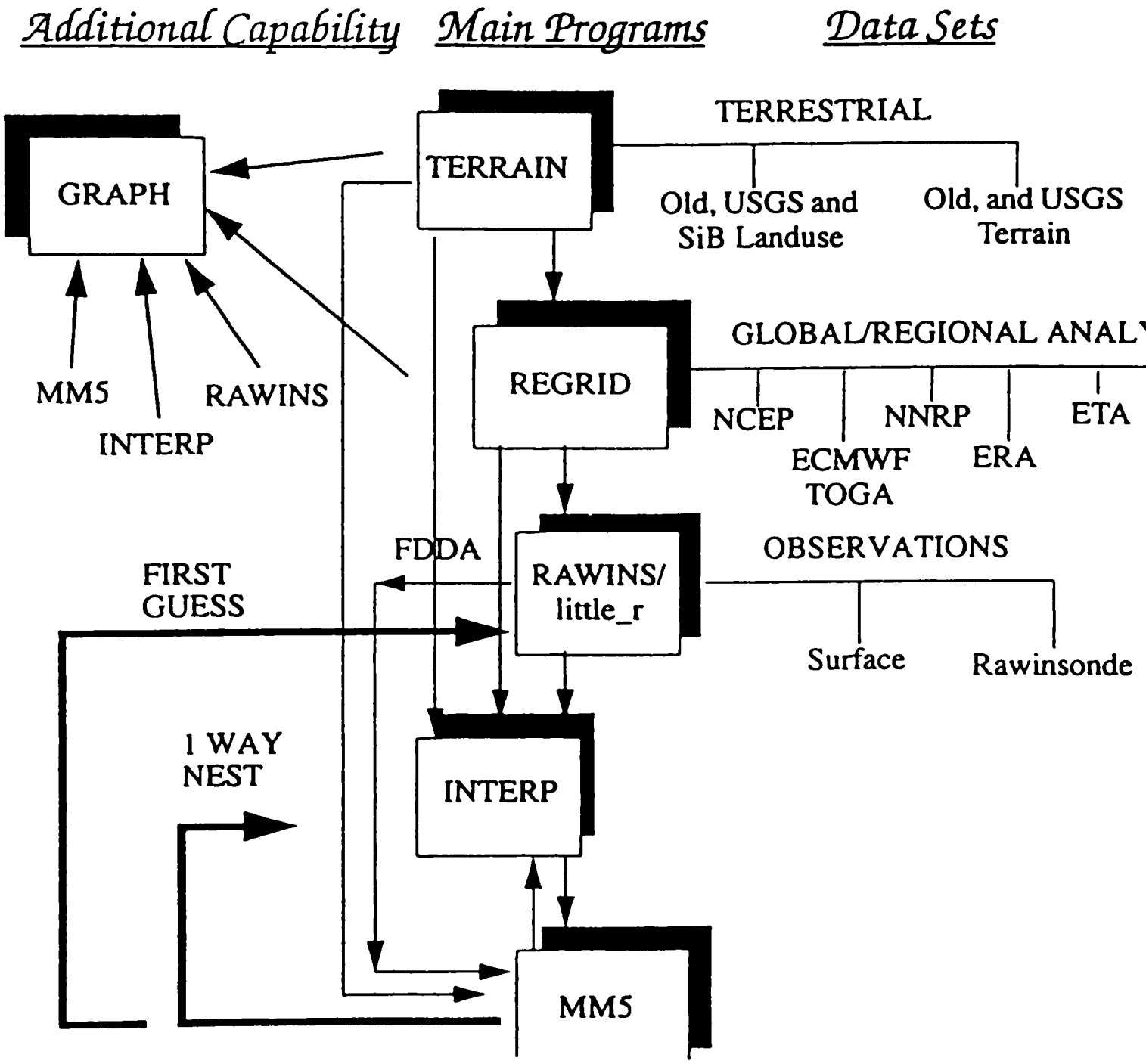


Figure 3.1. Flow chart of MM5 modeling system (from Dudhia et al., 1999).

several resolutions. In this study, a 30-second resolution is chosen, giving very detailed elevation information of Taiwan's CMR.

In this step, the user also chooses both the horizontal and vertical model domain boundaries. A triple-nested horizontal domain is used in this study, with resolutions of 60 km, 20 km, and 6.7 km, respectively. The analysis conducted in this project focuses only on the finest horizontal resolution of 6.7 km (total number of horizontal data points is approximately 24,000 on any given vertical surface). In the vertical, 23 levels are simulated, extending upward to approximately 19 km in the atmosphere. To give a detailed picture of the PBL, 5 of the 23 total vertical surfaces exist from the surface to 1 km.

The REGRID program uses both the output from TERRAIN and the initial meteorological data as its input. All of the data is then read in and written to an "MM5-friendly" grid. For each specified time period, all data provided is written to a horizontal slab of the atmosphere for a given pressure surface. No analysis has yet been completed, but all data is placed in a format usable by either the next preprocessing program or the MM5 program. In the this

simulation, the European Centre for Medium Range Weather Forecasting (ECMWF) global analysis beginning 1200 UTC on 29 July 1996 was employed. Some 12 hours later (0000 UTC 30 July 1996), a fully developed vortex with a radius of 760 km had developed (Wu and Kuo, 1999).

Program RAWINS performs the initial meteorological analysis on the input data and produces the first-guess field (Dudhia et al., 1999). An objective analysis of the surface and upper-air data is performed and the resulting output is later used as the initial and boundary conditions. It is at this point that any "bogus" data may be incorporated to help the model "spin up" and perform a simulation closer to that which is observed. For the Typhoon Herb simulation, the fully developed vortex produced from the RAWINS program was lifted and merged with ECMWF analysis at 0000 UTC 30 July 1996. The "best track" analysis (Figure 2.1) was used to place the actual starting position of the inserted vortex. By inspection, it appears that the center of Typhoon Herb at this time is located at approximately 21°N, 127.4°E, or about 1000 km to the southeast of Taiwan. The surface and 3-dimensional output fields produced in this step are then used in later programs.

The INTERP program is the last preprocessing program before data is submitted into the actual MM5 program. It is responsible for transforming the data from the previous analysis programs to one usable by the MM5. This process is achieved through vertical and horizontal interpolation, data reformatting, etc. (Dudhia et al., 1999). The integrated mean divergence is removed as well during this stage, resulting in less initial condition "noise." It is this process that also transforms coordinate systems from the defaulted constant pressure surfaces. In this experiment, as the CMR is a vital part of the simulation, the pressure coordinates are transformed to "terrain-following," or the $\sigma$-coordinate system. This coordinate change will be discussed in greater detail in the following section.

The MM5 program is the actual numerical weather prediction segment of the package. Once the boundary and initial conditions are finalized, a forward progression of time integration takes place. This is the "prediction" or "forecast" that the model performs. In the Herb simulation, MM5 began its forecast simulation at 0000 UTC 30 July 1996 and marched forward in two hour increments terminating at 0000 UTC 1 August 1996. The entire model

simulation covered 48 hours. A series of MM5 experiments were conducted at National Taiwan University, making use of the same physics options for each run. The 60 km and 20 km horizontal resolution experiments were first conducted as "control" experiments, followed by a finer mesh 6.7 km run. Again, in this study, only the finest 6.7 km horizontal resolution output is analyzed.

## 3.4 Vertical Coordinate System

MM5 initially analyzes input data on constant vertical pressure surfaces (the 500 hPa surface, for instance) but interpolates all data to the so-called $\sigma$ or terrain-following coordinate system where:

$$\sigma = \frac{(p - p_{top})}{(p_{sfc} - p_{top})} \qquad 3.1$$

In equation 3.1, p is the given pressure, $p_{top}$ is the pressure of the top boundary and $p_{sfc}$ is the lower boundary pressure (Dudhia et al., 1999). Thus, by defining this new, non-dimensional coordinate system as proportional to the pressure normalized by the surface pressure, $\sigma$ decreases with height and has values of $\sigma$=1 at the surface (regardless of the terrain height) and $\sigma$=0 at the upper limit. The advantage of such a coordinate system in a

model containing significant geographical features is that surface pressure is not a function of horizontal variables and vertical velocity, w, is always zero at the ground regardless of terrain height (Holton, 1992). Figure 3.2 displays the breakdown of vertical levels and half-levels on which data is displayed. This study contains 23 levels in the vertical, with 5 in the lowest 1 km for a high resolution PBL of the simulated atmosphere. This design is particularly useful in analyzing model PBL fields, which generally lie below the 1 km level.

## 3.5 Viewing the Output

The final part of any complete model package is a program to allow the user to view the output. In this study, VIS 5-D version 5.2 is used. The program, a product of The University of Wisconsin-Madison, has many practical meteorological and non-meteorological applications. The software allows the user to view both gridded and irregularly spaced data with a graphical interface relatively easily.

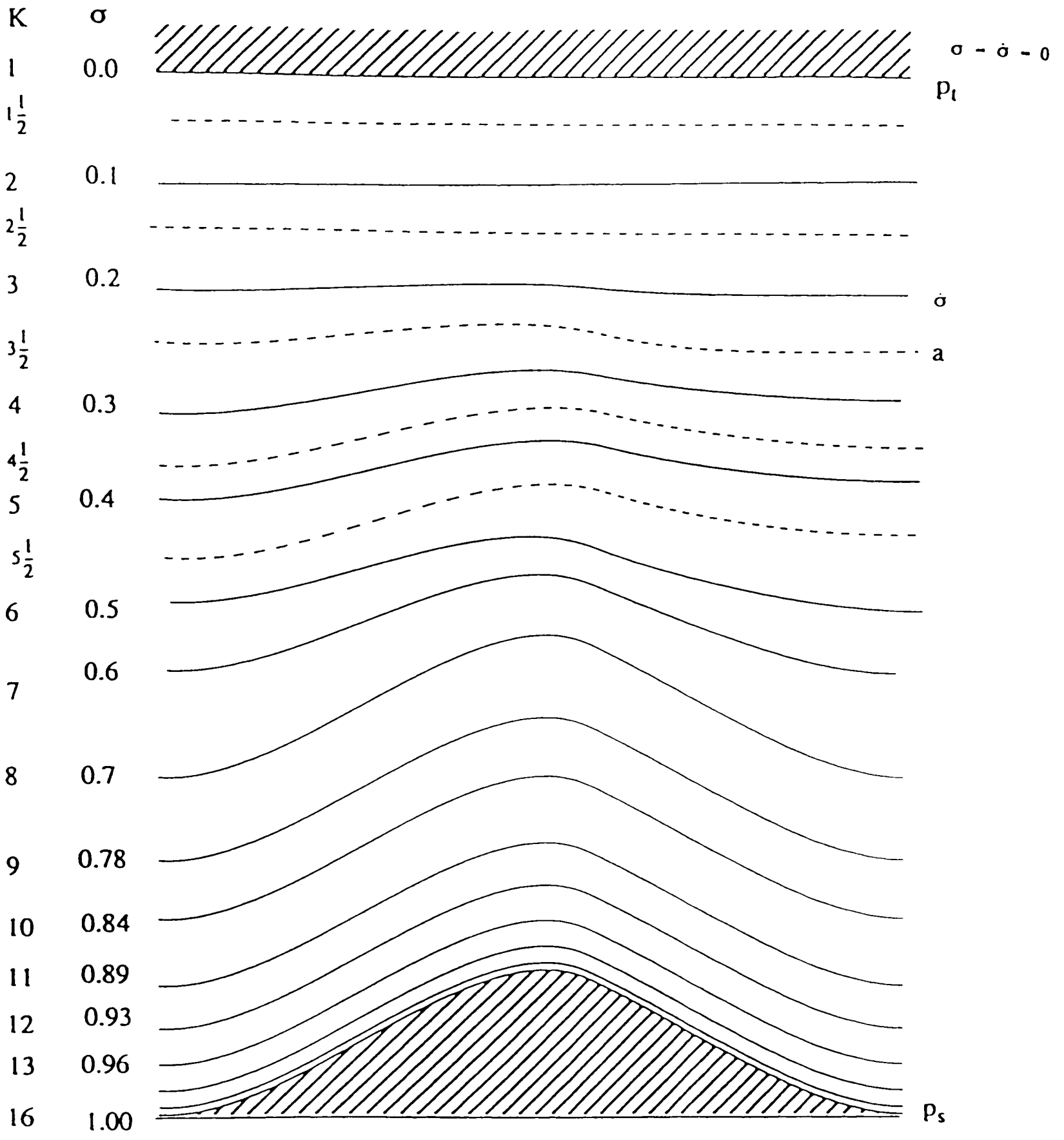


Figure 3.2. Schematic diagram of the vertical layers of the MM5. Dashed lines represent half-sigma levels, solid lines denote full-sigma levels (from Dudhia et al. 1999).

# CHAPTER 4

# VERTICAL MOTION ANALYSIS

## 4.1 The Conceptual Model

The conceptual model of Liu et al. (1999) as mentioned earlier will be used as a comparison tool in this section. Figure 4.1 displays a schematic radial-height model of a mature TC as presented in Liu et al. While no specific values are presented in the text, it is assumed that a horizontal diameter of approximately 200 km and height of 15 km (as expected in an actual TC) are used in the conceptual model. The model is designed to describe the axisymmetric structures identified in the inner core region of an MM5 simulation of 1992's Hurricane Andrew. This conceptual model is chosen due to its similarities in strength, translational speed and northwest track to that of Herb. The model simulations for each are also close in horizontal resolution and physics options. The conceptual model is quite detailed, particularly within the eye and eyewall region. It is well beyond the scope of this project to present each minute detail, and thus features relevant only to this analysis will be discussed. Readers are encouraged to consult the original publication for a complete treatment of the conceptual model.

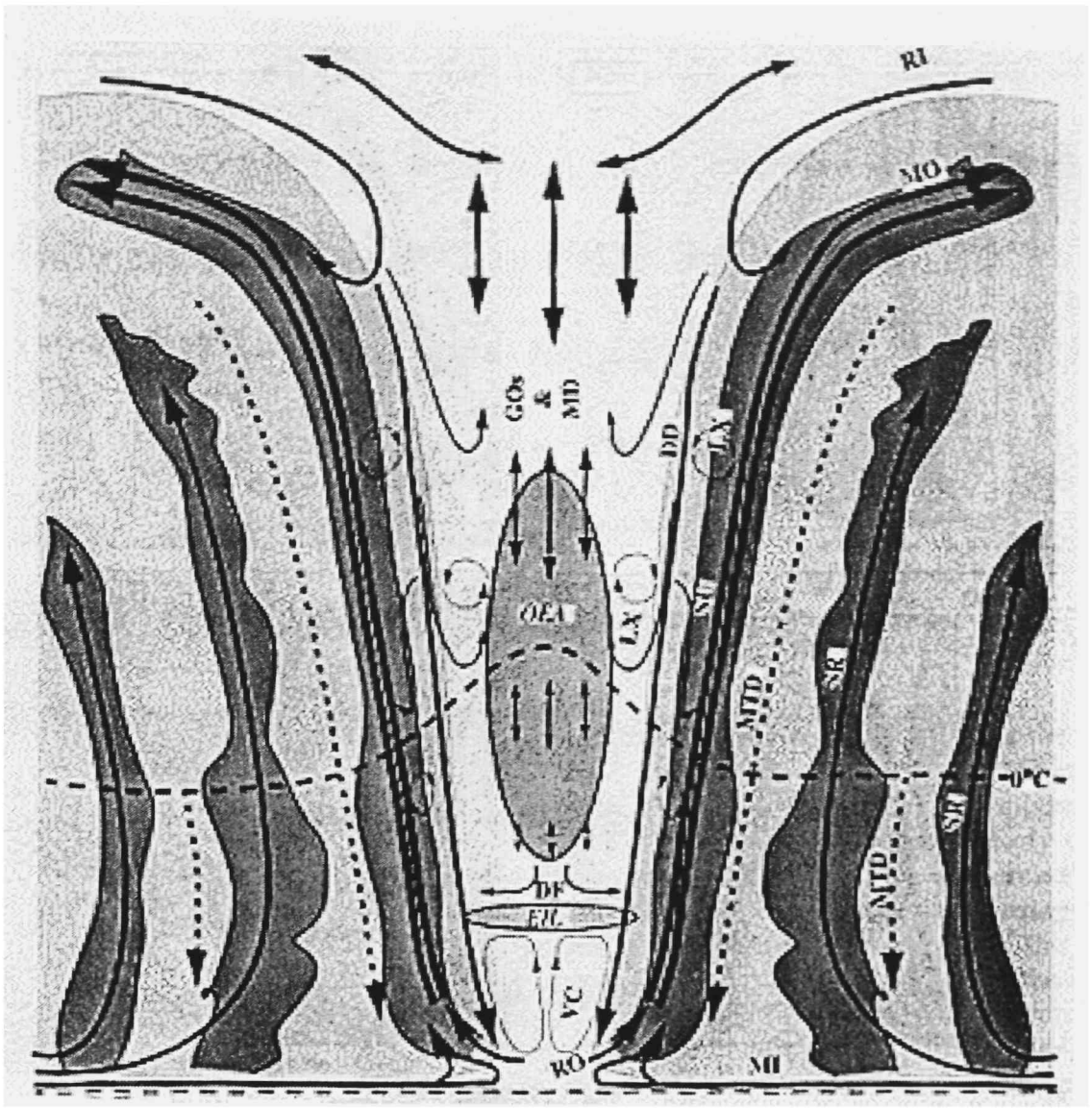


Figure 4.1. Reproduction of the Liu et al. 1999 schematic radial-height model of the inner core region of a mature tropical cyclone. The shaded regions represent the convective eyewall and spiral rainbands. The main outflow (MO), spiral updrafts (SU), main inflow (MI), spiral rainbands (SR), dry downdraft (DD), and moist downdrafts (MTD) are labeled in the figure. Other abbreviations are given in the original source.

The most pronounced air streams are shown in Figure 4.1 with heavy arrows, while the light and dark shaded regions represent the convective eyewall and spiral rainbands, respectively. The main inflow (MI) is rooted in the marine boundary layer (MBL), defined as less than 1.5 km above the surface, and is responsible for feeding the convective eyewall region with high $\theta_e$ air. The main outflow (MO) regions extend from the MBL radially outward, tilting away from the eye with height. Spiral rainbands (SR) and spiral updrafts (SU) with imbedded regions of rising motion (as displayed by the heavy arrows) exist radially outward throughout the eyewall. These areas become less intense away from the eye, and continue to tilt outward with height through the eyewall region of the TC.

A relatively weak region of sinking dry air (identified as 'DD' for dry downdraft) is observed immediately to the inside of each main outflow region penetrating slantwise inward toward the eye. This DD region is believed to be the result of the sublimation/ evaporation cooling process that occurs as the air penetrates downward toward the MBL. Liu et al. note that the term "dry downdraft" refers to relative humidity (RH) differences between 50% and 90% that exist in the region

where the most pronounced sublimation/evaporation processes occur. Moist downdraft (MTD) regions also occur between the spiral rainband/updraft regions, in an alternating pattern. These regions are believed to act as an additional source to the MI, feeding in unstable, high $\theta_e$ air into the updrafts.

In the next few sections, this schematic model will serve as the basis for an analysis of the MM5 simulation of Supertyphoon Herb. Special attention will be paid to the cyclone as it approaches Taiwan's Central Mountain Range (CMR). Comparisons will be then made in the vertical velocity fields associated with Herb to those of the conceptual model of Liu et al. as the Herb approaches the land feature. Three cases will be presented, each representing a definitive position of the TC relative to the CMR for comparative purposes.

## 4.2 Vertical Motion Well Before Landfall

Figures 4.2 through 4.6 represent Supertyphoon Herb at 0800 UTC on 30 July 1996. Figures 4.2 and 4.3 display an east-west cross-section of the vertical motion fields associated with the TC. These images are taken through a line of constant latitude of 22° 28′ N. Figure 4.3 is

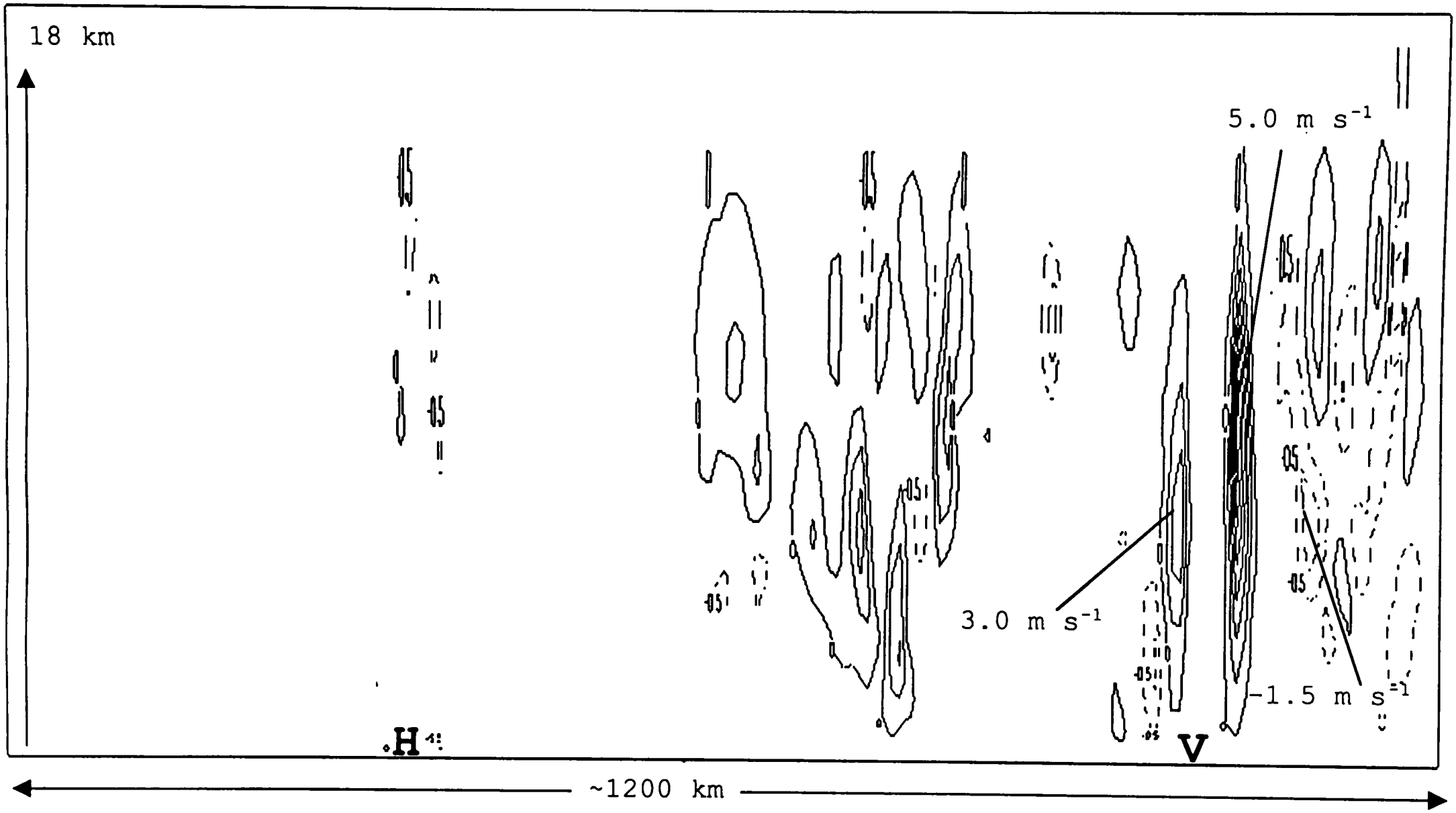


Figure 4.2. Upward (solid) and downward (dashed) motion in an east-west cross section at 0800 UTC 30 July. Contour intervals are 1.0 m $s^{-1}$ for upward motion and 0.5 m $s^{-1}$ for downward motion. The typhoon center is identified with a 'V' and the terrain with an 'H'.

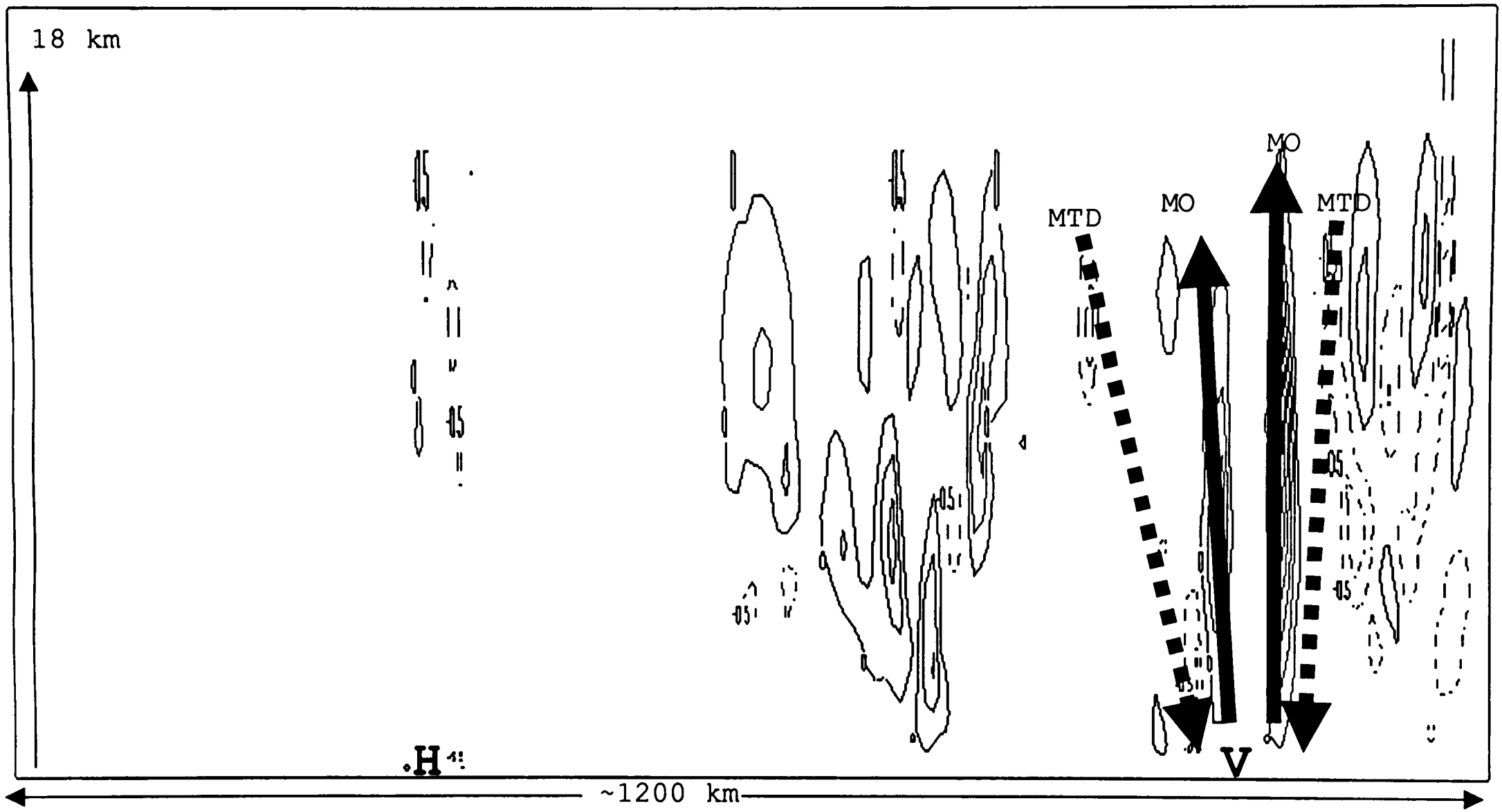


Figure 4.3. Best estimate of updraft (solid arrow) and downdraft (dotted arrow) regions relative to the eye at 0800 UTC 30 July. Other contours are as before, and abbreviations are given in the text. The typhoon center is identified with a 'V' and the terrain with an 'H'.

merely a reproduction of Figure 4.2 with the addition of identifiable features as compared to the conceptual model. At this time, the typhoon is quite far from Taiwan's CMR, about 725 km (450 mi) to its southeast. This scene is intended to represent a time when the mountain range has not yet begun to affect the structure or intensity of the TC. From this point forward, each cross-sectional image will span over the entire model domain in the horizontal, approximately 1200 km, as well as to an altitude of 18 km. Also for consistency, the best estimate of the center of the TC will be identified with a bold 'V' while the CMR is shown with an 'H'. Finally, upward motion will be shown with solid black isotachs while sinking motion and relative humidity (RH) will be shown in dashed black isotachs unless otherwise indicated. This style will remain consistent for all images shown throughout the chapter.

Overall, there is an evident east-west symmetrical nature to the vertical motion fields. It is immediately obvious that there exists two main outflow/spiral updraft (MO/SU) regions, each tilted radially outward with height (refer to Figure 4.3). This is consistent with the conceptual shown in Figure 4.1. As shown in Figure 4.2, the eastern MO is stronger in magnitude (peak values of 5.0

m $s^{-1}$ versus 3.0 m $s^{-1}$) than its western counterpart and also extends through a greater depth. Peak values in this and subsequent images were identified using the VIS-5D "probe" function.

Based on the isotach patterns, there is also an indication of alternating regions of upward and downward motion, which become weaker further out from the eyewall. Sinking motion is seen between the regions of upward motion and identified as moist downdrafts (MTD) in Figure 4.3. As with the updraft regions, the magnitudes of the downdraft regions are greater on the eastern side of the TC. A slight dry downdraft is found to exist to the inside of the MO areas, with average velocity values of about -0.25 m $s^{-1}$. This region does not appear on the plot, as the contour interval used in the graphic is too large. In fact, if DD regions were observed they were consistently weaker than the smallest isotach, never reaching values greater than -0.25 m $s^{-1}$. Thus, DD regions do not appear in any future images.

Figure 4.4 overlays relative humidity (RH, dashed) on regions of upward vertical motion within the model domain. As seen in the figure and extending up to about 15 km, the main outflow (MO) updraft regions correlate well with the

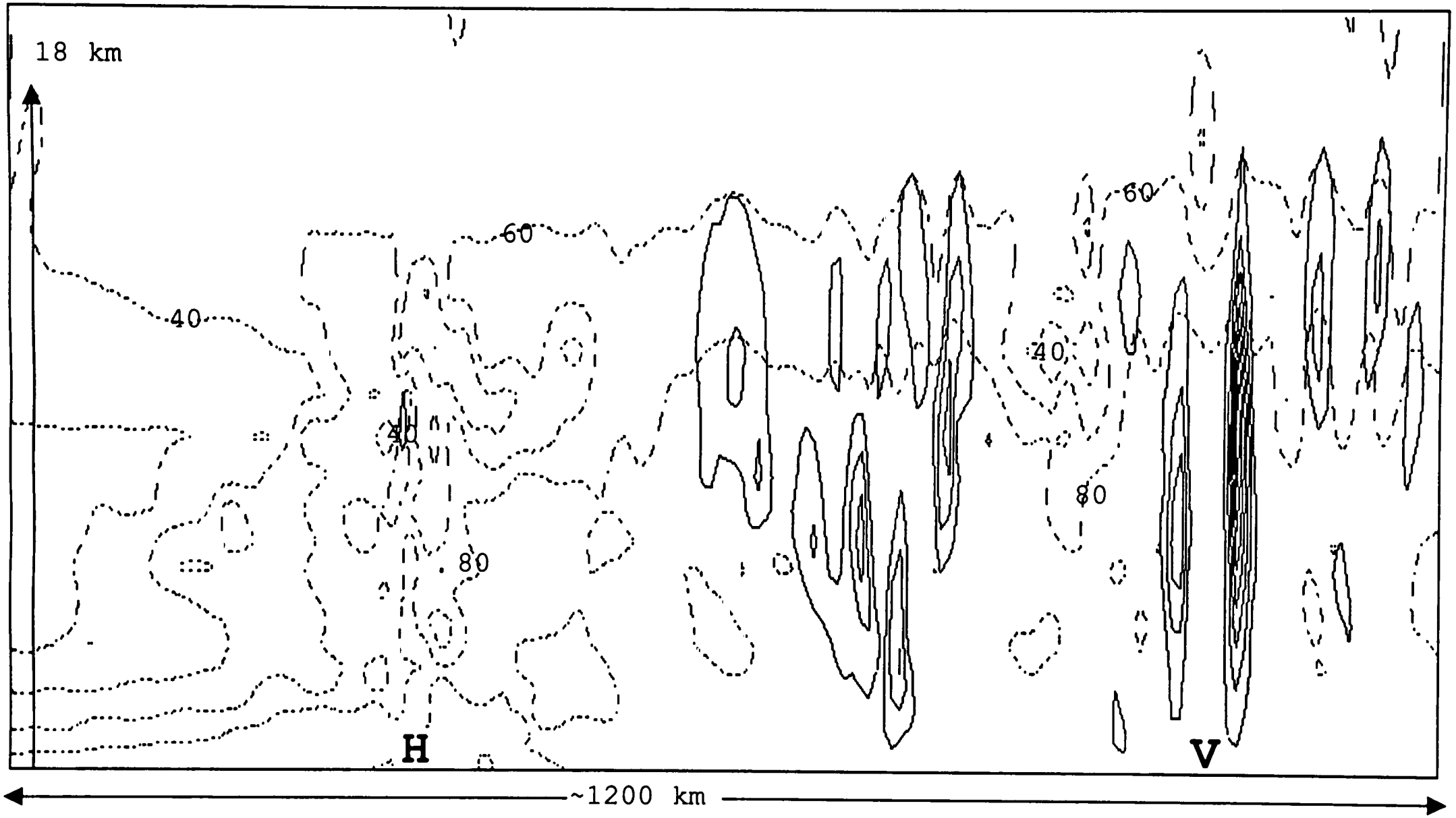


Figure 4.4. Upward motion (solid) and RH (dashed) in an east-west cross section at 0800 UTC 30 July. Contour intervals are 1.0 m $s^{-1}$ for upward motion and 20% for RH. The typhoon center is identified with a 'V' and the terrain with an 'H'.

highest RH areas. The cores of both MO's are found in air with RH values of 90%-100%, with outer spiral rainband areas coinciding with rising motion regions mainly within air of RH values 80%-100%. As these regions appear well outside a 200 km radius at this time, they are not labeled. There was relatively drier air (RH values between 60% and 80%) found at mid-levels (4-7 km) directly above the CMR. As will be shown later through trajectory calculations this air is eventually advected into the mid-levels on the eastern side of the TC, contributing to its overall weakening as it approaches Taiwan and the CMR.

One major difference noted in comparison to the conceptual model is found within the moist downdraft regions (MTD). Liu et al. refer to these regions as "moist" downdrafts, inferring that RH values are higher relative to their surroundings. As seen in Figure 4.4, the isohumes associated with MTD regions are within the 60%-80% range and tend to protrude toward the surface, indicative of relatively drier air penetrating downward. In comparison to the surroundings, the air associated with these downdrafts appears to be somewhat drier, particularly in the first set of MTD's radially outward from the eye.

In fact, the first western MTD region contains air with RH values near 40% just to its west!

Trajectory calculations (not shown) were also conducted to determine the origin of air parcels comprising the strongest updrafts. Calculations were performed for both MO's and other regions exhibiting significant rising motion (greater then 2.0 m $s^{-1}$, say) on both the east and west side of the TC. For this case, air parcels on the western side of the eye typically originated from the eastern half of the cyclone and spiraled upward, exhibiting a helix-like structure. Moreover, an area between 1 km and 4 km with RH values greater than 80% on the eastern side provided most air parcels for the strongest western updrafts. Consequently, eastern updraft air parcels originated in the same 1 km to 4 km layer with RH values greater than 80%, but in the vicinity very near to the eye and well within the convective eyewall region (near the MO).

From an additional perspective, Figure 4.5 displays a north-south cross-section of the vertical motion fields through a line of constant longitude (126° 71′ W). This view is considered approximately perpendicular to the TC track. Previous research has dictated cross-sections taken

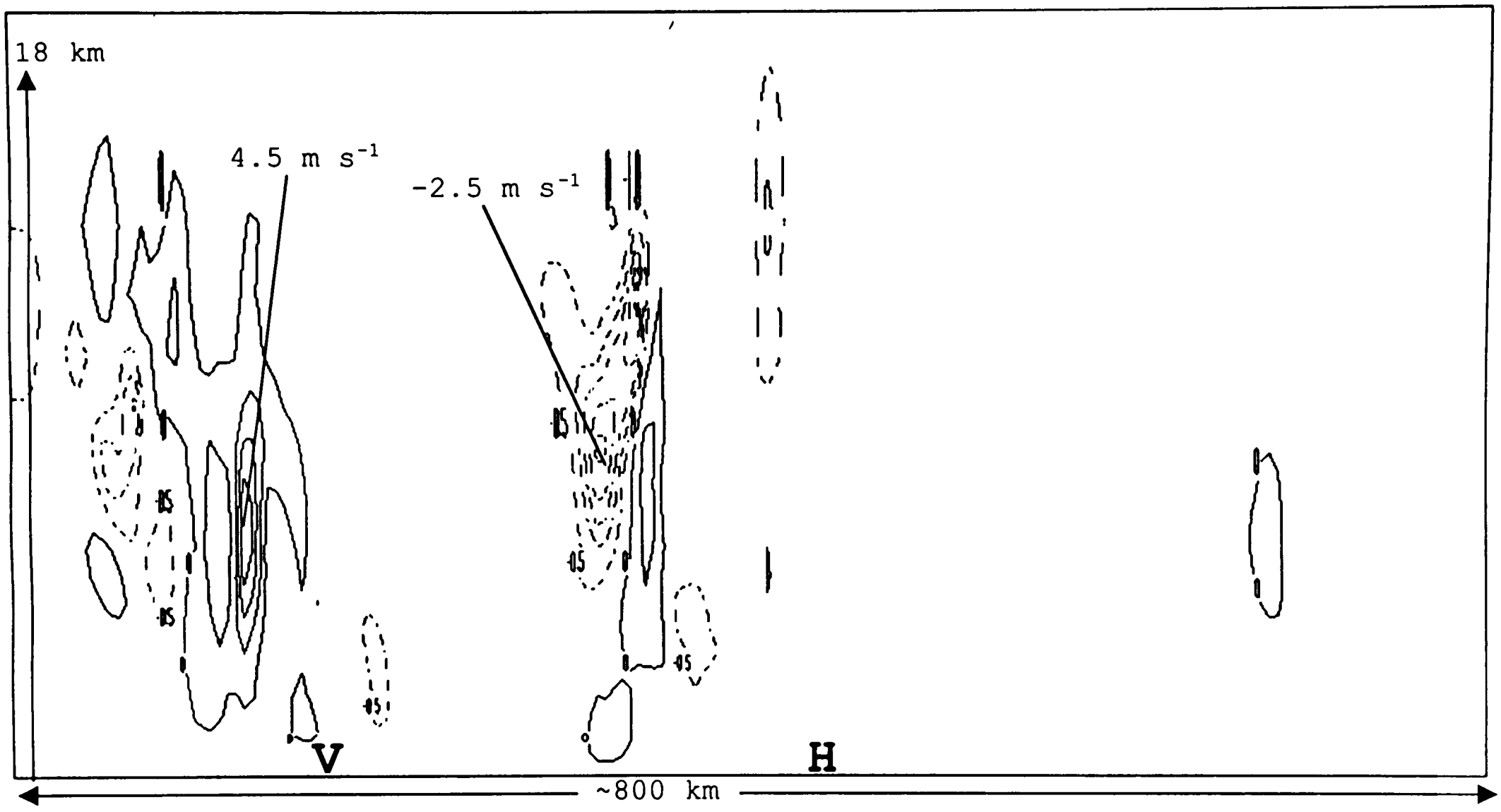


Figure 4.5. Upward (solid) and downward (dashed) motion in a north-south cross section at 0800 UTC 30 July. Contour intervals are 1.0 m $s^{-1}$ for upward motion and 0.5 m $s^{-1}$ for downward motion. The typhoon center is identified with a 'V' and the terrain with an 'H'.

normal to the TC path as convention. While all of the features observed in the conceptual model as well as the east-west cross-section are not as evident, a strong, southerly SU is seen just south of the eye as well as the overall alternating upward and downward motion patterns. It appears, however, from this image that for cross-sections taken normal to the typhoon path at this position, the conceptual model does not hold well as the horizontal distance is much too large (~ 400 km) for that of a typical TC eyewall region.

Figure 4.6 displays a horizontal plot of rising motion and wind vectors at the 3 km level. The MO's are highly evident (seen as small black dots) immediately to the northeast and northwest of the center of circulation of the TC. It is also evident that the majority of rising motion occurs to the south and west of the typhoon eye. These regions are found to correlate quite well with the areas of highest cloud water content (not shown), indicative of the moist convective processes occurring within this sector of the TC.

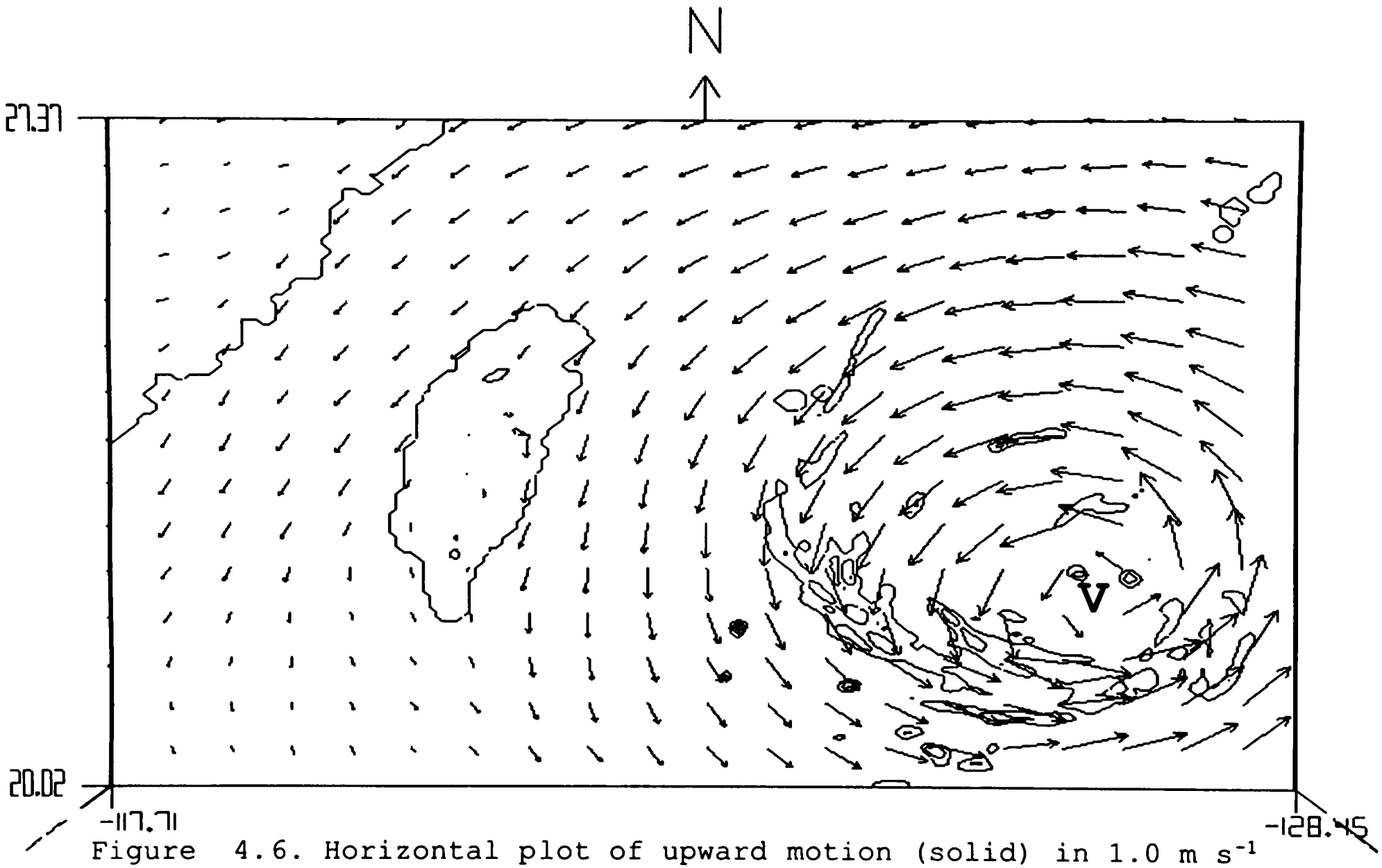


Figure 4.6. Horizontal plot of upward motion (solid) in 1.0 m $s^{-1}$ intervals and wind vectors (60 km spacing) at 3 km at 0800 UTC 30 July. Latitude and longitude references are indicated at the model boundaries. The typhoon center is identified with a 'V'.

## 4.3 Vertical Motion Just Before Landfall

Figures 4.7 through 4.11 reveal Supertyphoon Herb at 0400 UTC 31 July 1996, some 20 hours after the "well before" case, yet approximately 6 hours prior to landfall. The eye of the TC is estimated to be 400 km (250 mi) to the southeast of the CMR. This period begins the "transition zone" where the identifiable features observed to this point begin to break down. Vertical cross-sections are taken at 24° 65′ N (east-west cross-sections) and at 123° 11′ E (north-south cross-sections). At this time, the northeasterly flow observed on the west side of the typhoon is found directly over the CMR. This particular time is chosen to represent Taiwan's CMR significantly affecting the strength and structure of the typhoon. Figures 4.7 and 4.8 are cross-section plots of the vertical motion fields in this "just before" landfall scenario. Isotach contour intervals and line style in the accompanying figures are as in the previous case.

The MO regions, which were very symmetrical about the eye of Herb in the "well before" case, are now a bit more difficult to identify. The eastern MO is no longer as robust, having shrunk both in magnitude (3.0 m $s^{-1}$ maximum value) and in vertical structure. The western MO is now

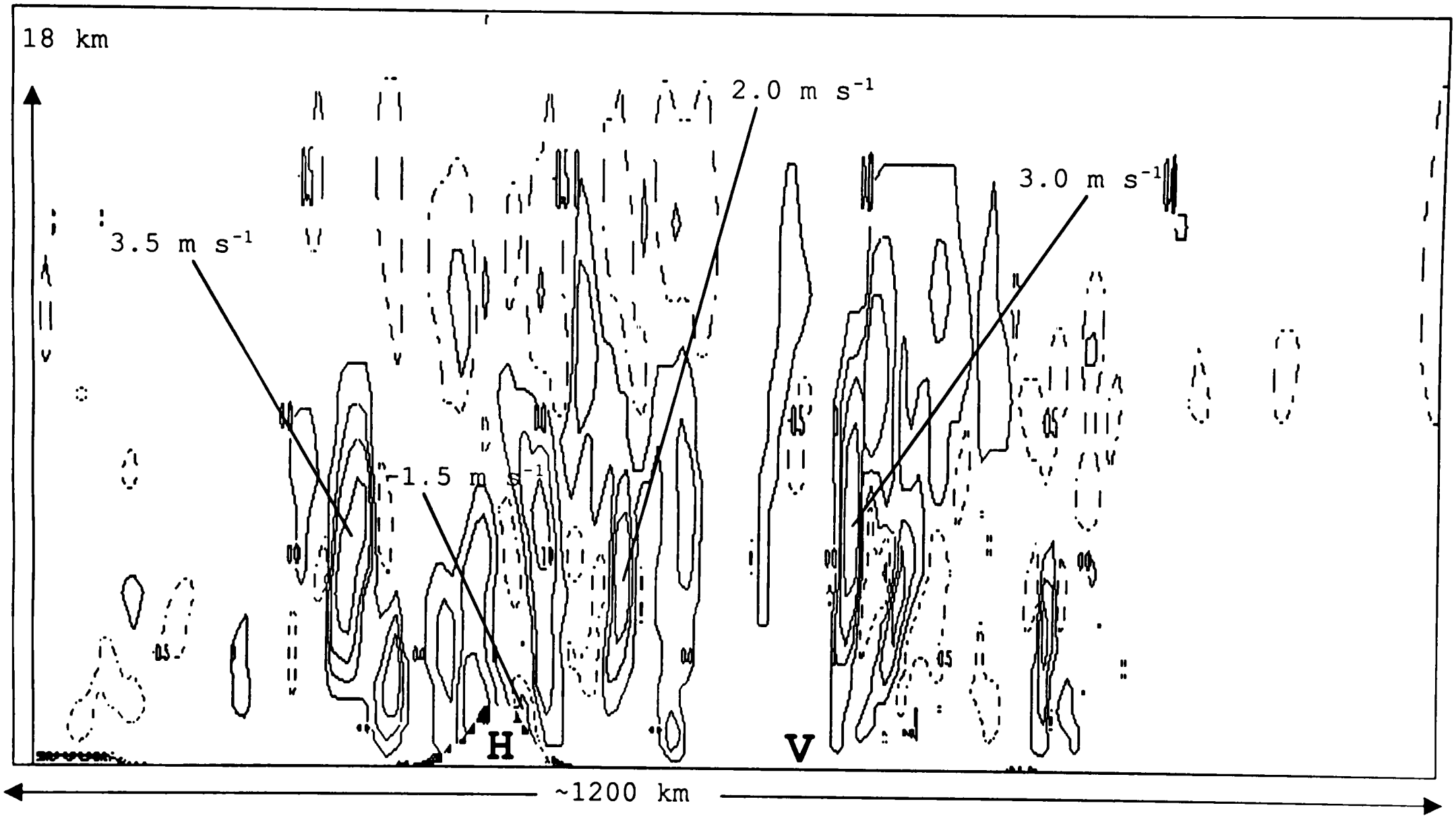


Figure 4.7. Same as in Figure 4.2 but for 0400 UTC 31 July.

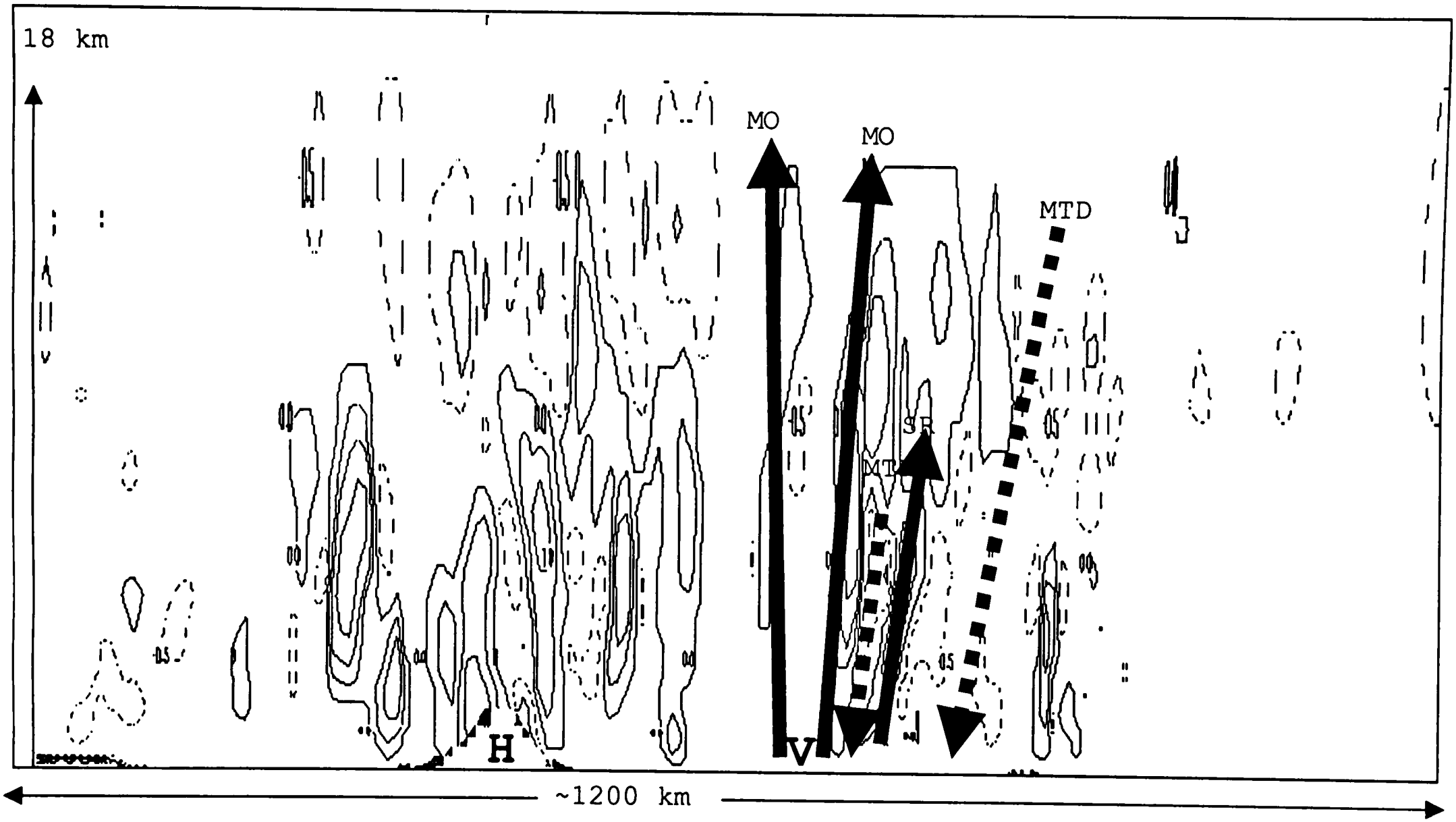


Figure 4.8. Same as in Figure 4.3 but for 0400 UTC 31 July.

much weaker as well. It has contracted in the vertical as compared to the previous time with most intense rising motion confined between the 5 km and 7 km levels. The MTD regions found on the eastern side of the TC have strengthened, particularly below 9 km, so as to almost "choke" or cutoff the MO and spiral rainband/spiral updraft regions that had previously existed. It should be noted as well that the former western MTD, which was weak to begin with, has vanished. In fact, very little organized structures exist at this time on the western side of the TC.

Figure 4.9 is a plot of the RH and upward motion for the typhoon at this position. This plot displays several interesting occurrences. First, the eastern half of the TC has dried out considerably, particularly to the east the eyewall region, with air containing RH values of 30% and 40% entering into mid-levels. Recall from Figure 4.1 that this region, through the MTD's, is partially responsible for advection of high $\theta_e$ back into the TC environment. Bender et al. (1985) found through numerical simulation that a mountain tended to reduce the amount of latent heat and kinetic energy advected into the storm circulation as it approached and passed over the terrain feature. This

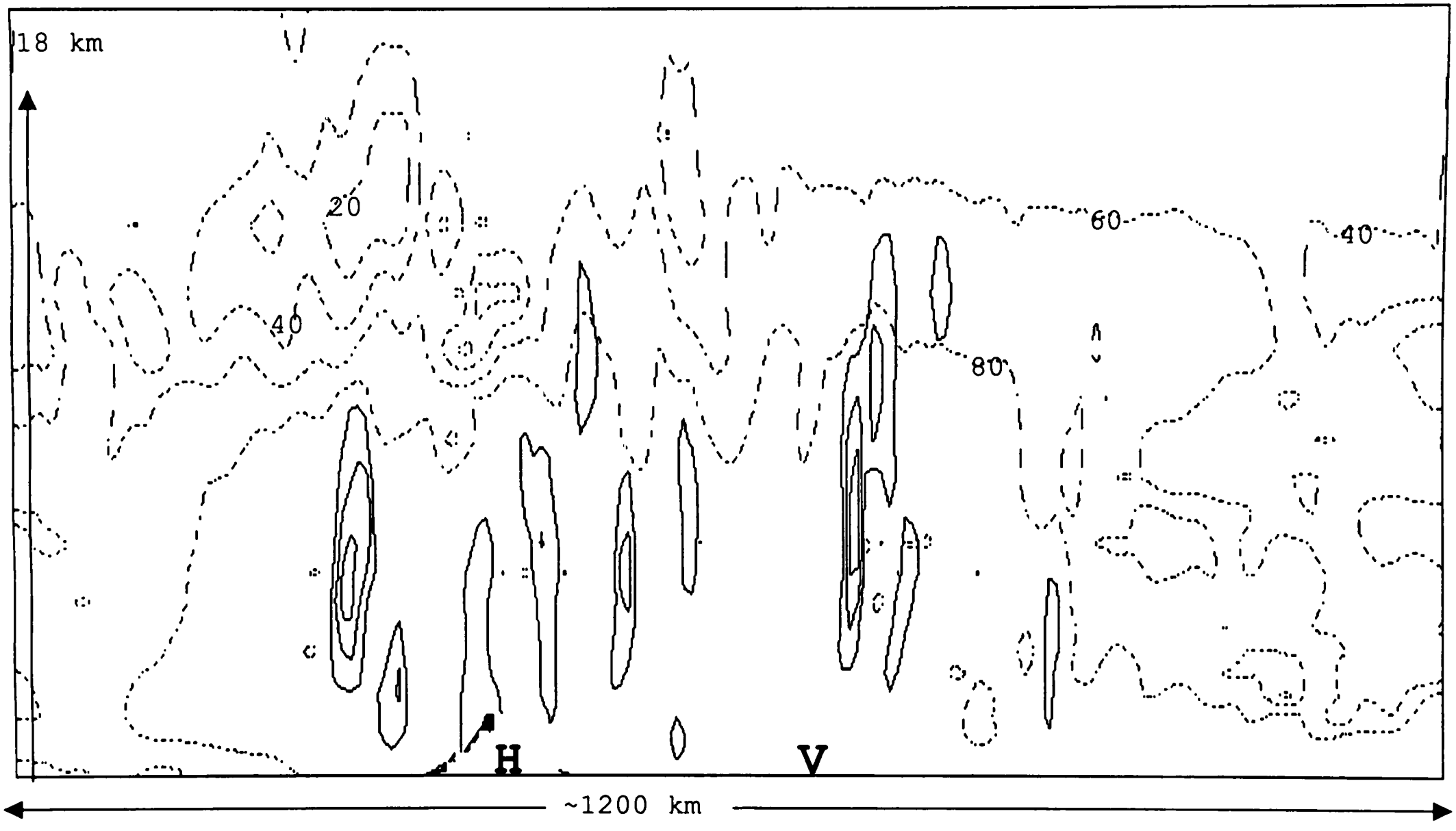


Figure 4.9. Same as in Figure 4.4 but for 0400 UTC 31 July.

appears to be a similar case, albeit some 400 km prior to landfall. In comparison to the "well before" case, the air over the CMR has moistened to values greater than 80% in the mid-levels with the approaching TC.

The MO regions are still moist as in the previous case, although a new, large RH difference appears just to the west of the weakened western MO directly above the CMR. The DD's and MTD's have also remained relatively dry (RH values near 60%). The air associated with the DD's, MO's and MTD's has remained moist with RH values greater than 80% to altitudes of 9 km. With moisture in place, the lack of any significant upward motion acts to further weaken or inhibit any additional convection within the eyewall.

In a north-south cross-section (Figure 4.10), it is interesting to note the absence of any well-defined upward motion other than in a few, random spots. The exception is an intense area of rising motion just to the south of the eye. This region can be seen in greater detail in Figure 4.11, where a broad region of upward motion exists along the southern/southeastern edge of the eyewall. It will later be shown that this region correlates quite well with an area of stronger positive potential vorticity that appeared to originate over the CMR. As hypothesized before

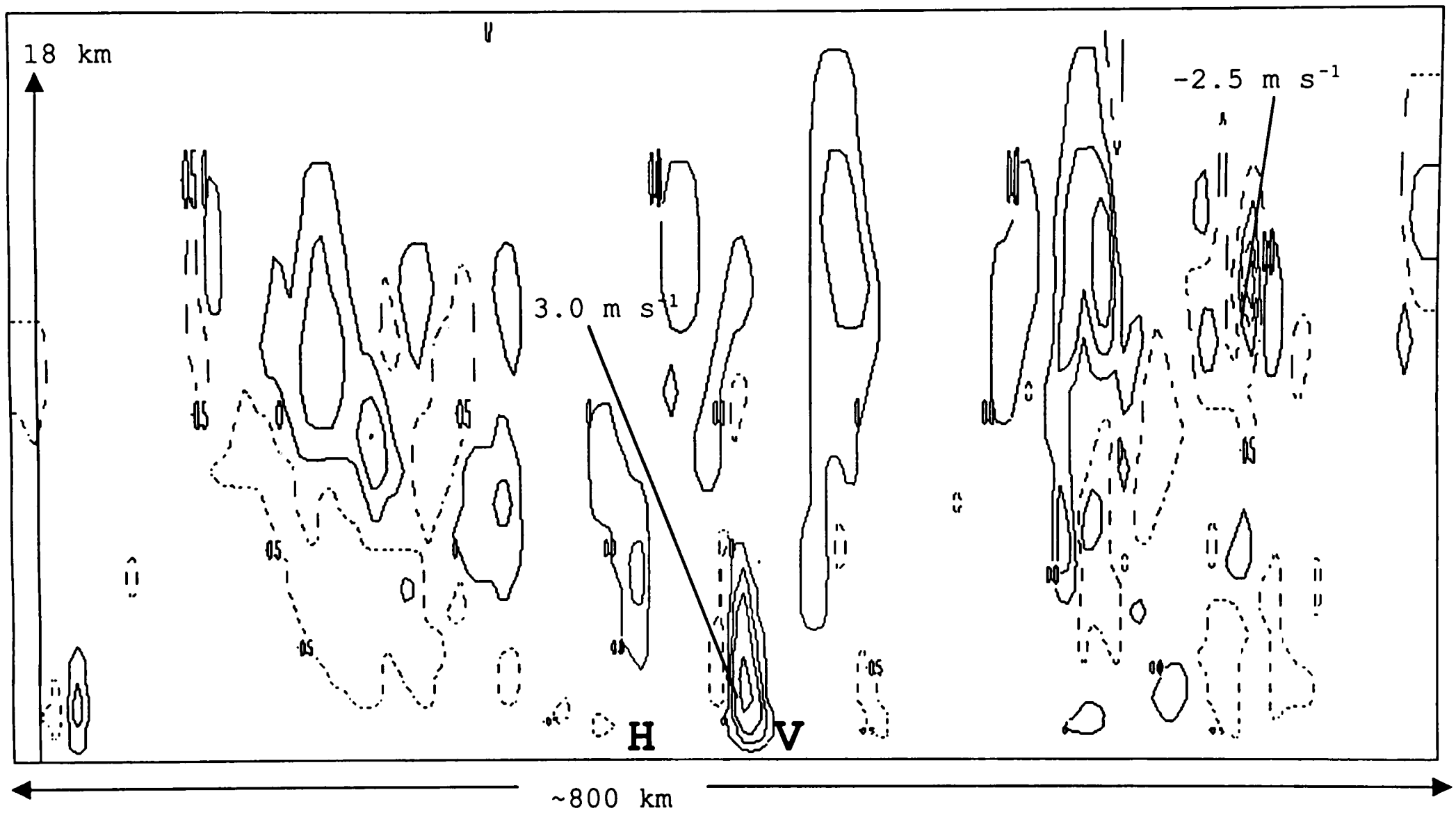


Figure 4.10. Same as in Figure 4.5 but for 0400 UTC 31 July.

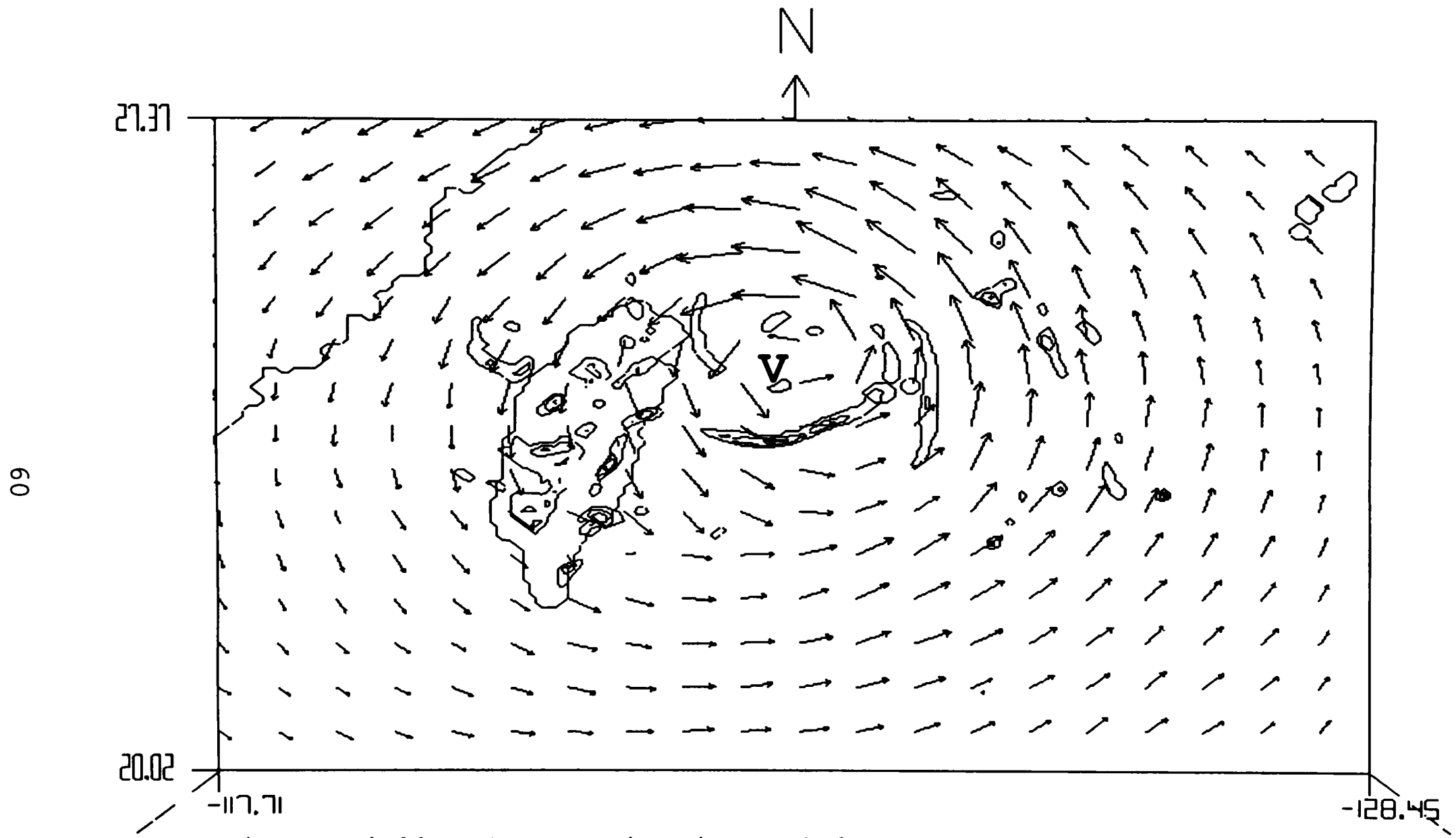


Figure 4.11. Same as in Figure 4.6 but for 0400 UTC 31 July.

and confirmed here, the radial-height conceptual model of Liu et al. does not hold up well for cross-sections examined normal to the cyclone track regardless of position relative to the terrain feature.

Trajectory calculations (not shown) were again performed on the stronger updraft regions (SU's/MO's) on both the east and west sides of the typhoon. On the west side, updraft air parcels continued to originate from the east, although at higher altitudes and with lower RH values as compared to the "well before" case. Overall, parcels were advected from altitudes of 7 km to 9 km, with RH values between 70% and 90%. The eastern updraft regions were again found to emanate from the eastern eyewall region, but from lower RH, higher altitude air (3 km-5 km). Figure 4.11 depicts a horizontal plot of upward motion and wind vectors at 3 km. Most of the rising air is concentrated within two main areas, to the southeast of the eye as well as around the perimeter of the CMR. As in the "well before" case, these concentrated areas of rising motion correlate quite well with the highest concentrations of cloud water (not shown) for this position of the TC.

## 4.4 Vertical Motion Over Land

The third time analyzed occurs as Herb's center of circulation passed directly over Taiwan's CMR, at 1000 UTC 31 July 1996. This time represents the cyclone position just after landfall and is indicative of the CMR affecting both east and west flow patterns of the typhoon. The figures that accompany this time period are 4.12 through 4.16. The east-west cross-sections (Figures 4.12, 4.13, 4.14) are taken at a constant latitude of 24° 84′ N with contour intervals and line styles as in previous figures. Figures 4.12 and 4.13 display the vertical motion fields as Herb traverses the CMR. At this time, the comparison to the conceptual model has become extremely difficult. A large region of rising motion exists directly over the CMR, bounded by heights of 5 km and 12 km. Only the MO regions remain identifiable, becoming much weaker and contracting horizontally. Vertical speeds less than 0.5 m $s^{-1}$ are most frequently noted with the updrafts. A relatively small but strong region of sinking air is also observed just above and to the east of the CMR at a height of approximately 4 km, extending toward the surface between the two MO updrafts. Although it would appear from the conceptual model comparisons that this feature is a 'DD' (based on

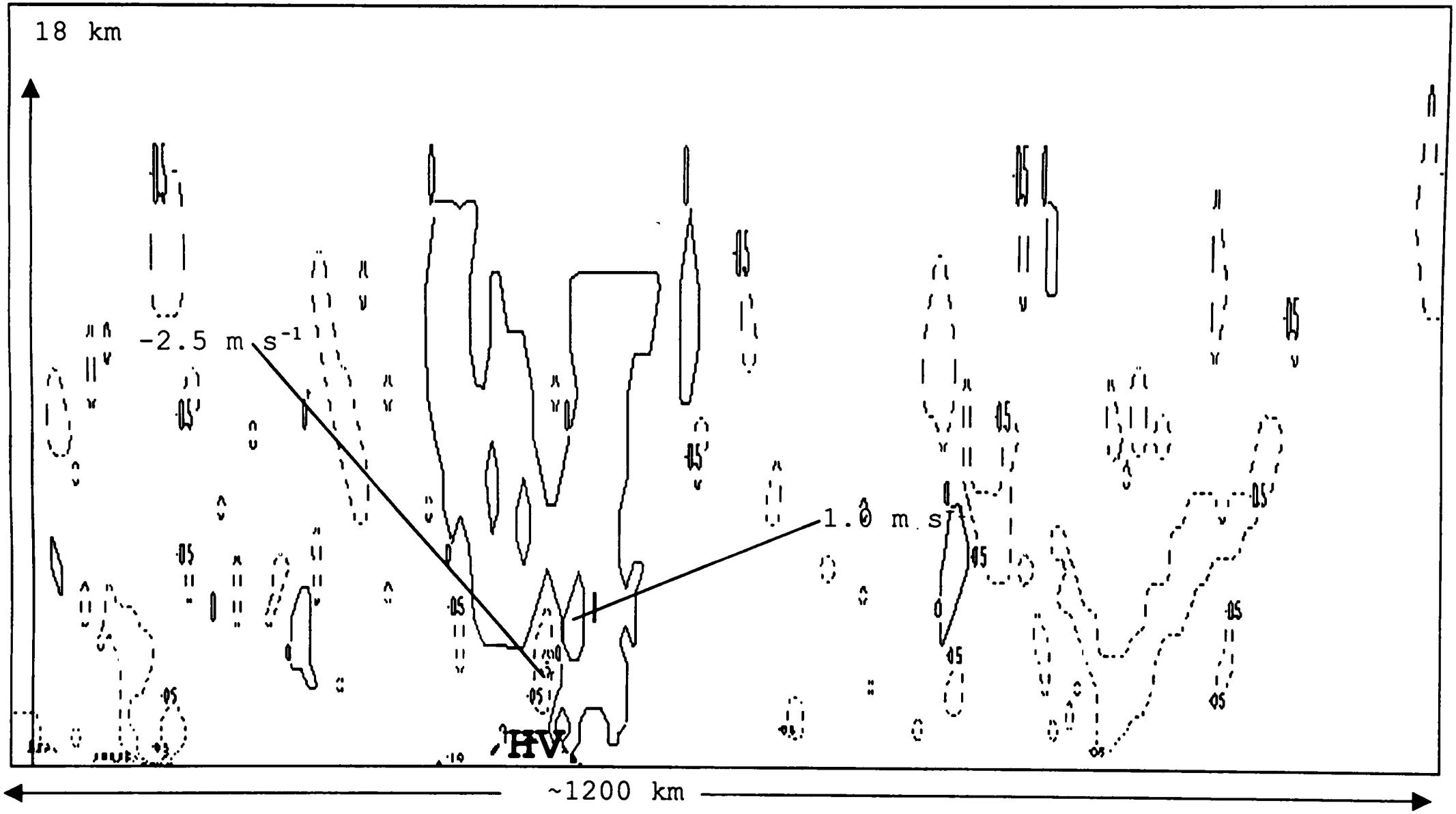


Figure 4.12. Same as in Figure 4.2 but for 1000 UTC 31 July.

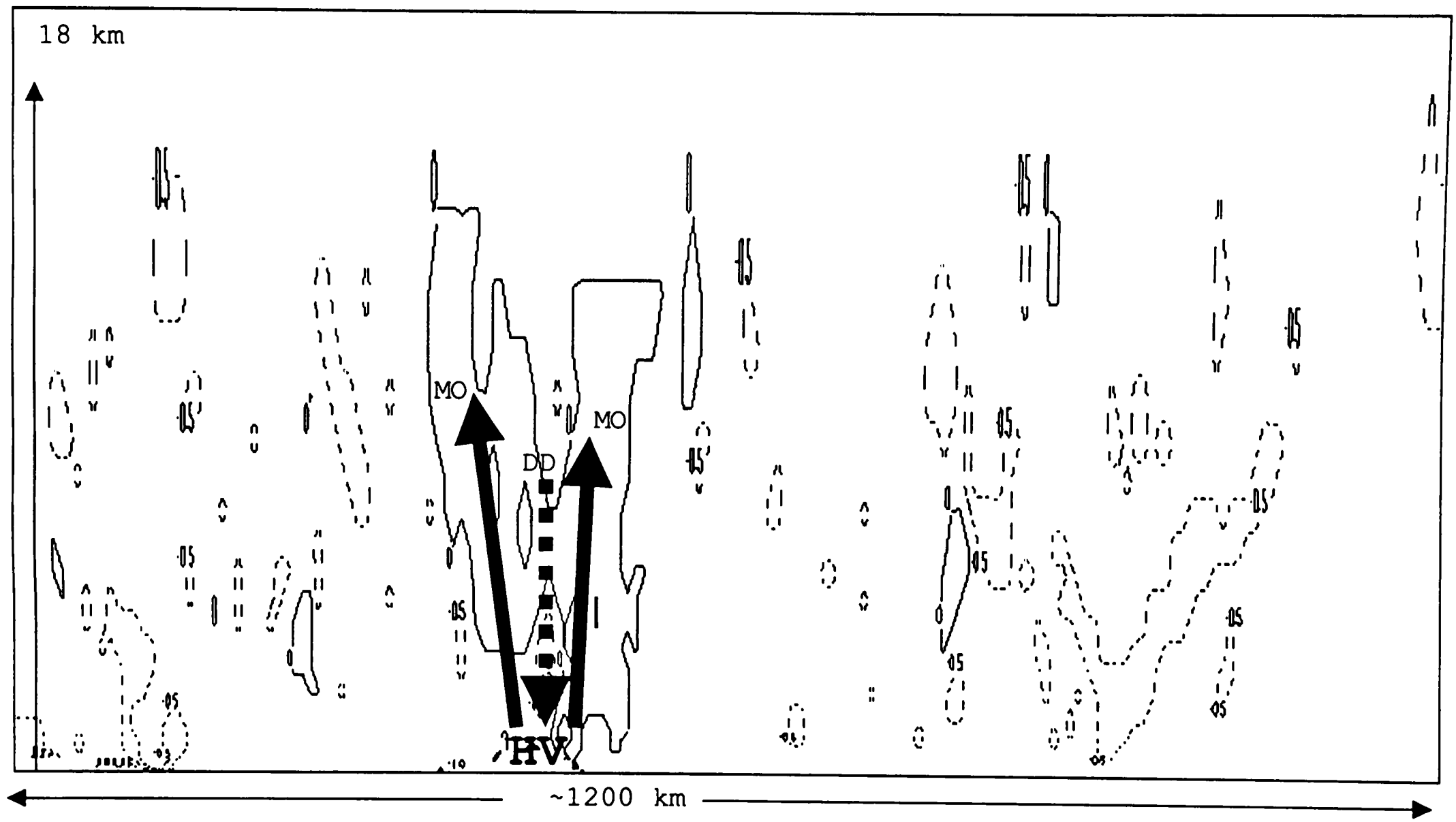


Figure 4.13. Same as in Figure 4.3 but for 1000 UTC 31 July.

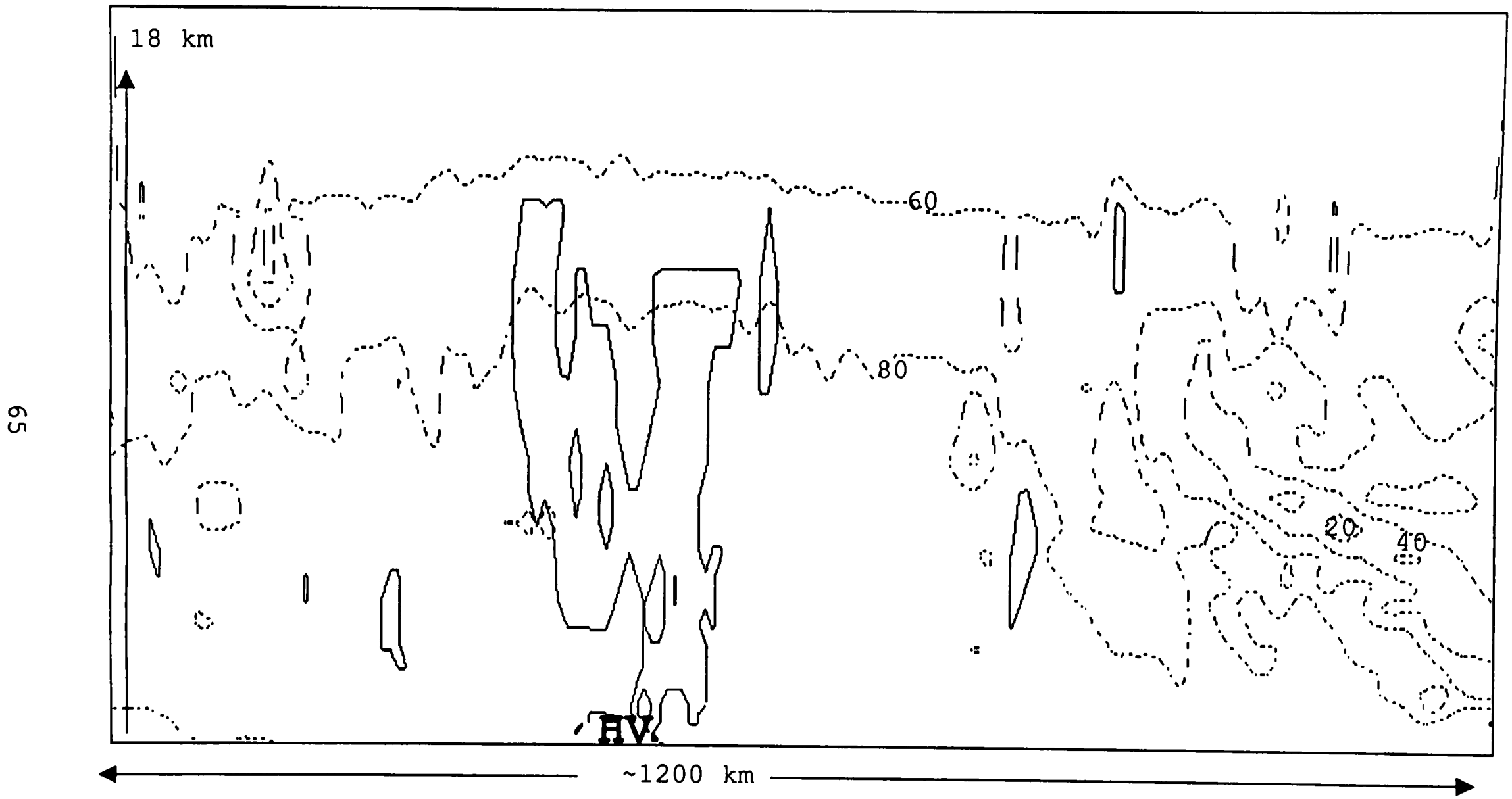


Figure 4.14. Same as in Figure 4.4 but for 1000 UTC 31 July.

location), RH values are much too high to be considered 'dry' and thus refute the notion. Thus, this area of sinking air is likely the result of the terrain interaction, with gravity wave breaking resulting in downsloping winds. Radially outward from the TC, there are no obvious MTD or spiral rainband areas, although both have appeared in previous plots. Figure 4.13 further exemplifies the breakdown of the conceptual model at this stage, with only weak MO's identified.

Figure 4.14 displays an overlay of RH with regions of upward motion in solid black. Over the terrain feature, the air is moist, with RH values between 80% and 100% up to about 6 km, as would be the expectation in the vicinity of a typhoon. It is even more surprising, however, to see the moisture remain in place over the terrain both before and during the passage of the TC.

Well to the east of the landfalling typhoon, the air remains extremely dry, with RH values between 30% and 60%. This is indicative of the dry air, as seen in the previous case, continuing to be advected into the TC environment, weakening it further. It is also of interest to note that this region of dry air has shifted west with the propagating typhoon.

The north-south plot through a line of constant longitude (121° 66′ E) is shown in Figure 4.15 for this position. It is taken parallel to the orientation of the CMR as well as the track of the TC. This plot further supports the breakdown of the conceptual model. None of the few features observed in the previous cases are seen in this image.

Trajectory calculations for this time were performed as well. Each MO region immediately to the outside of the eye of Herb contained air parcels that originated very high into the atmosphere over the CMR and immediately to its west. Consistent heights of greater than 7.0 km and RH values of less than 50% were found as sources for these air parcels that ended up in updraft regions associated with the MO′s.

Finally, a horizontal plot at 3 km of wind vectors and upward motion for this case is presented. Note the overall spatial absence of upward motion regions, except in the southwest quadrant. As would be expected with the weakening cyclone, upward motion areas become less and less prominent, further exemplifying the breakdown of the cyclone as compared to the conceptual model.

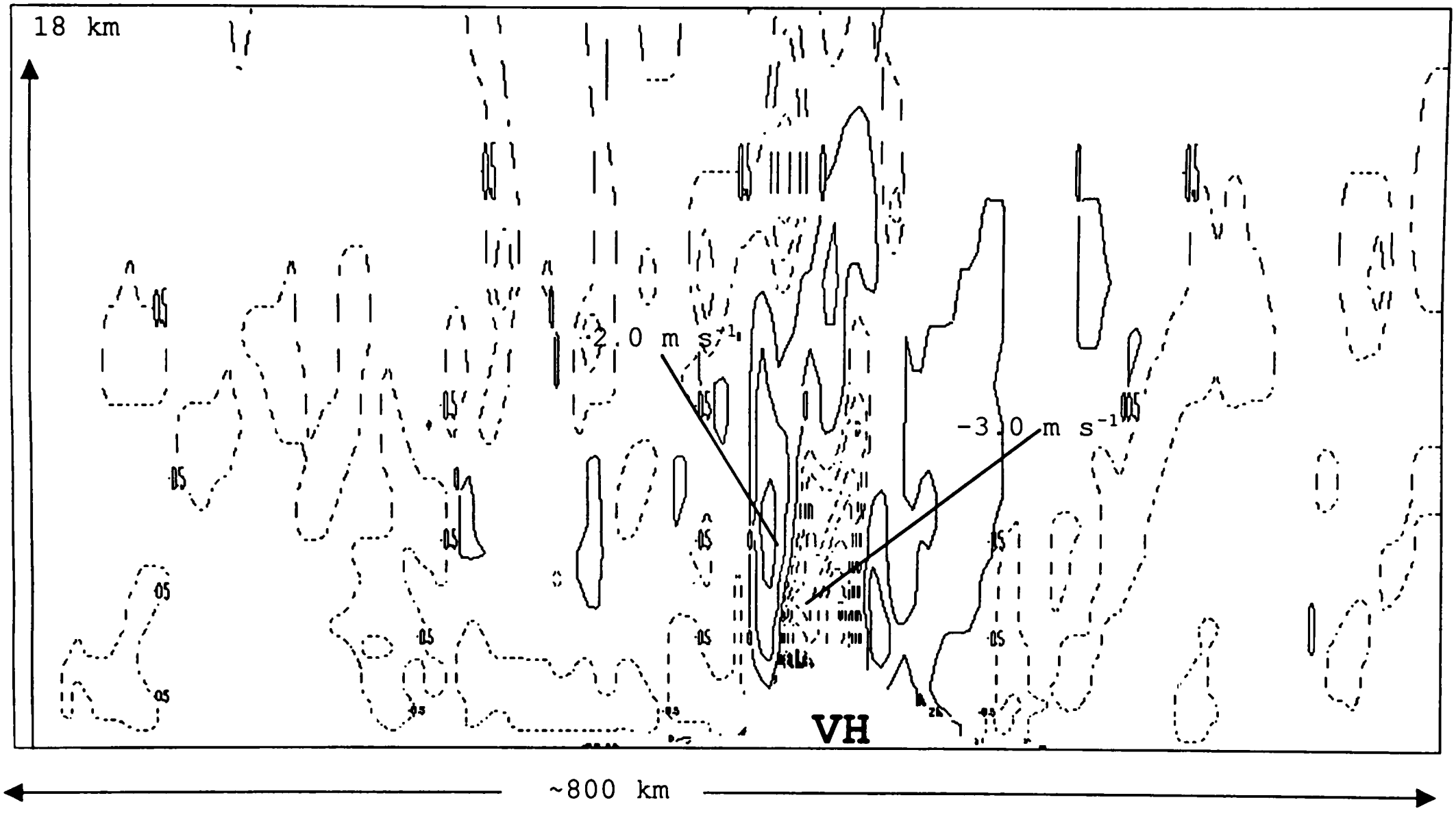


Figure 4.15. Same as in Figure 4.5 but for 1000 UTC 31 July.

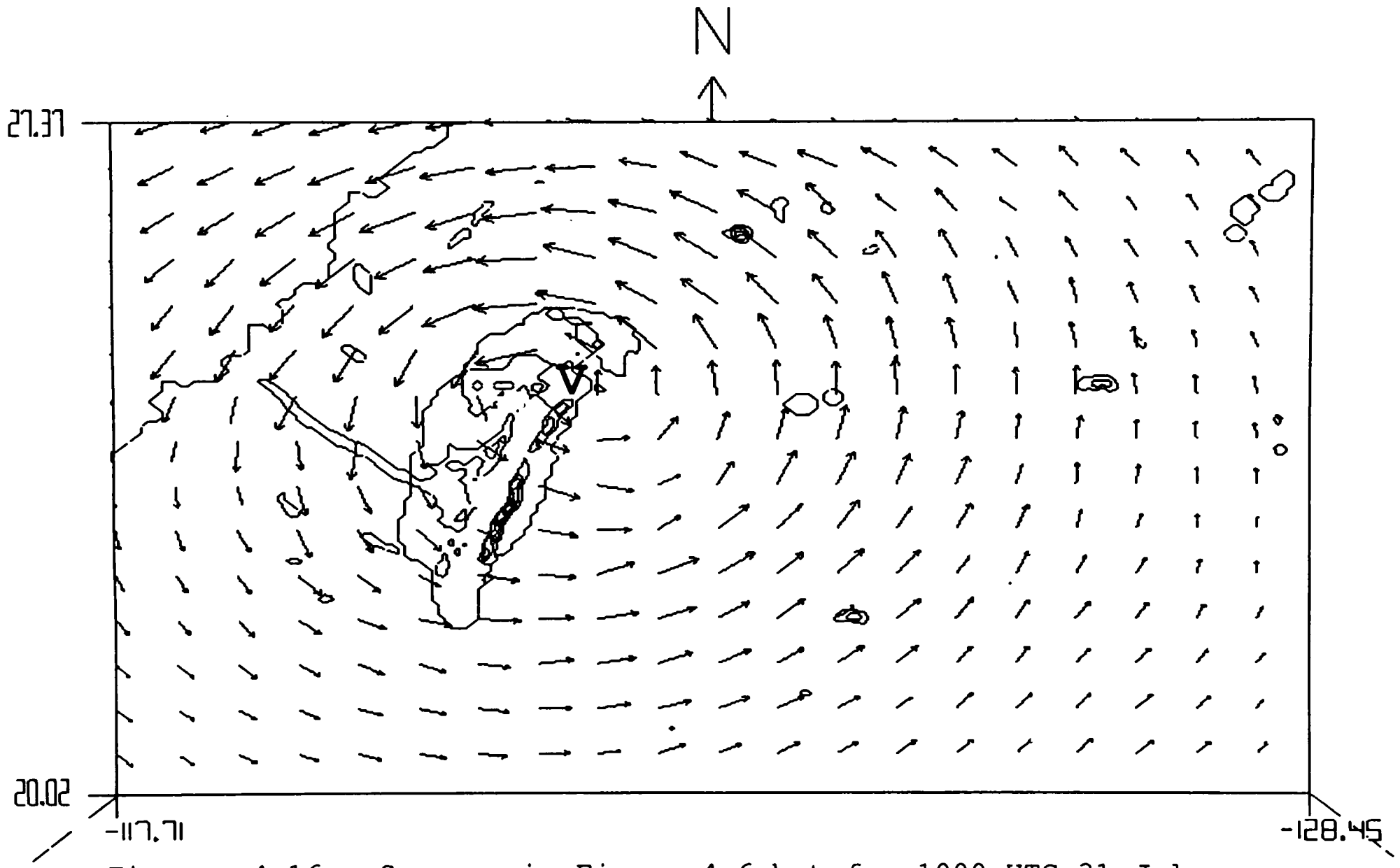


Figure 4.16. Same as in Figure 4.6 but for 1000 UTC 31 July.

# CHAPTER 5

# POTENTIAL VORTICITY ANALYSIS

## 5.1 PV Structure Analysis

Figures 5.1 through 5.6 depict the simulated typhoon as a positive PV anomaly as well as the associated potential temperature ($\theta$) and vertical component of absolute vorticity (AV) fields at three positions along its path. For comparative purposes, the east-west cross section locations (at a constant latitude) and times are exactly as in the previous chapter. The best estimate of the surface center of circulation are again labeled with a 'V' and the CMR with an 'H'.

### 5.1.1 Well Before Landfall

Figure 5.1 shows a somewhat symmetrical version of Herb as a positive PV anomaly well before landfall at 0800 UTC 30 July. PV is contoured in intervals of 5 PVU (1 PVU= $1x10^{-6}$ $m^2$ K $s^{-1}$ $kg^{-1}$) with maximum values identified via the VIS-5D "probe" function within the convective eyewall region of the TC. The positive anomaly at this time is quite symmetrical both in magnitude and structure about the center of the TC to a height of approximately 5 km (labeled

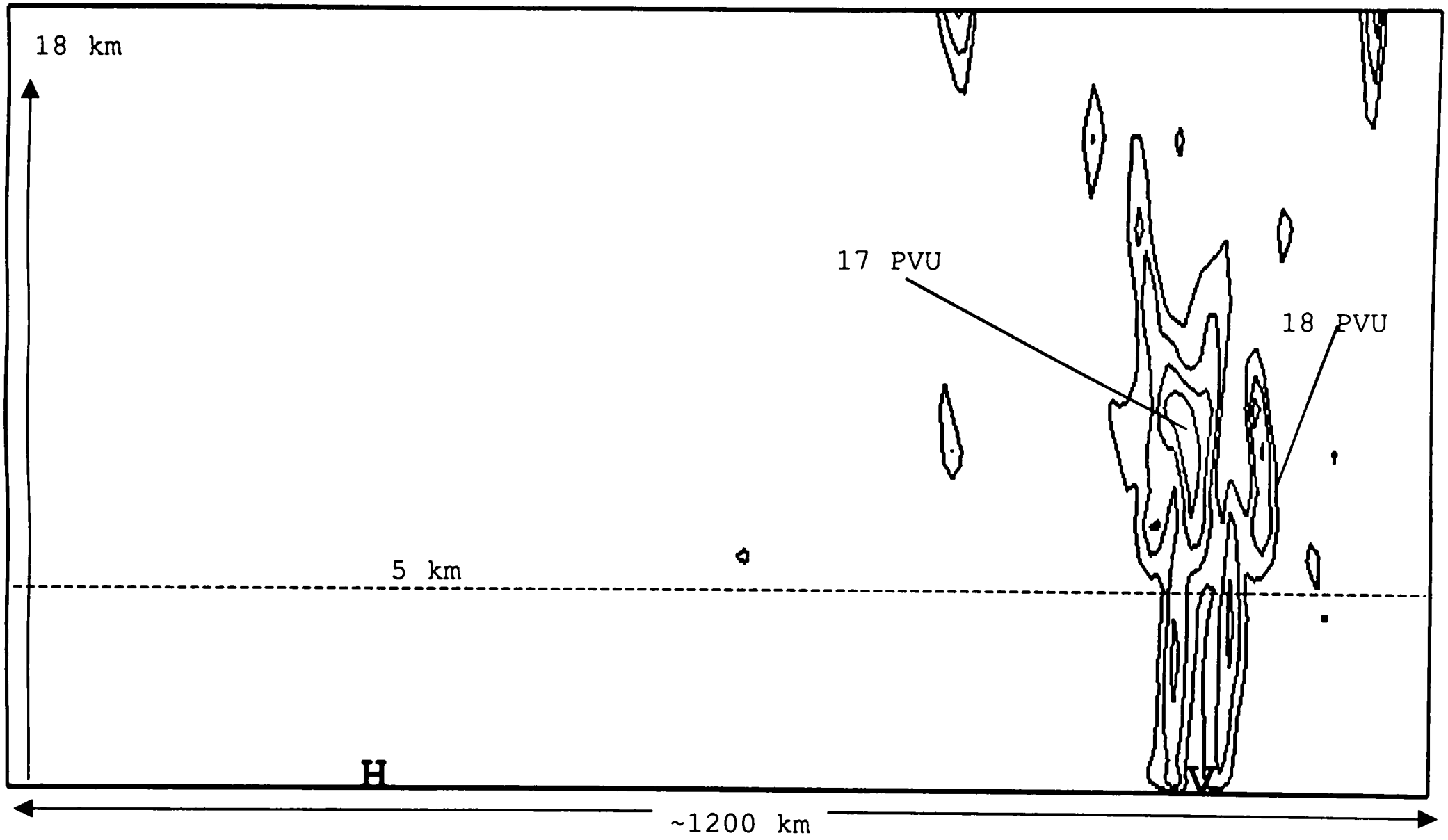


Figure 5.1. Vertical east-west cross section of positive PV well before landfall, 0800 UTC 30 July 1996. Contour interval is 5 PVU from 5 to 20 PVUs. The eye is identified with a 'V' and the mountain with an 'H'.

on Figure 5.1). The anomaly has an estimated radius of approximately 150 km, comparable to that of the eyewall region of a TC. There is an identifiable westward tilt of positive PV extending from 7 km to 12 km, slowly decreasing in strength with height. This is consistent with Figure 1 of Wu and Wang (2000), where a vertical cross section of positive PV displays a similar structure with a distinct westward tilt of the anomaly above 7 km in a TC.

Also of interest in Figure 5.1 immediately surrounding the eye is the radial tilt outward of both the east and west segments of the positive PV anomaly. This corresponds well with the main outflow (MO)/spiral updraft (SU) regions identified and described in Chapter 4. As expected in a strong region of upward motion, higher values of the vertical component of absolute vorticity and thus PV exist. Coupled with the diabatic heating that occurs within the eyewall, the expectation for increased positive PV values within these MO regions is evident. In the eye region there is little or ño positive PV, represented by a single symmetric contour up to a height of about 4.5 km. PV values within the eye are less than 1 PVU on average at this location during this time.

Figure 5.2 shows the potential temperature and absolute vorticity fields for this time. The AV fields match quite well with the PV anomaly, particularly within the westward tilt seen above 7 km. The relative maximum values of PV and AV also coincide very well at this time. The $\theta$ field appears most tightly packed around the 7 km height, which is coincident with the greatest positive PV regions.

### 5.1.2 Just Before Landfall

Figure 5.3 represents the TC just before landfall at 0400 UTC 31 July. Contour intervals, units and labels are as in the previous figure. Overall, the positive PV symmetry of the storm is quite similar to the previous time. In terms of magnitude, the both east and west areas have remained similar, as identified in the Figure 5.3. The largest PV values found on the western side have stretched horizontally, with highest values now around 15 PVU.

The westward tilt exhibited at the previous time still exists, though it has shrunk vertically to a maximum altitude of about 9 km and is not as definitive. The eastern region has weakened at higher altitudes as well,

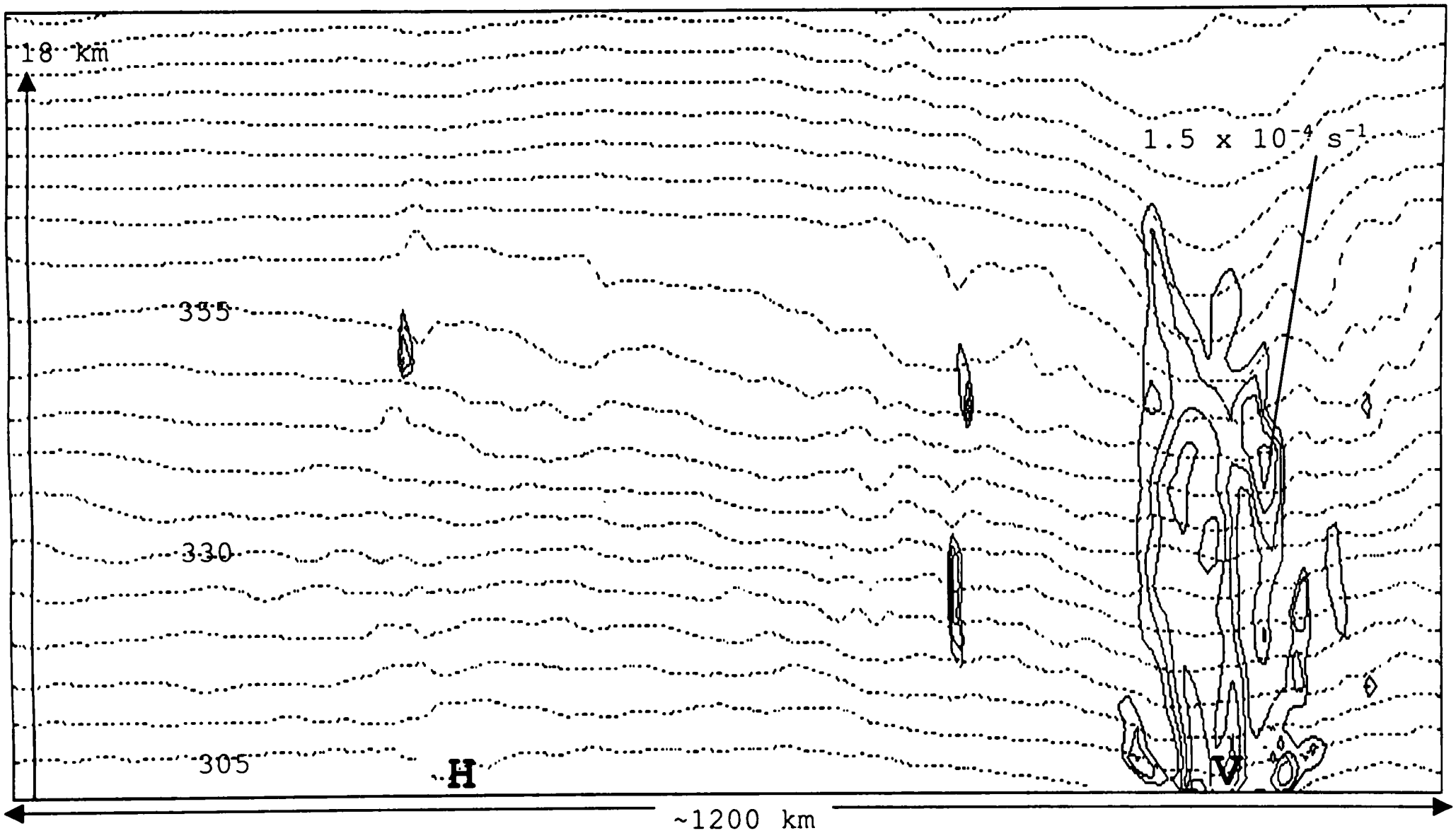


Figure 5.2. Vertical east-west cross section of positive absolute vorticity and potential temperature well before landfall, 0800 UTC 30 July 1996. AV contour interval is 2.5 x $10^{-5}$ $s^{-1}$ and potential temperature is 5 K. The eye is identified with a 'V' and the terrain with an 'H'.

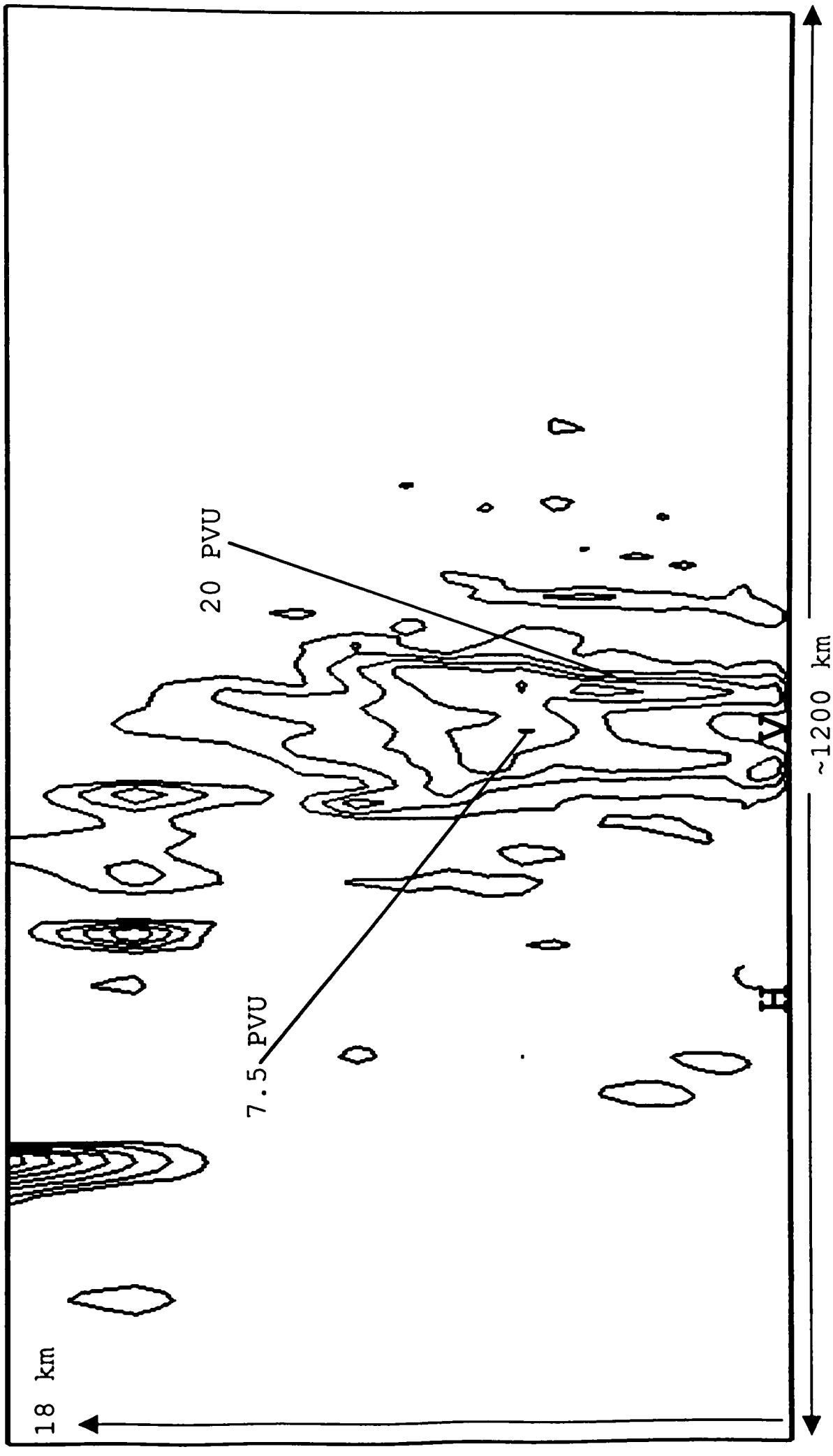


Figure 5.3. Same as in Figure 5.1 but for 0400 UTC 31 July 1996.

with no indication of a radially-outward tilt to the PV as seen in the previous image. Vertically, the eastern anomaly continues to extend to heights of 10 km. In comparison to the last time frame, the strongest positive PV areas have become elongated and propagated toward the surface.

The entire anomaly appears to have increased its radius to approximately 200 km. This is true throughout its vertical extension. In the eye region, PV values overall have increased slightly with height compared to the previous time. Directly to the west of the eye, a decrease is exhibited in the surface to 5 km in positive PV in this MO area when compared to the previous time. Overall, the west side has stretched and slightly weakened while the eastern side has slightly strengthened. This decrease in the western positive PV here is indicative of the weakening eyewall region as it approaches the mountain and enters the "transition" zone prior to landfall.

Figure 5.4 displays the corresponding $\theta$ and AV fields. On the eastern side of the TC, the AV has significantly increased from the previous time below 7 km. The $\theta$ fields have remained nearly the same, although the vertical potential temperature gradient ($\partial\theta/\partial z$) appears to have

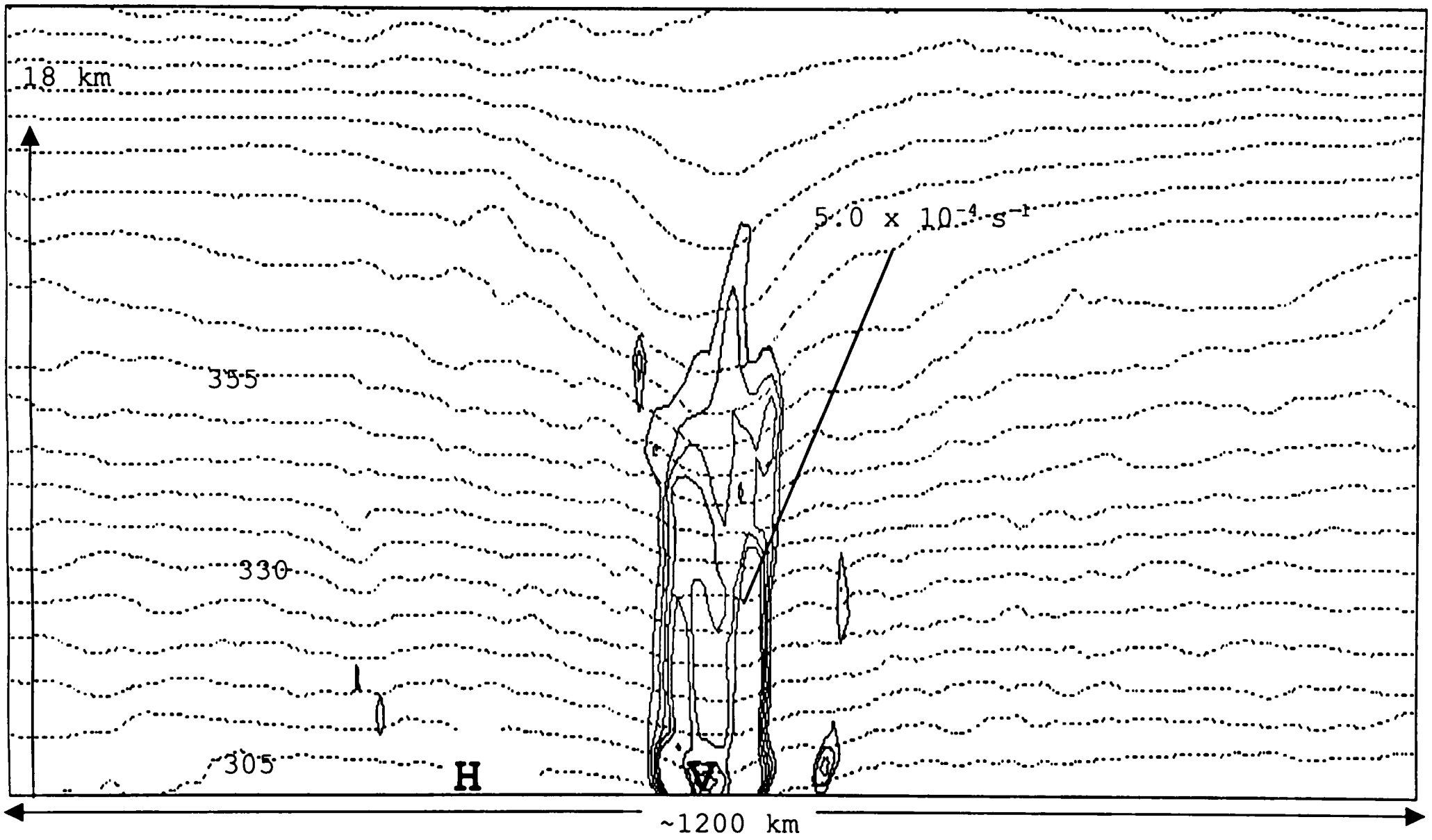


Figure 5.4. Vertical east-west cross section of positive absolute vorticity and potential temperature just before landfall, 0400 UTC 31 July 1996. AV contour interval is 2.5 x $10^{-5}$ $s^{-1}$ and potential temperature is 5 K. The eye is identified with a 'V' and the terrain with an 'H'.

increased in the mid-levels, most notably at the tops of the more enhanced east/west AV regions.

### 5.1.3 Over Land

Figure 5.5 displays Herb over land, at 1000 UTC 31 July. As might be expected at this stage, the symmetrical positive PV anomaly seen previously has broken down, although not to the extent of the vertical motion fields as seen in the past chapter. No PV values greater than 5 PVU exist below 3.5 km within the convective eyewall region, as evidenced by the lack of contours in that region. In fact, the absence of positive PV just above the CMR in the typhoon vicinity correlates well with Figure 4.7, where a strong area of sinking air is observed along the eastern slopes. Two distinct areas of positive PV associated with the structure of the TC that are now elevated remain. These are confined between altitudes of 3.5 km and 7 km. Overall, the anomaly has contracted both vertically and horizontally compared to the earlier cases, while still exhibiting two distinct east-west PV regions. The magnitudes of both have decreased only slightly since the last time frame. The western edge has reduced to 15 PVU at its highest value, a decrease of only 2.5 PVU. On the

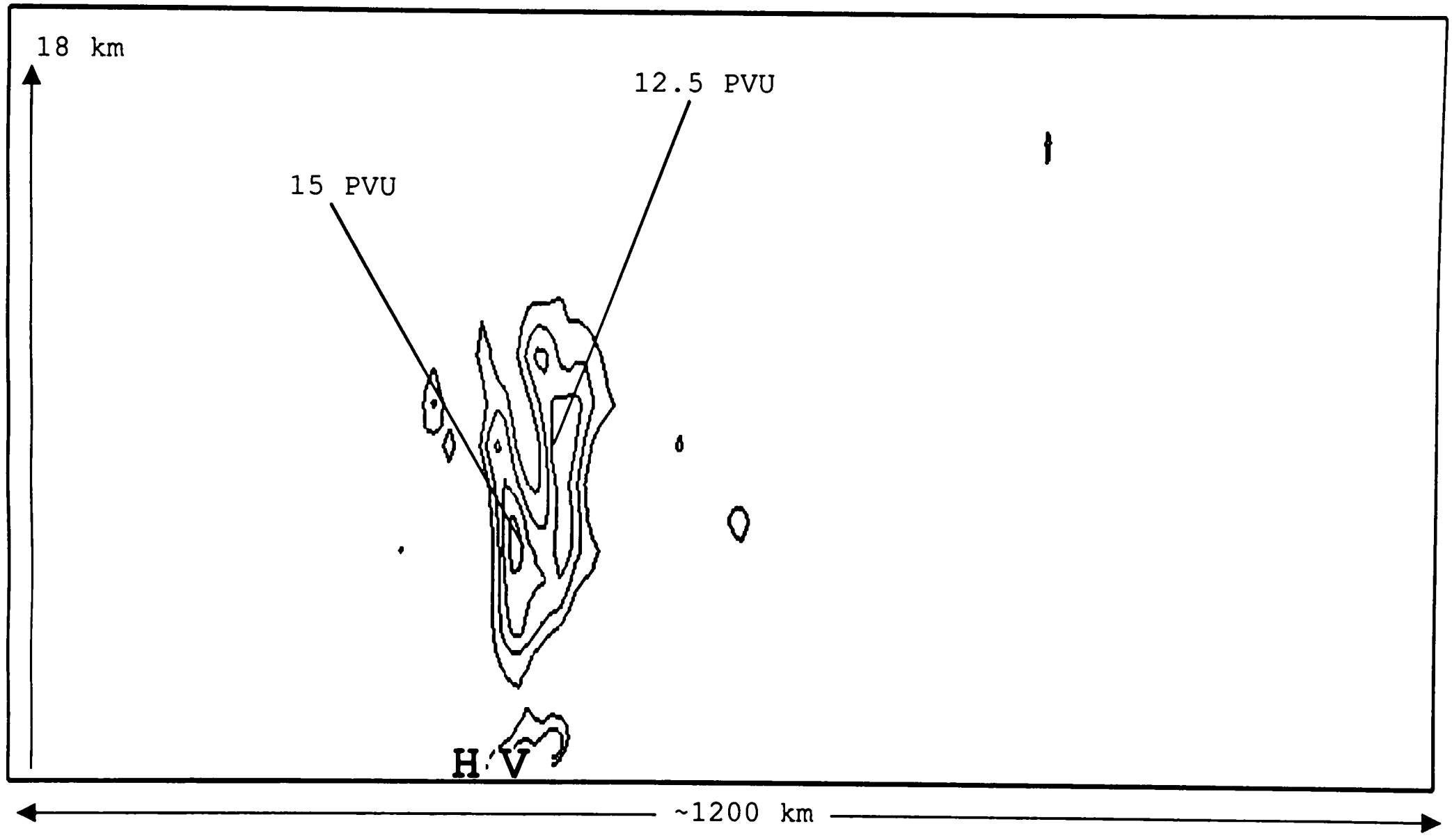


Figure 5.5. Same as in Figure 5.1 but for 1000 UTC 31 July 1996.

eastern side, a drop of 7.5 PVU is observed. At least in PV terms of thought, this signifies that the majority of the weakening of the PV anomaly occurred before landfall, most likely within the "transition" zone.

Figure 5.6 represents the AV and θ fields associated with Herb at this time. Little changes are observed with the θ field. Consequently, the AV field has weakened over the terrain as well, although its symmetrical nature remained intact. Rather than the two distinct regions of higher values as in the W and PV fields, one centrally located maximum is seen.

## 5.2 Lee Potential Vorticity Generation

### 5.2.1 Horizontal Cross Section Analysis

A second method of "PV thinking" involves the generation and distribution of positive PV that occurs within the TC environment. Specifically, the generation of positive PV on the lee side of the terrain feature and its subsequent advection into the TC is of greatest interest. Future insight into the storm's track may be deduced from this information. Figure 5.7 displays a horizontal plot of wind vectors (note the 60 km spacing) and positive PV on a constant height surface of 1 km at 0800 UTC 30 July. This

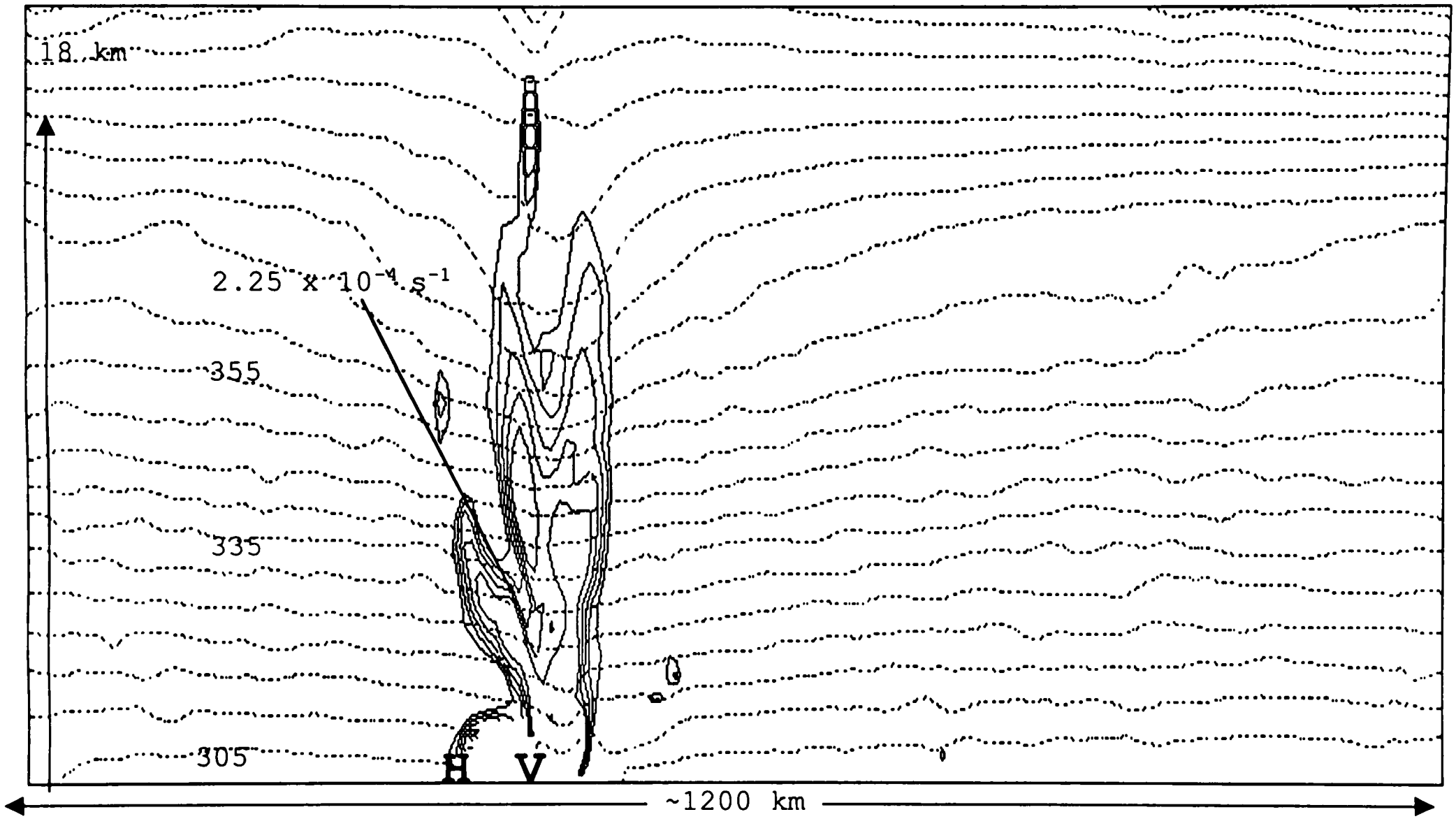


Figure 5.6. Vertical east-west cross section of positive absolute vorticity and potential temperature over land, 1000 UTC 31 July 1996. AV contour interval is 2.5 x $10^{-5}$ $s^{-1}$ and potential temperature is 5 K. The eye is identified with a 'V' and the terrain with an 'H'.

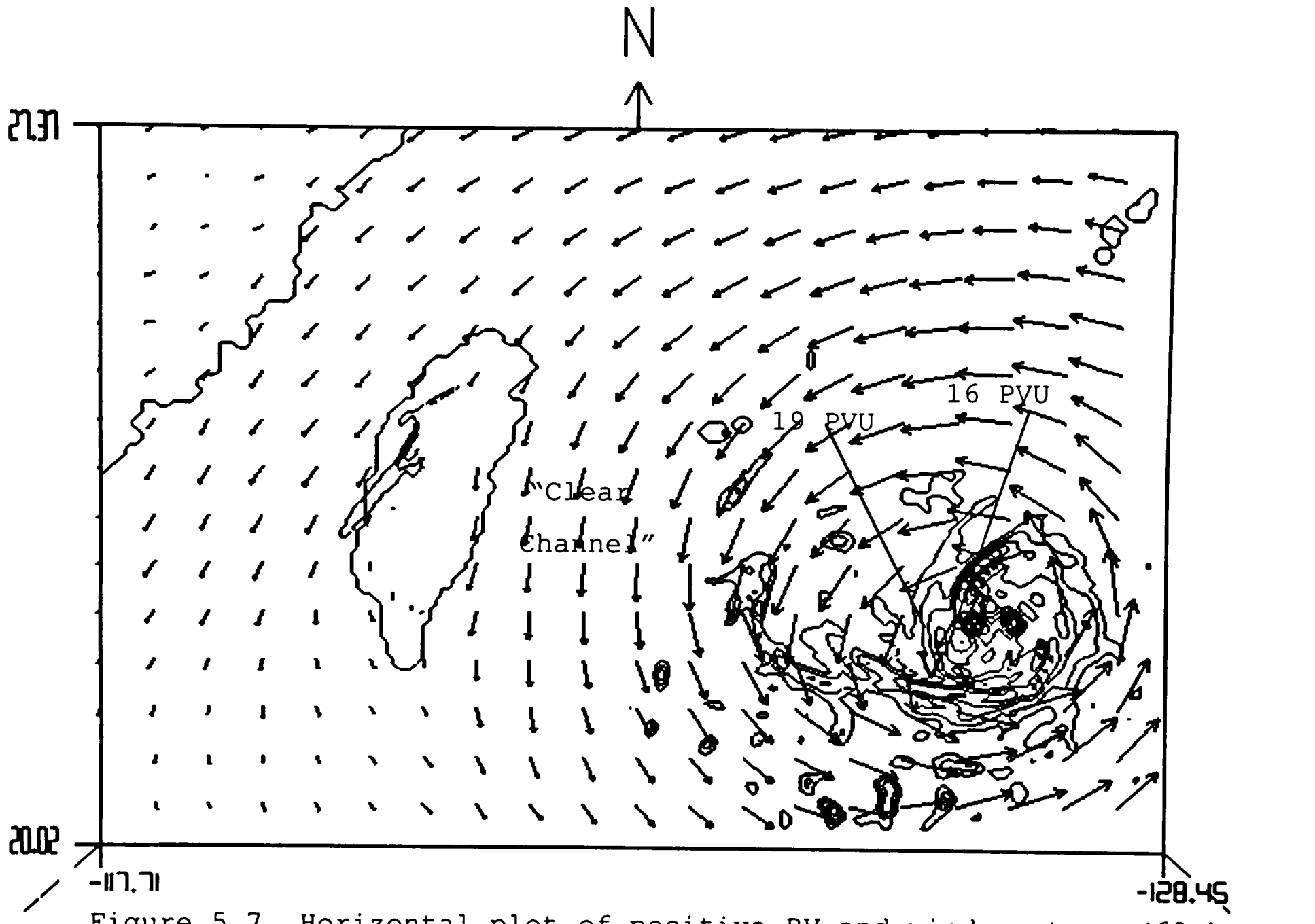


Figure 5.7. Horizontal plot of positive PV and wind vectors (60 km resolution) at 1 km well before landfall, 0800 UTC 30 July 1996. Contour interval is 2 PVU from 2 to 10 PVUs. The eye is identified with a 'V'.

scenario occurs well before the typhoon makes landfall, approximately 725 km beforehand. The contour interval has been reduced to 2 PVU for the horizontal images and the best estimate of the center of circulation is identified with a 'V'. From this point of view and as compared to the previous three figures, it is quite clear that the TC is indeed a three-dimensional positive PV anomaly.

The region in and around the eye contains the greatest PV values, with weaker values found radially outward. Just to the north of the center of circulation there are two maximum positive PV regions identified on Figure 5.7 and labeled with values of 16 and 19 PVU, respectively. These maximum regions coincide very well with the upward motion (MO) regions shown in Figure 4.6. These increased PV "spots" are found to exist vertically from 1 km to the 5 km level, with average values around 16 PVU. They also correlate quite well with regions of upward motion and cloud water (not shown) as in Figure 4.6. This is indicative of the existence and coincidence of positive PV regions within the convective updrafts.

There is also a northwest-east oriented "trail" of relatively higher PV air located on the southwestern side of the TC. The air parcels at this height are advected

into the TC environment and appear to be the result of PV redistribution within the typhoon. Over the CMR, there are a few small areas of positive PV found along the northwestern and central portions of the mountain. At this time, none of the very small PV associated with the terrain appears to be advected into the storm environment. The lack of any positive PV found in the 400 to 500 km "clear channel" region downstream of the CMR and the TC center supports this conjecture.

At 3 km for the same time, Figure 5.8 displays another cross section of positive PV and wind vectors. This layer resides within the higher PV air, as evidenced by the two maximum regions just to the north of the eye. In comparison to the 1 km level, maximum positive PV values have increased slightly by about 2.5 PVU in each case. These two maximum regions are positioned parallel to their lower counterparts (i.e., there is no tilting of the anomaly with height between these levels). This lack of tilting is to be expected as westward tilting of the anomaly did not begin until the 5 km height as shown previously.

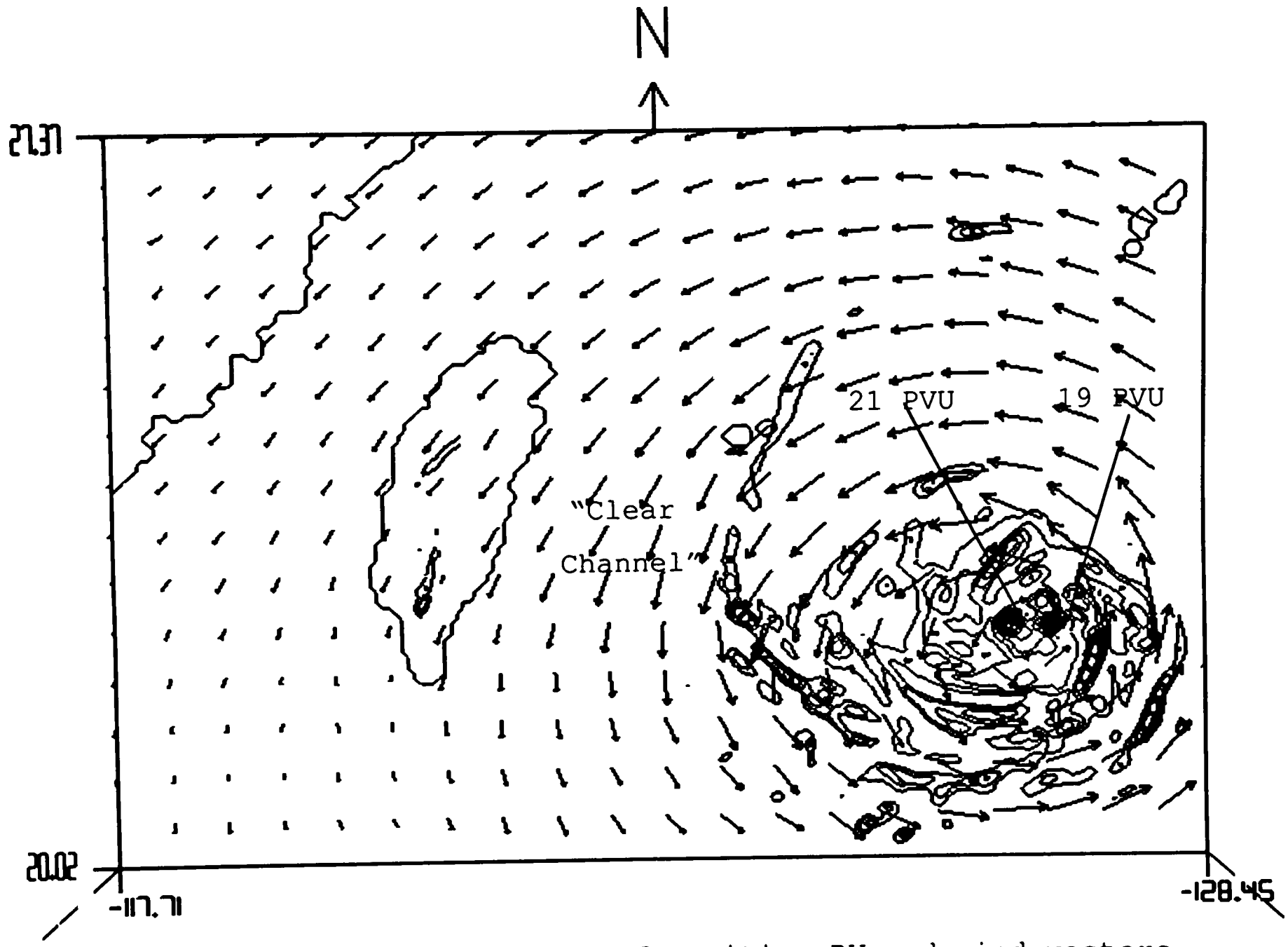


Figure 5.8. Horizontal plot of positive PV and wind vectors (60 km resolution) at 3 km well before landfall, 0800 UTC 30 July 1996. Contour interval is 2 PVU from 2 to 10 PVUs. The eye is identified with a 'V'.

The "trail" of positive PV seen at the 1 km level can still be identified, though it is now oriented in a more northwesterly-southeasterly direction and originates from more northerly regions of the TC environment. There is a slight increase in the magnitude of the "trail" PV values, from about 2-4 PVU at 1 km to 7-9 PVU (not labeled) at this level. Again, this higher PV air appears to be advected into the TC environment at this level as well.

Over the CMR, there is relatively little PV found. A small area is noted in the south central regions with a bit along the northeastern slopes. As seen at the 1 km level, none appears to be moving into the TC environment, exemplified by the lack of any PV in the northwest flow area (clear channel) located between the CMR and Herb. An argument can be made, however, that the extreme western flow associated with Herb may be responsible for this small generation. Note the lack of any positive PV on the lee (western) side of the CMR at this level as seen below. Figure 5.9 displays an "intermediate" time, 2000 UTC 30 July when the TC eye is approximately 500 km offshore. It displays the 3 km constant height surface. This special horizontal cross section depicts the first significant positive PV generation observed over the CMR. Note that

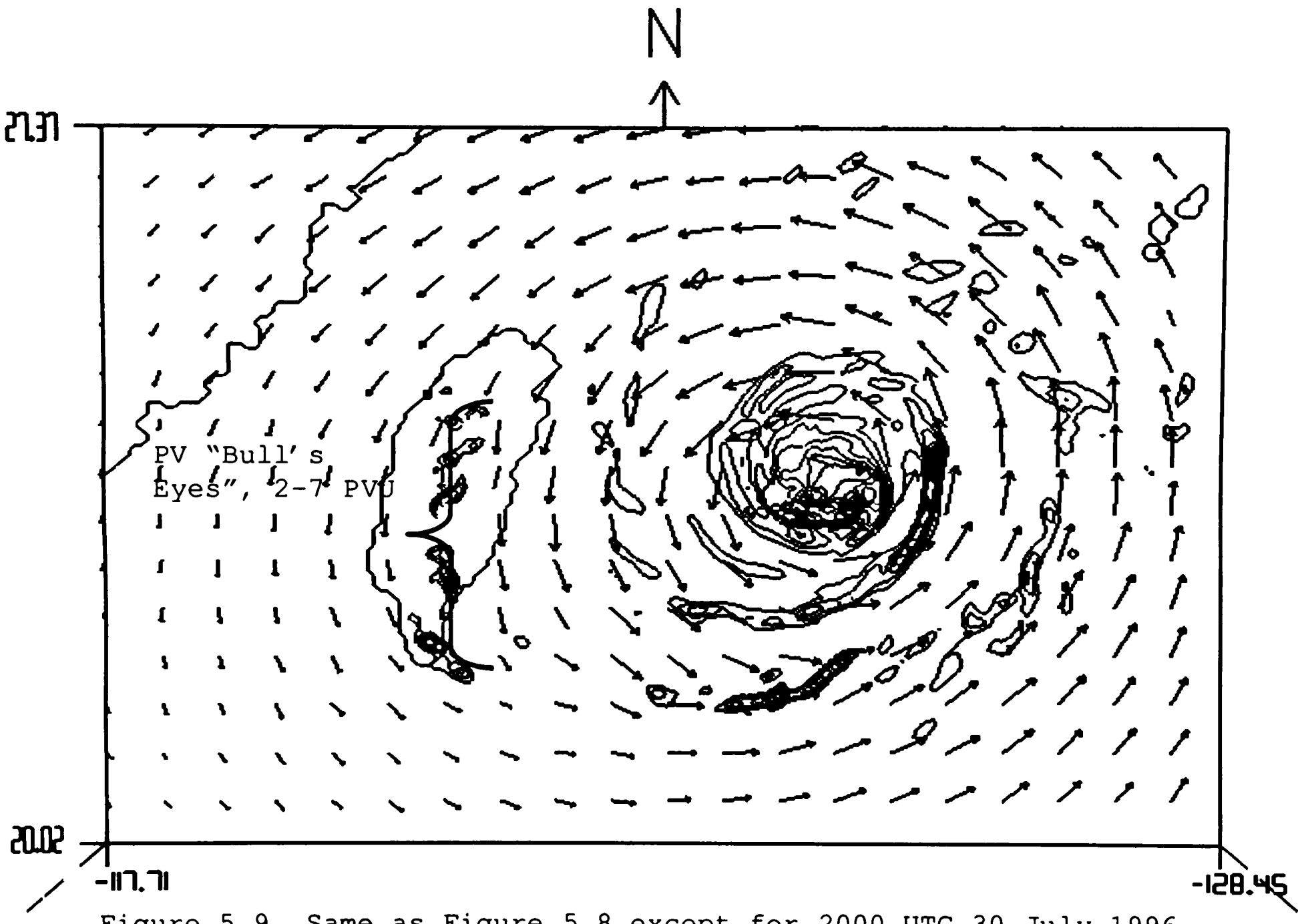


Figure 5.9. Same as Figure 5.8 except for 2000 UTC 30 July 1996.

this time is about six hours prior to the "transition zone," as referenced earlier. There are several small, circular regions of higher concentrated PV air extending linearly north-south parallel to major axis of the CMR. These enhanced regions are also oriented exactly parallel to the mean flow as compared to the wind vectors at this level. A channel 150 to 200 km wide extends between the CMR and the typhoon, which lacks any significant positive PV, indicating as before the "bull's-eyes" are a product of the flow interaction with the terrain and not simply redistribution within the typhoon itself. From equation (1.4) and as shown later, an increase in both terms on the right-hand side likely contributes to this generation. Specifically, an increase in the vertical potential temperature gradient, $(\partial\theta/\partial z)$ as the flow interacts with the terrain was likely the greatest contributor. Due to the data set obtained it was impossible to perform a budget analysis on equation 1.4 to verify which terms contributed most to this positive PV generation.

The strongest positive PV bull's-eyes (6-8 PVU) nearest the TC were found to correlate well with upward motion and cloud water content (not shown) values of greater than 1.5 m $s^{-1}$. The weaker bull's-eyes did not lie

in regions of any significant rising motion. Again, this indicates the highest positive PV regions were associated with convective updrafts.

Just before landfall, an enhancement of the positive PV bull's-eyes is observed based on Figures 5.10 and 5.11. Again, at this time (0400 UTC 31 July) the typhoon is within the "transition" period, where the symmetries and "conceptual" model comparisons began to break down. At this stage, however, the entire positive PV anomaly that encompasses the eyewall has not lost any of its horizontal symmetry. The MO regions coinciding with the positive PV anomaly identified in the last two figures remain and have deepened slightly as well as shifted south.

The bull's eyes features are more pronounced at the 3 km level (Figure 5.11) at this time. At 1 km (Figure 5.10), a significant region of positive PV spans the entire lee of the CMR, from northwest to southeast. Again, the generation appears parallel to the typhoon-incident northwest flow. Offshore from the southeast coast of Taiwan, a few weaker (less than 5 PVU) positive PV bull's-eyes are seen. At 3 km, the small positive PV anomalies are much better defined, stronger in magnitude (4-5 PVU)

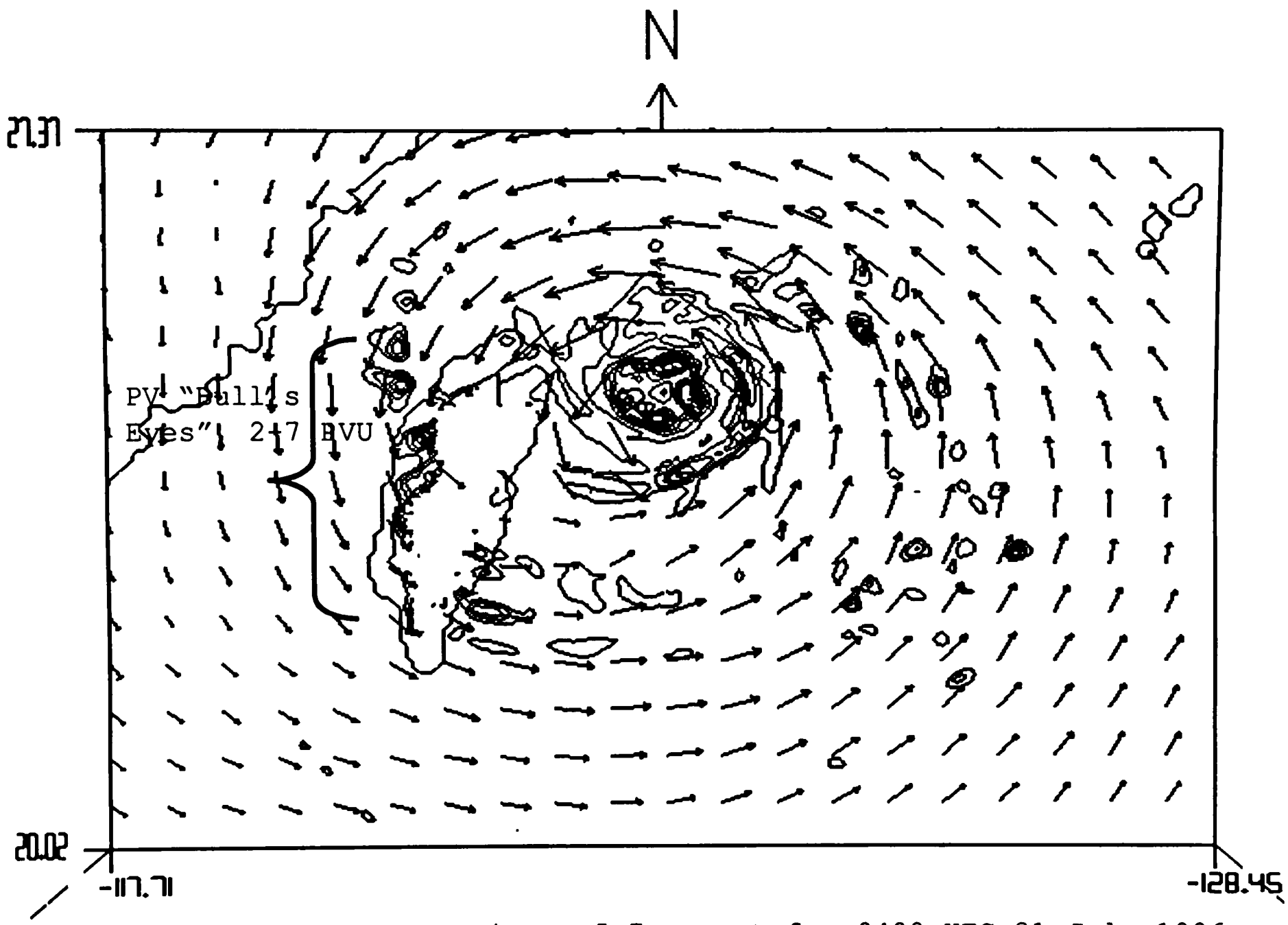


Figure 5.10. Same as Figure 5.7 except for 0400 UTC 31 July 1996.

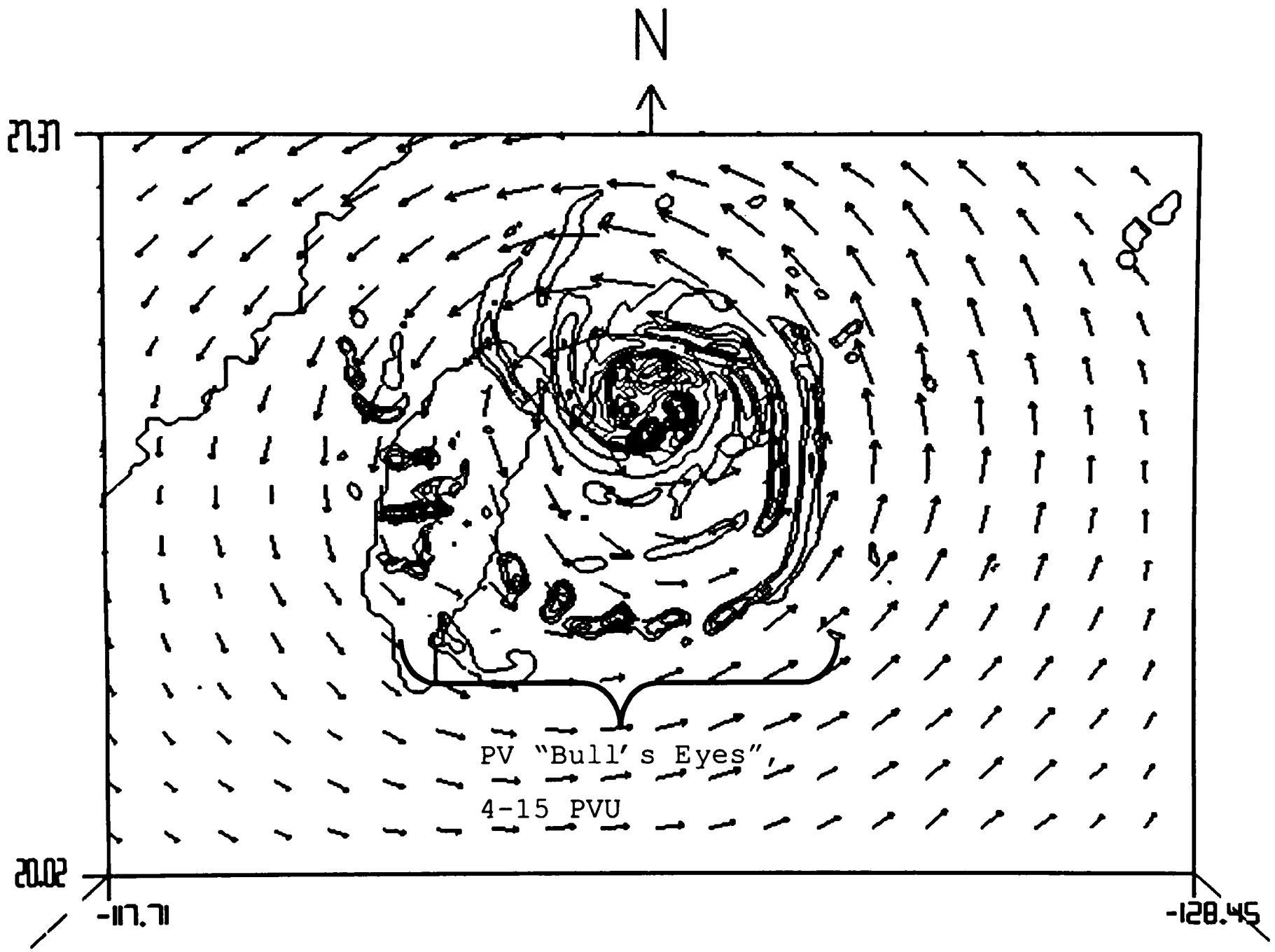


Figure 5.11. Same as Figure 5.8 except for 0400 UTC 31 July 1996.

and are aligned in a "train" parallel to the mean flow, indicative of their advection into the TC environment. It appears from these figures that any positive PV that is generated on the lee side of the CMR is advected directly into the inner-core/eyewall region of the TC environment.

As Supertyphoon Herb traverses Taiwan, an overall decrease in positive PV is noted (as displayed by the cross sections), along with the absence of any symmetrical structure that had previously existed. Figure 5.12 shows Herb over the CMR at 1 km. The highest positive PV air surrounds the perimeter of the CMR, with the TC itself not identifiable by a positive PV anomaly as before. At this low level, the CMR blocks any flow thus inhibiting any positive PV that may have already existed. PV bull's-eyes are still evident in the northeast quadrant, likely remaining from prior lee side generation and continuing to advect into the TC.

At 3 km (Figure 5.13), a more familiar structure is seen. The anomaly is more identifiable but concentrated to the northeast quadrant of the typhoon. Mt. A-Li (refer to Figure 1.1), one of the tallest peaks of the CMR as well as several other higher areas in the Hsinchu region is located to the southwest of this anomaly. Again, blocking and

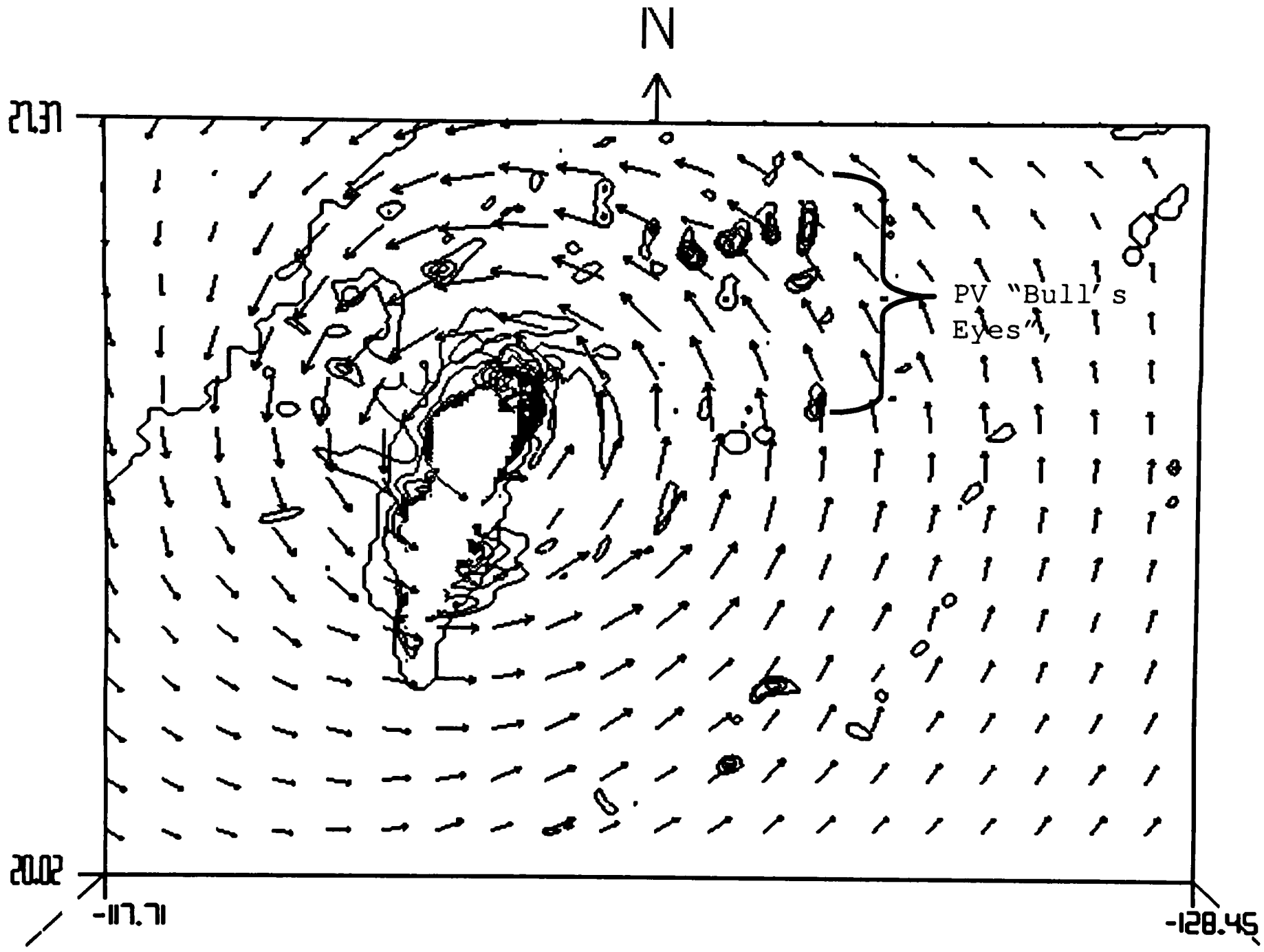


Figure 5.12. Same as Figure 5.7 except for 1000 UTC 31 July 1996.

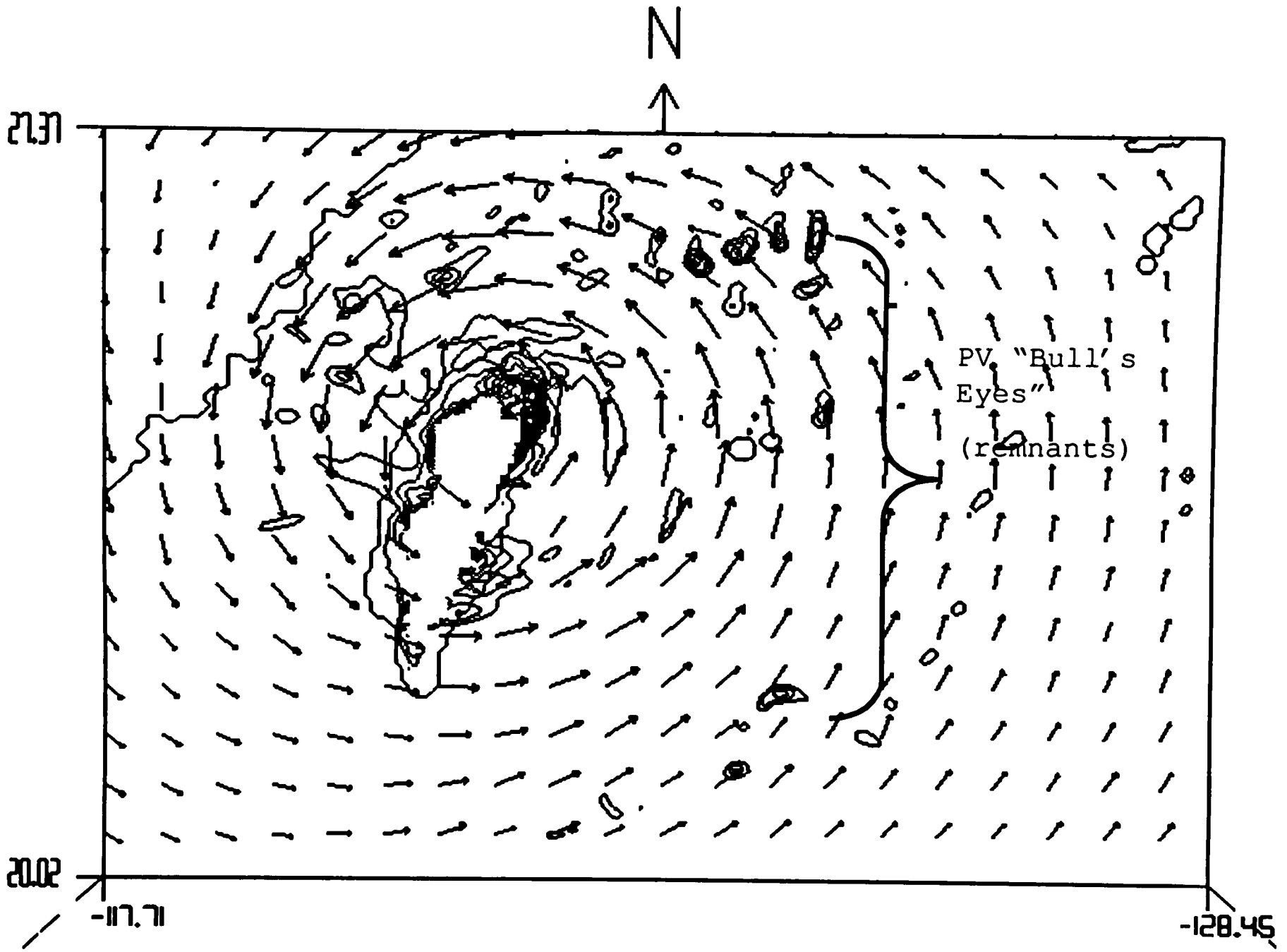


Figure 5.13. Same as Figure 5.8 except for 1000 UTC 31 July 1996.

channeling is seen with the high concentration of positive PV to the northeast, as the highest values remain to the east of the typhoon's center of circulation. Overall, the symmetrical positive PV anomaly over land no longer exists, much the same as with the vertical motion fields seen in the last chapter.

A few bull's-eyes remnants are found in the northeast flow associated with the TC at both levels. Along the southern half of Taiwan, limited positive PV generation is occurring, with weaker bull's-eye areas noted in the southeast quadrant of the typhoon. Values for these weaker bull's-eyes are less than 5 PVU on average. With a weaker flow at both levels associated with the TC as well as a more parallel flow component along the northern half of the CMR, a decrease in the generation of positive PV is reasonable.

### 5.2.2 Probing the Positive PV Generation

In order to gain further insight into and to quantify the positive PV generation that may occur on the lee side of the CMR, three "probes" are placed at different levels and locations. Figure 5.14 displays the three points, labeled "north", "south" and "east," where the probe

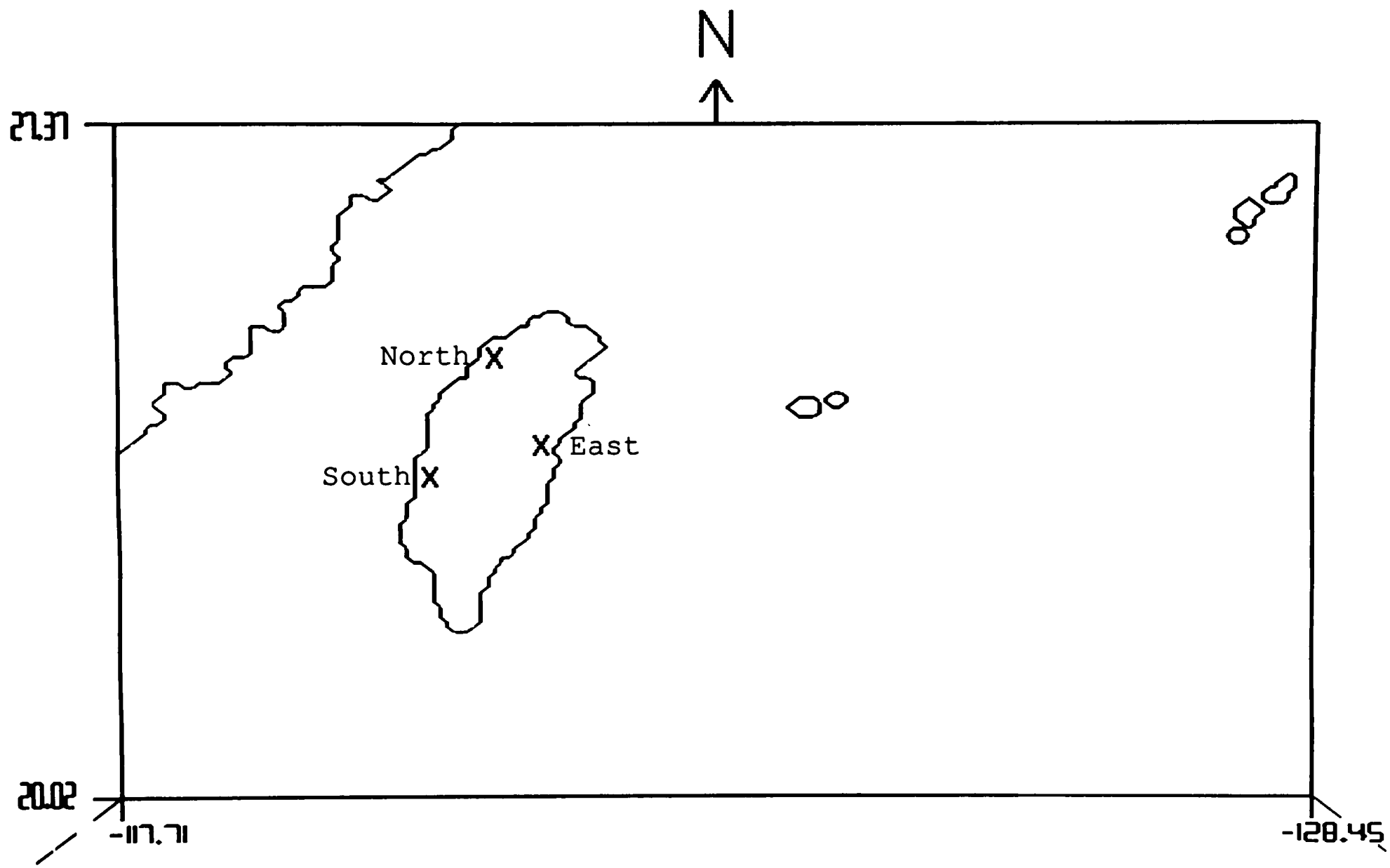


Figure 5.14. Three PV probe locations.

"measures" the PV, absolute vorticity (AV), vertical change in potential temperature ($\partial$(THE)/$\partial$z) and upward motion (W) at different times. Probes are placed on two vertical levels at each location, 1.0 and 3.0 km to match up with the horizontal plots previously examined. In terms of equation 1.4, the horizontal variation in potential temperature is ignored as it is small compared to that of the vertical away from the center of the TC.

An average of five individual "measurements" for each parameter at each level and location was then calculated. The objective was to eliminate any erroneous or outlying values within the data. The four closest points as determined by latitude and longitude around a center point was used in obtaining values for averaging. After the averaging, a time series of all variables each location and level was produced. Times were chosen represent the typhoon approaching the terrain feature and to include the "transition zone" between 0400 and 0600 UTC 31 July. Prior to 0000 UTC, no significant changes in any of the variables were observed and thus omitted from the graphs. The plots for PV, absolute vorticity, vertical change in potential temperature and upward motion are shown in Figures 5.15 through 5.20.

There are a few caveats to be aware of in examining the graphs. While the abscissa remains fixed throughout the series, the ordinate values change somewhat between charts. Although averaging removed many of the extraneous values, some remained. In order to plot all four parameters (which have different orders of magnitude) on the same set of axis, some manipulation of the raw values was required. For example, PV is multiplied by 10 PVU (i.e., 2 PVU is now 20 PVU), absolute vorticity is an order of magnitude smaller (x $10^{-5}$) vertical potential temperature gradient $\partial$(THE)/$\partial$z is larger (x 10 K/km), and W is in cm $s^{-1}$. As the interest here is in the change of each parameter with time, a set ordinate is not crucial.

In comparing all six graphs, it is immediately seen that a good correlation exists between PV, AV and W in all six cases. If one drew a best-fit line, a similar change with time is noted between all three parameters regardless of location or height. Also noteworthy is in all cases, the 3 km plots displayed higher values for all parameters than at the lower height.

### 5.2.3 Graphical Analysis of PV Generation

Figures 5.15 and 5.16 represent the northern probe at 1 and 3 km, respectively. Each plot tells a slightly different story. After 0400 UTC in each plot, all parameters increase through 1200 UTC. At 1 km, there was a sharp decrease from 0000 UTC to 0400 UTC followed by a rapid increase. As the location of the probe was quite close to the area that the TC made landfall, a sharp increase at both levels prior to and during landfall is to be expected. Thus, the rapid increase seen after 0400 UTC at both levels was determined to be a result of the probe's close proximity to the typhoon itself and not representative of any PV generation. Recall that from Figures 5.9 through 5.13, few PV bull's-eyes were observed in the northern half of the island. The greatest concentrations of positive PV bull's-eyes were found mainly in the southern regions.

Figures 5.17 and 5.18 show the southern probe at both levels. Based on the horizontal plots, this was the "favored" location for the generation of positive PV. Beginning at the "transition" time of 0400 UTC, at 1 km an increase in all parameters is noted until 0800 UTC, followed by a slight decrease and then another increase

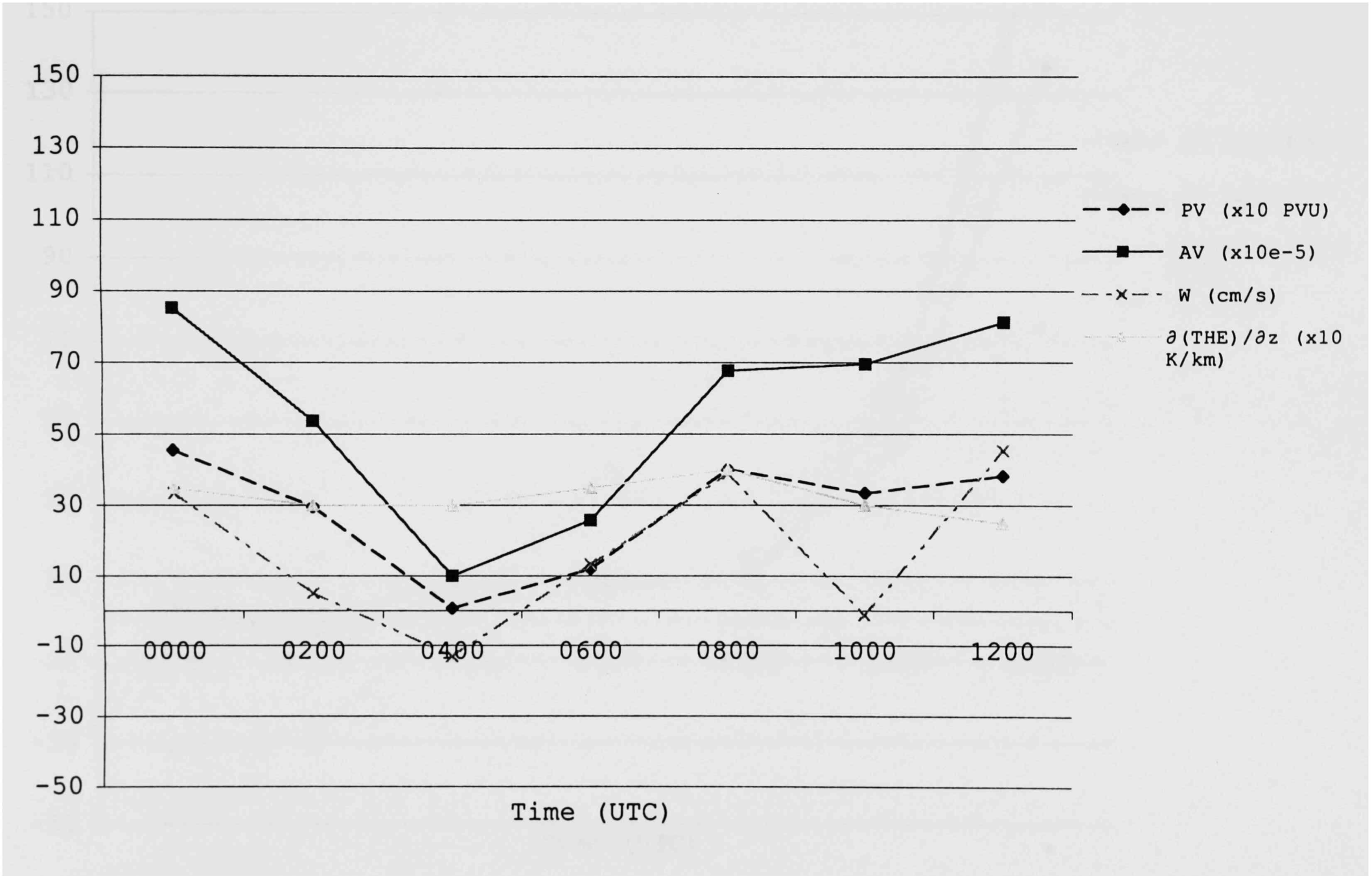


Figure 5.15. North Probe at 1 km.

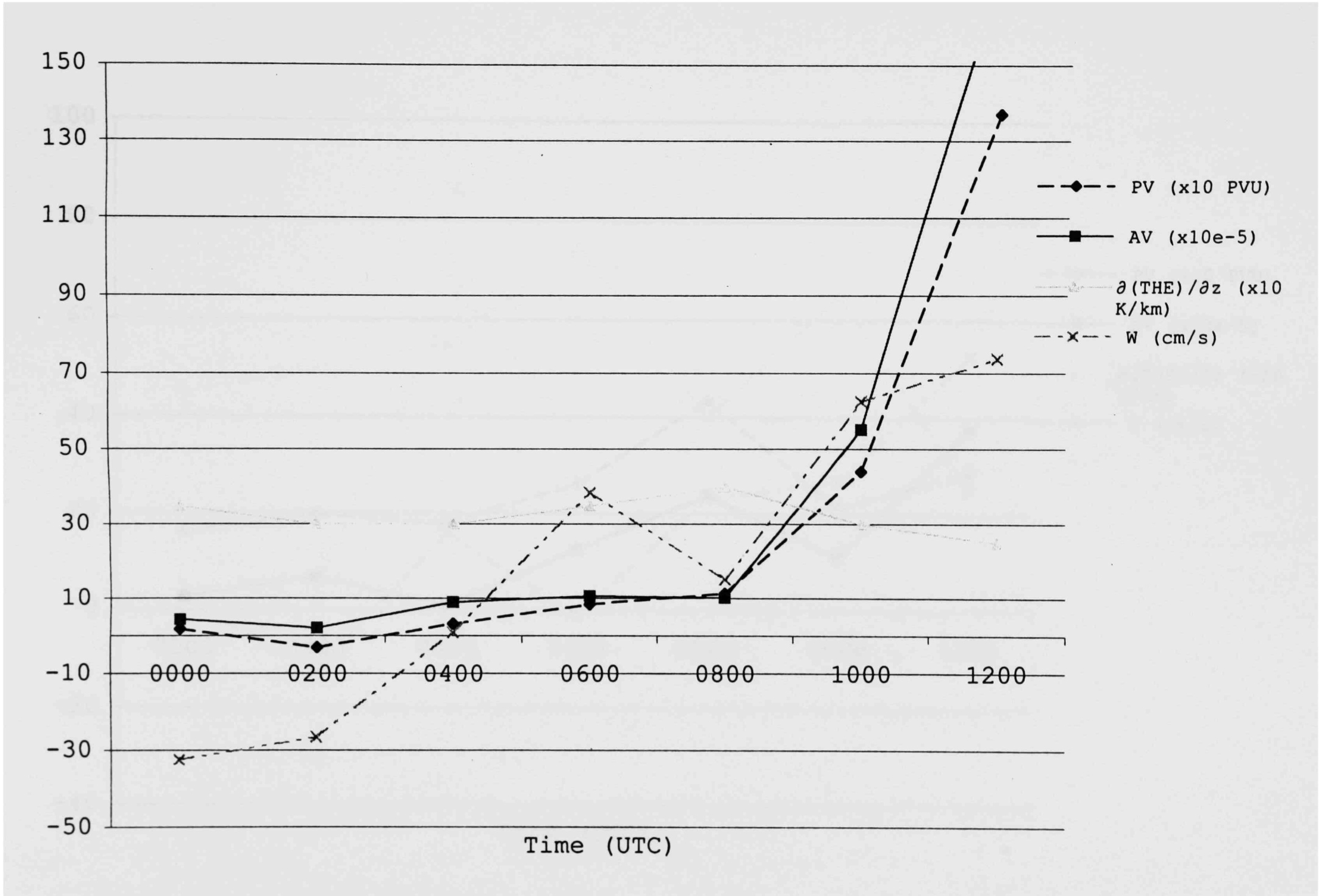


Figure 5.16. North Probe at 3 km.

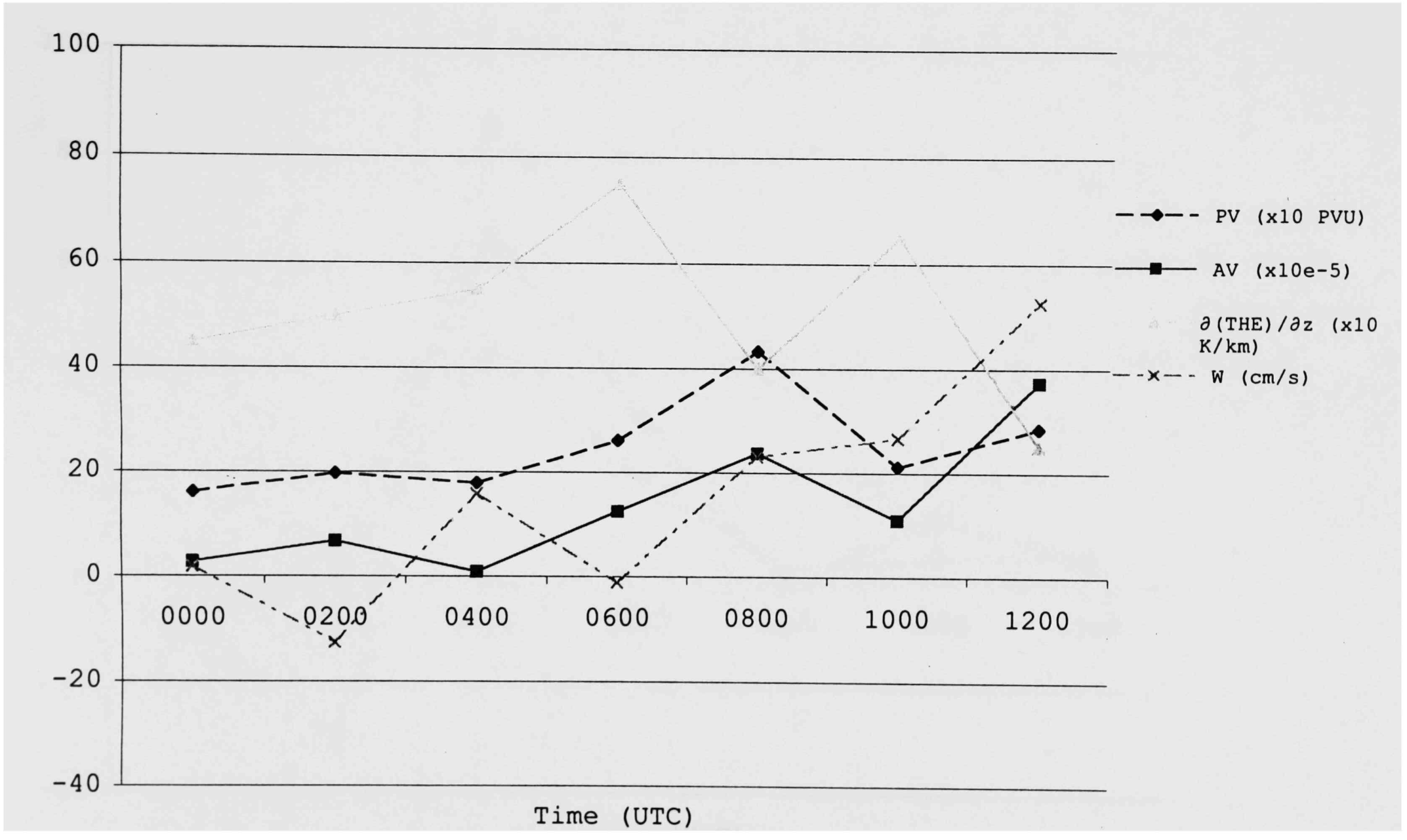




Figure 5.17. South Probe at 1 km.

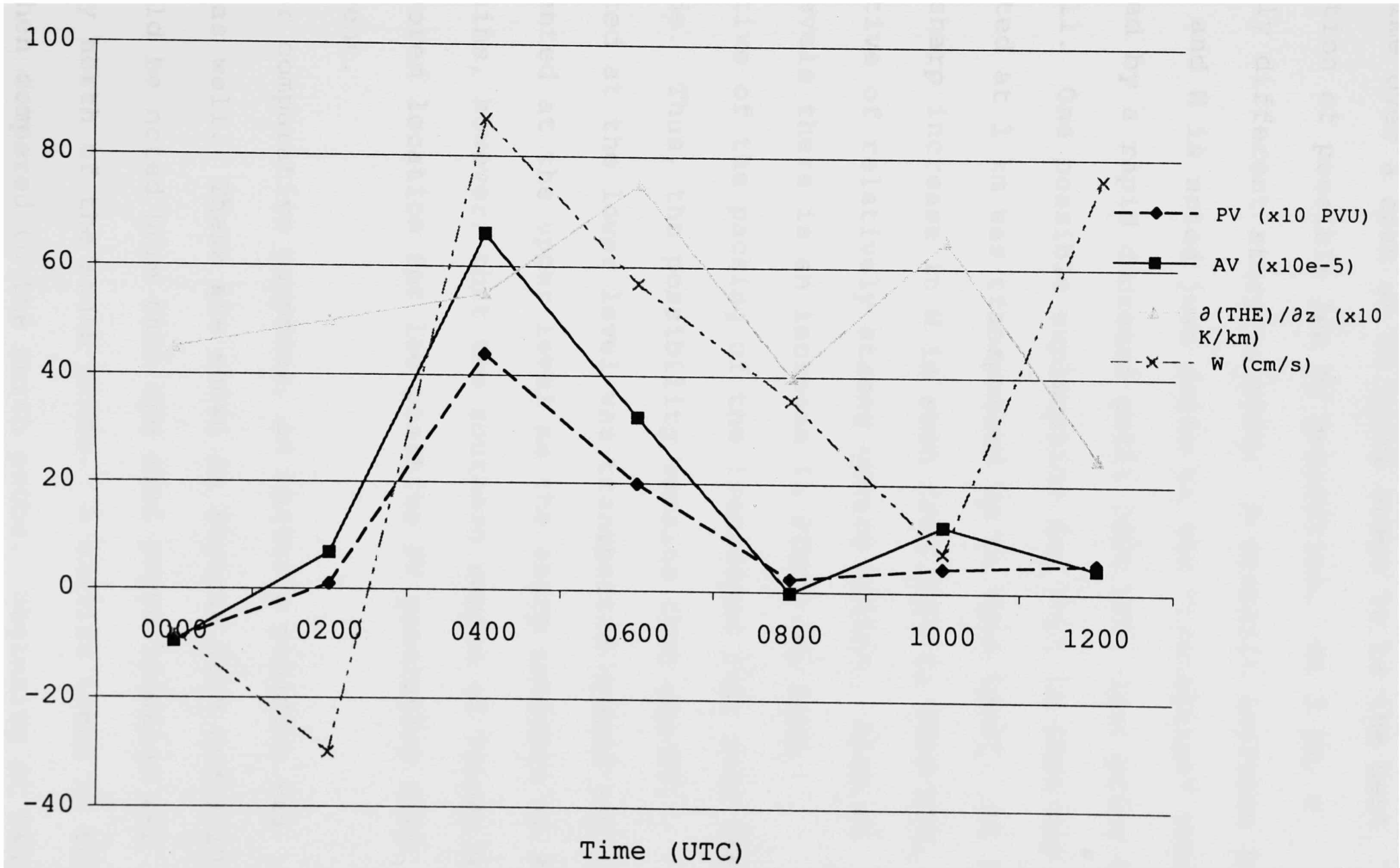


Figure 5.18. South Probe at 3 km.

until 1200 UTC. This continual increasing and decreasing with time over a span of 10 hours seems to be the best indication of possible lee PV generation. At 3 km, a slightly different story is told. A dramatic increase in PV, AV and W is noted just prior to the "transition" zone, followed by a rapid decrease until 0800 UTC, just prior to landfall. One possible explanation for this is that any PV generated at 1 km was transported up to this level. At 1 km, a sharp increase in W is seen from 0200 to 0400 UTC, indicative of relatively strong upward motion. Also at both levels there is an increase in $\partial(\mathrm{THE})/\partial z$ term, indicative of the packing of the isentropes just over the lee side. Thus, the possibility remains that any PV generated at the lower level was transported upward and is represented at the upper level as the sharp increase in PV. It remains, however, that the southern region of Taiwan was the favored location for lee positive PV generation with this event.

For comparative purposes, an easterly position was chosen as well. These are shown in Figures 5.19 and 5.20. It should be noted here that the east probe location was slightly north of the south probe. A similar trend is thus noted when compared to the north probe. Beginning at 0400

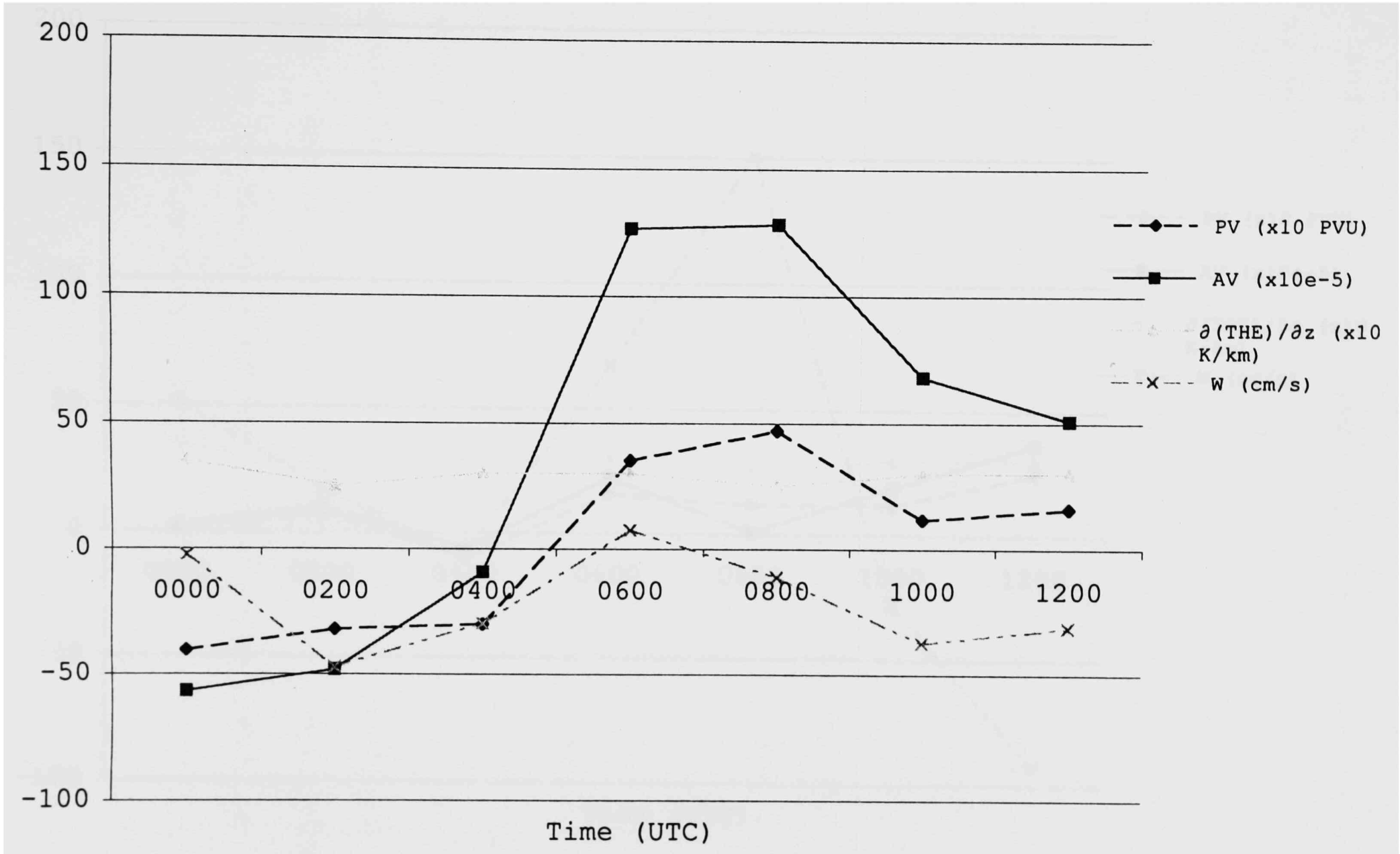


Figure 5.19. East Probe at 1 km.

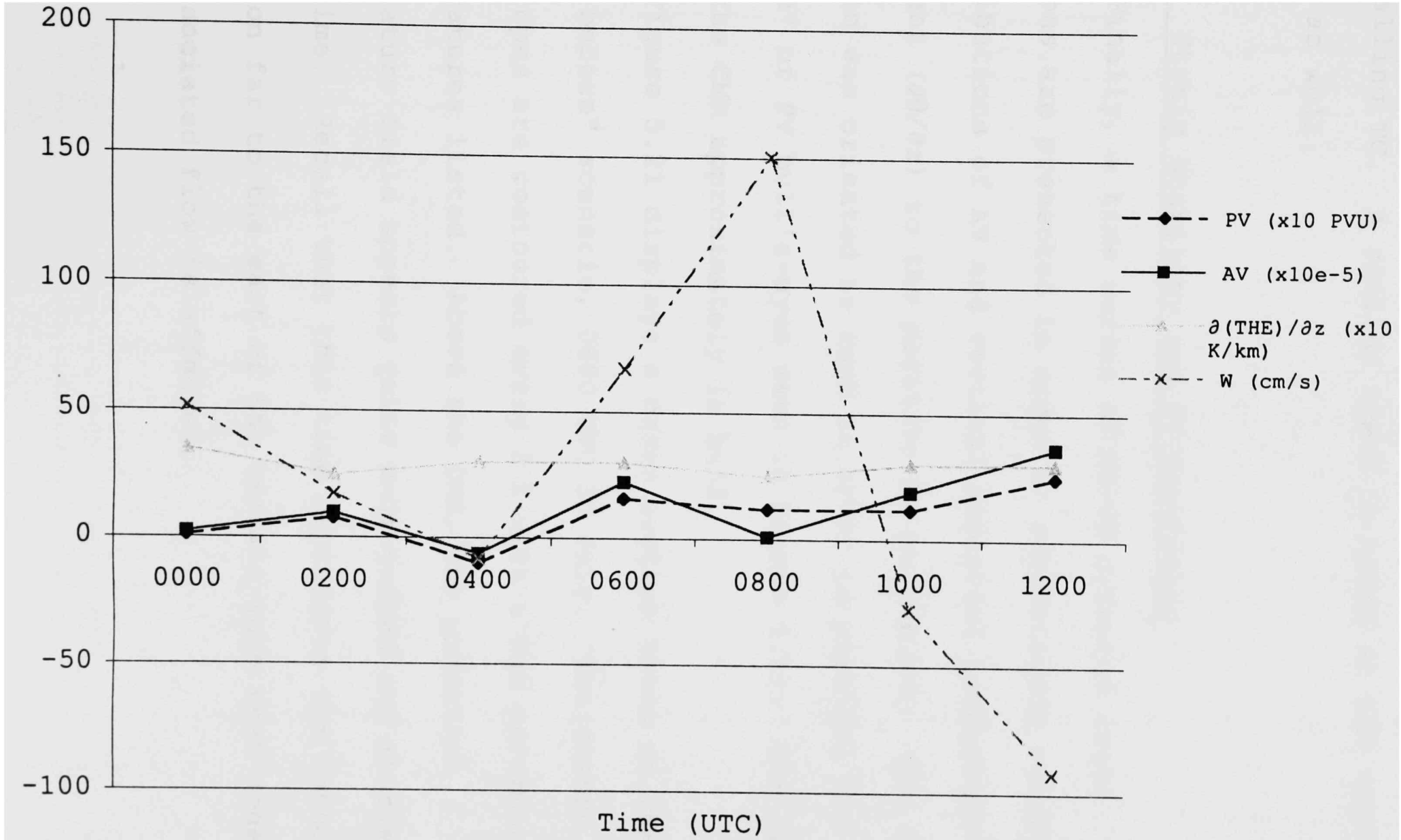


Figure 5.20. East Probe at 3 km.

UTC, a drastic increase is seen at 1 km, perhaps due to the close proximity of the probe to the southern edge of the landfalling TC. A similar trend is noted at the upper level as well.

### 5.2.4 Static Stability and PV Generation

Finally, a time series of NW-SE oriented cross sections are presented in order to subjectively assess the contributions of AV and vertical potential temperature gradient ($\partial\theta/\partial z$) to the positive PV generation. The cross section was oriented as such in order to parallel the "train" of PV bull's-eyes seen in Figure 5.11. The slice cuts the CMR approximately in half.

Figure 5.21 displays a cross section taken at the "well before" scenario, 0800 UTC 30 July. The dashed isentropes are contoured every 2 K with a few reference temperatures listed. Above the CMR, the potential temperature field appears quite undisturbed and stable at this time. Recall that this time represents the typhoon's position far to the east of the terrain such that none of its associated flow is affected.

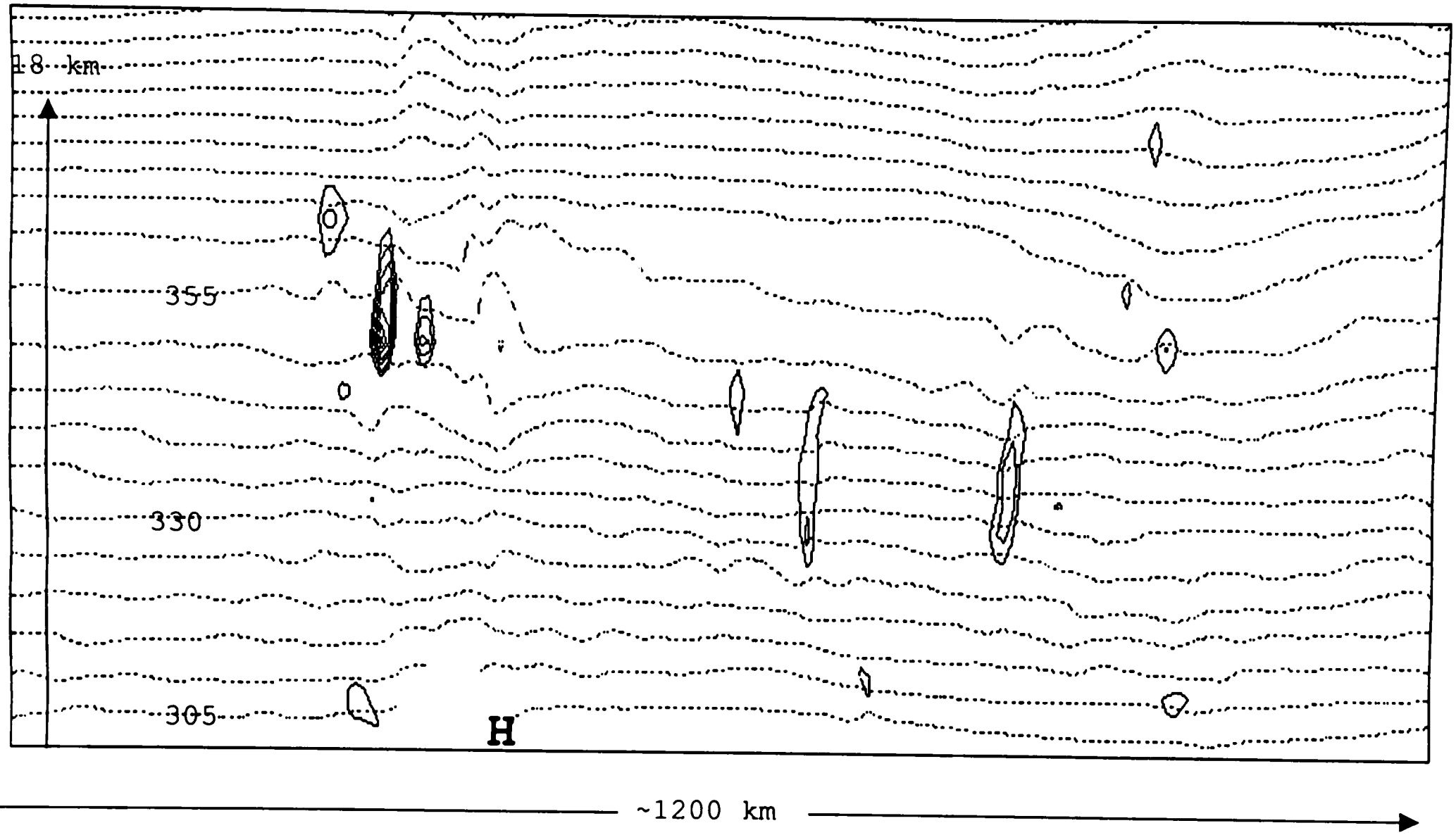


Figure 5.21. Vertical NW-SE cross section of positive absolute vorticity and potential temperature well before landfall, 0800 UTC 30 July 1996. AV contour interval is 2.5 x $10^{-5}$ $s^{-1}$ and potential temperature is 5 K. The terrain is identified with an 'H'.

Jumping ahead to 2200 UTC 31 July as drawn in Figure 5.22, the isentropes become much more packed just above and to the west of the CMR as compared to the previous time. By inspection, an increase in 8-10 K is observed through a comparable pressure slab. A small region of AV is also seen on the west side of the terrain. The isentropes continue to pack more tightly together in this region every two hours as evidenced in Figures 5.23 until 5.27. This is indicative of an increase in the $(\partial\theta/\partial z)$ term of Equation 1.4, which ultimately results in a PV increase assuming the AV remains relatively constant. There is also an increase in AV displayed in Figures 5.23 and 5.24, which represent 0000 and 0200 UTC 31 July. As the "transition zone" of 0400 until 0600 UTC is entered, the AV increase ceases though the isentropes continue to pack on the west and over the CMR. From these particular cross sections, it would appear subjectively that the $(\nabla\theta)$ term in equation 1.4 is the biggest contributor. Within that term, $(\partial\theta/\partial z)$ contributes most to the overall positive PV generation. By 1000 UTC, when PV generation appeared to cease over the terrain, the isentropes become less tightly packed, this reducing the $(\nabla\theta)$ term. This is to be expected assuming

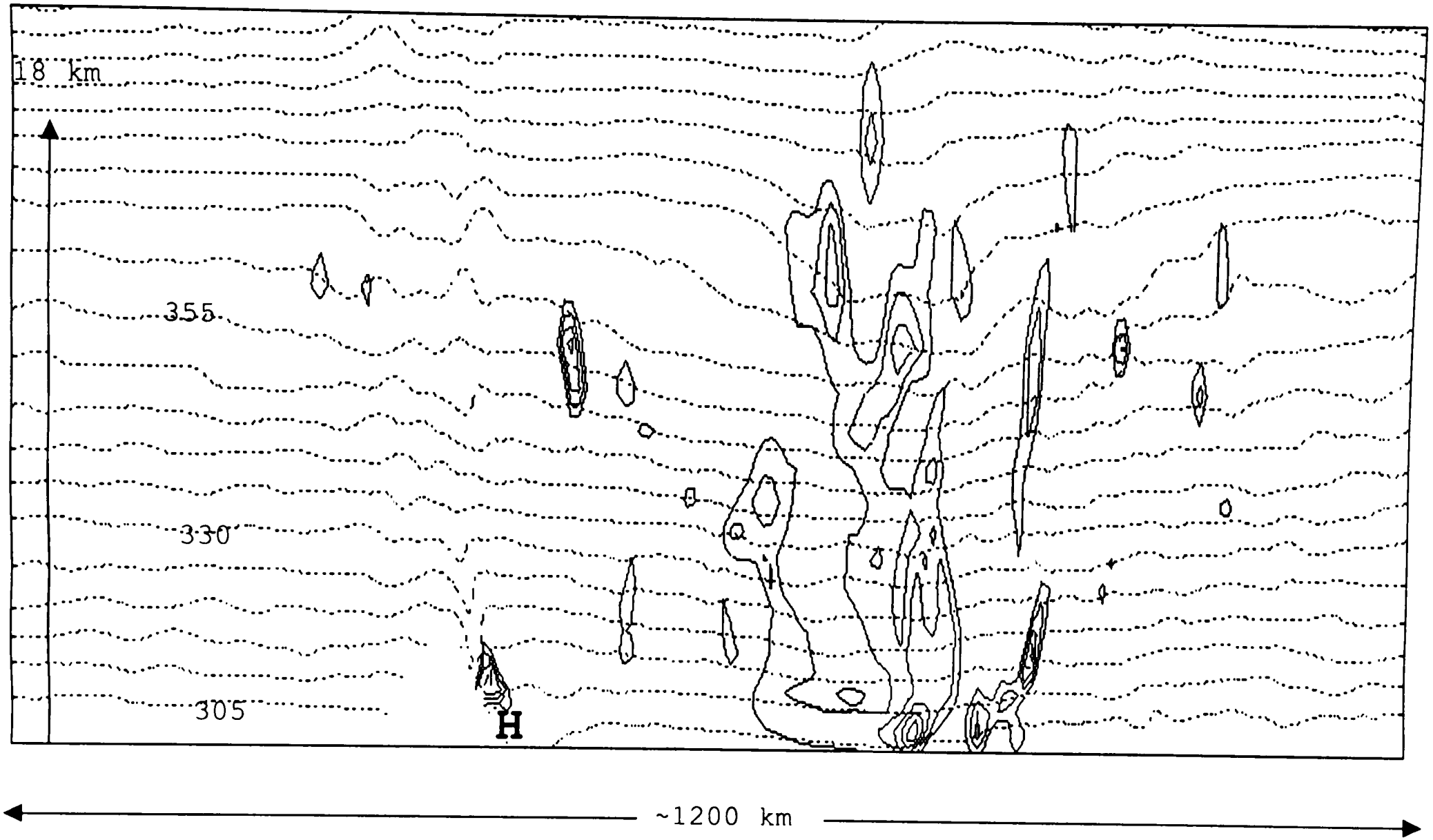


Figure 5.22. Same as Figure 5.21 but for 2200 UTC 30 July 1996.

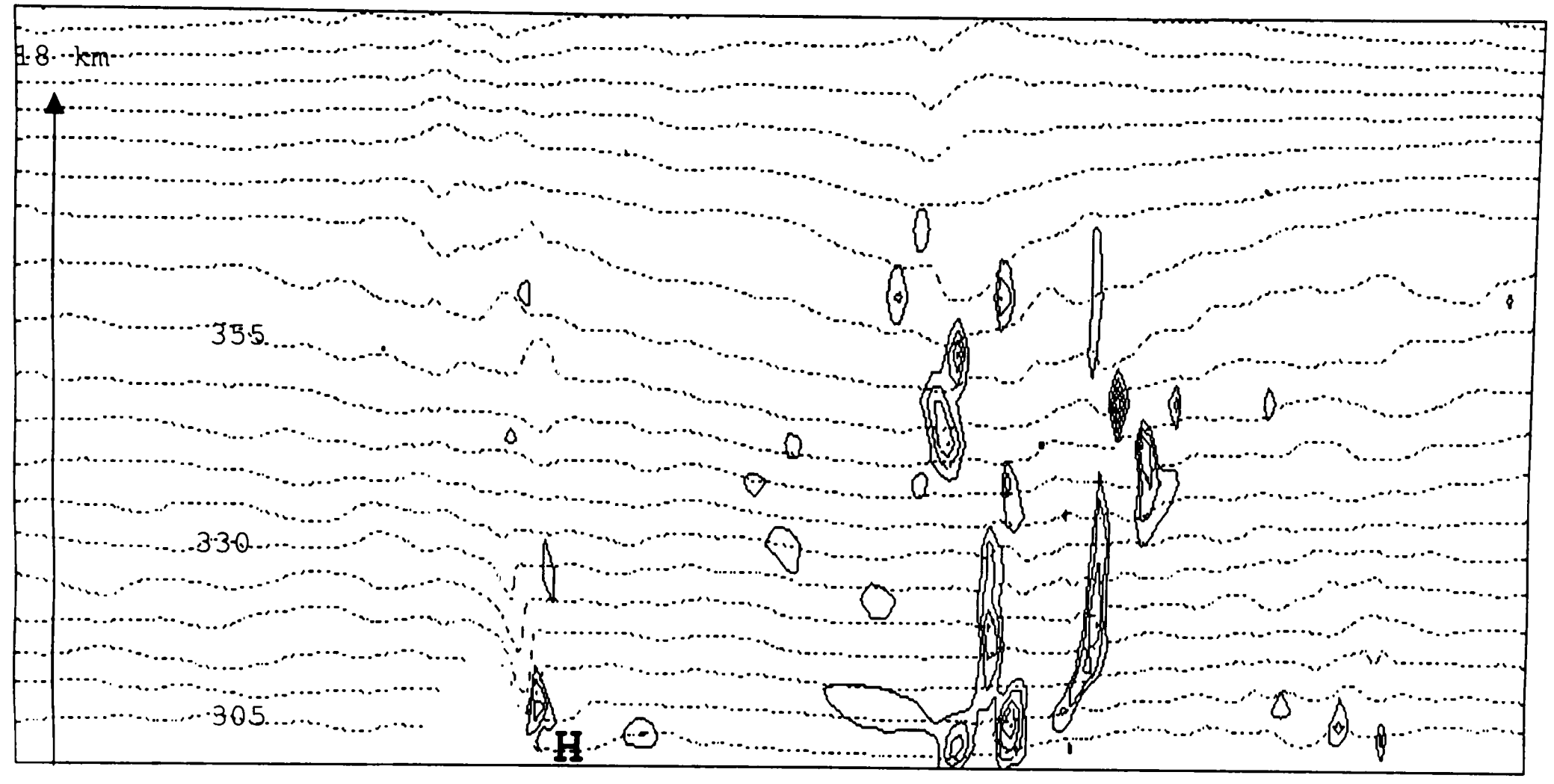


Figure 5.23. Same as Figure 5.21 but for 0000 UTC 31 July 1996.

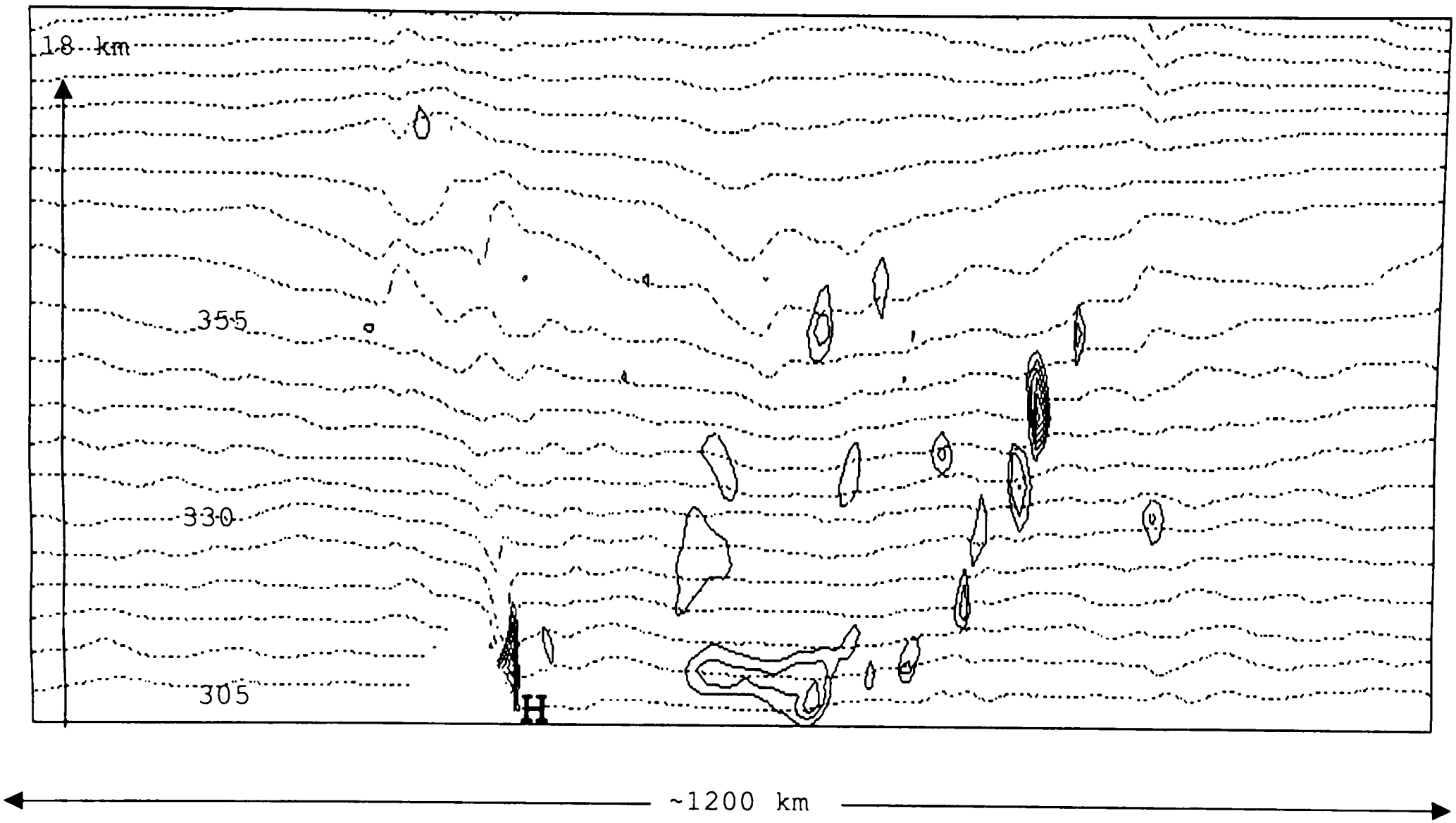


Figure 5.24. Same as Figure 5.21 but for 0200 UTC 31 July 1996.

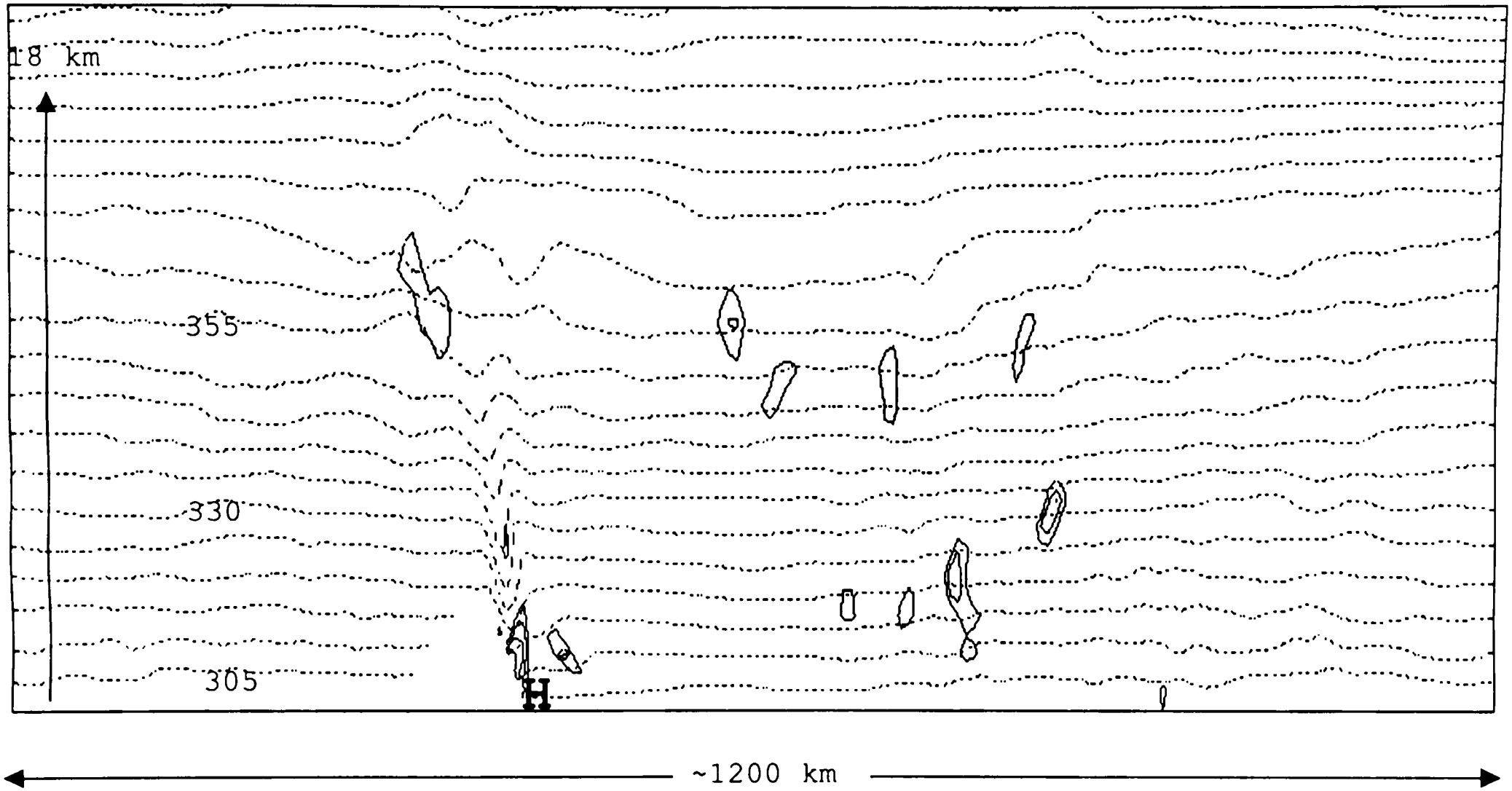


Figure 5.25. Same as Figure 5.21 but for 0400 UTC 31 July 1996.

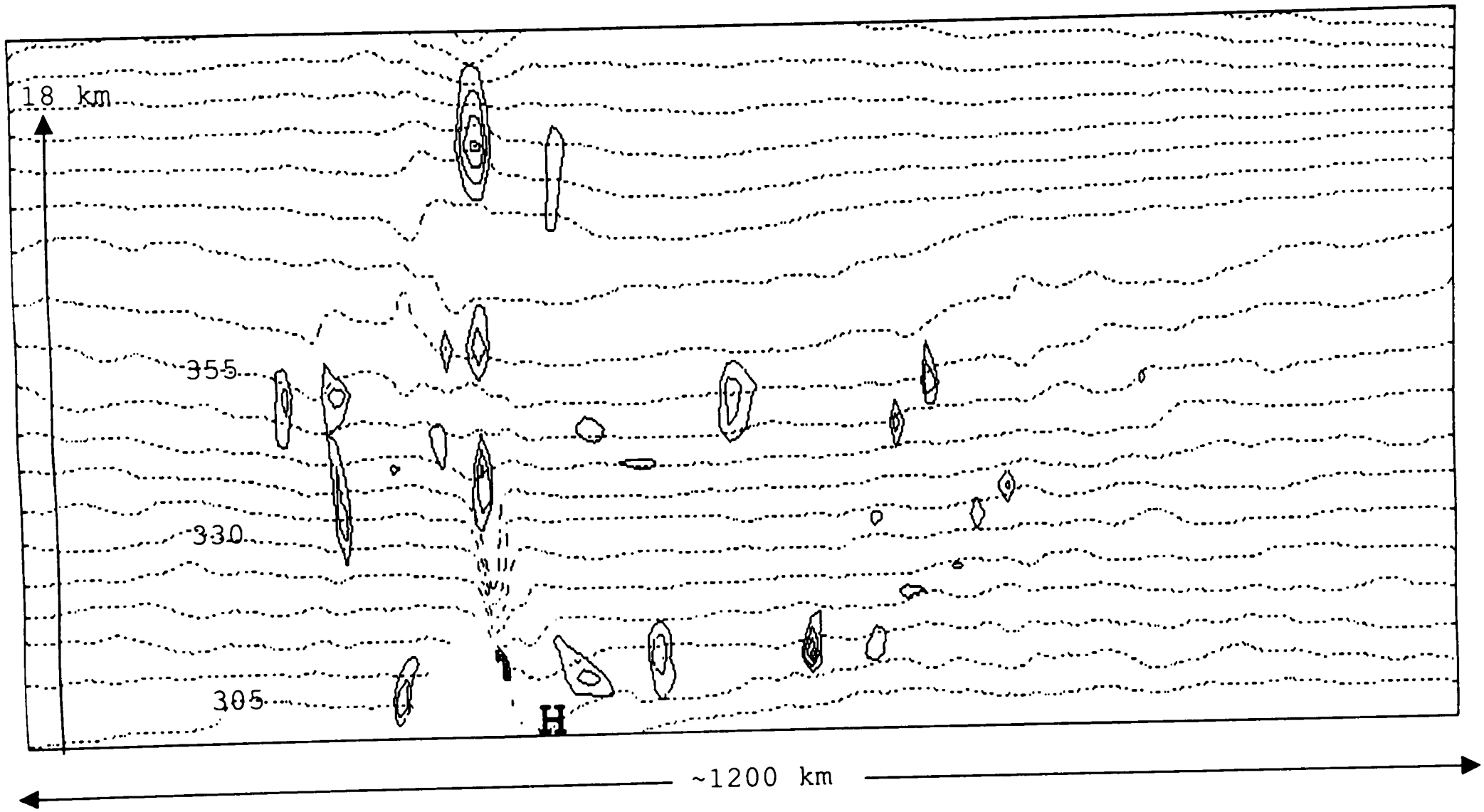


Figure 5.26. Same as Figure 5.21 but for 0600 UTC 31 July 1996.

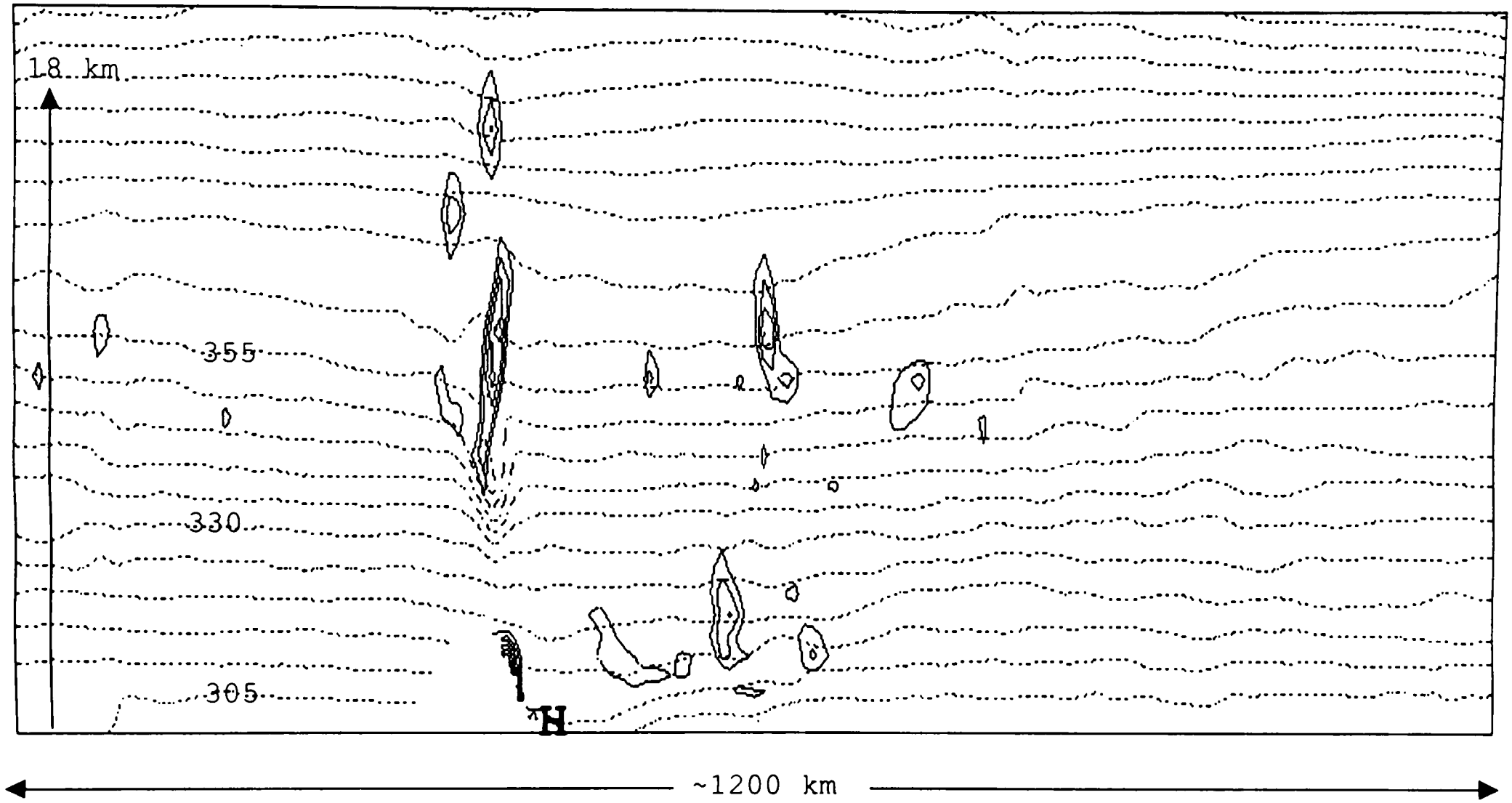


Figure 5.27. Same as Figure 5.21 but for 0800 UTC 31 July 1996.

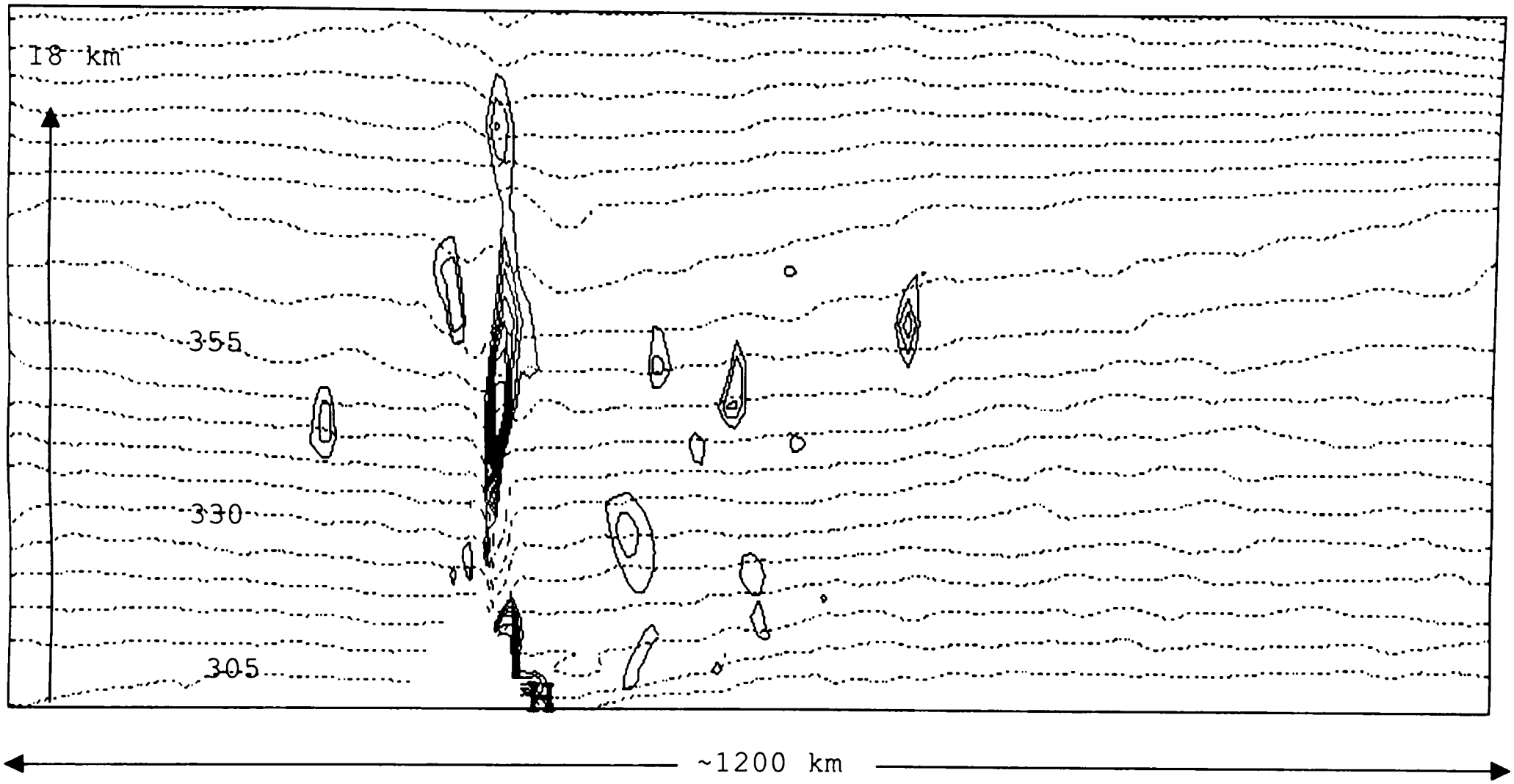


Figure 5.28. Same as Figure 5.21 but for 1000 UTC 31 July 1996.

little change in AV, with positive PV production ceasing as the typhoon traverses the island.

# CHAPTER 6

# CONCLUSIONS AND RECOMMENDATIONS

## 6.1 Conclusions

Based upon the vertical motion and PV analysis performed on the MM5 simulation of Supertyphoon Herb's interaction with Taiwan's CMR, several conclusions were reached. They are discussed below:

1. A "zone of transition" was found to occur some four to six hours prior to landfall in the symmetrical structure and magnitude of the vertical motion fields associated with the TC. It was during this transition period that most significant weakening of the typhoon was noted. This period was also found to coincide with the westerly flow associated with the TC first traversing and interacting with the steep terrain of the CMR. When compared to a conceptual model of a mature hurricane, the west side main inflow region was found to be cut off, followed by a reduction of the main outflow and spiral rainband regions. Significantly drier air was found to advect into mid-levels on the eastern side of the typhoon. Trajectory calculations performed on the most intense updraft regions determined air parcels typically originated from higher and drier source regions as the typhoon neared

the CMR. This was especially true for air parcels on the eastern half of the typhoon. It was determined that the overall decline in the intensity and structure of the TC was due to a combination of weakening on both the east and west sides from these different mechanisms.

2. The positive PV structure and symmetry associated with the TC were found to correlate well with past research. The strongest positive PV areas compared quite well with the main outflow regions in the convective eyewall as identified through the conceptual model. A westward tilt of the positive PV anomaly above 7 km was found to exist until the typhoon entered the "zone of transition" whereby both its symmetrical nature and PV intensity were reduced. The transition zone for the positive PV anomaly was identified slightly prior (about two to three hours) to that of the vertical motion fields. No definitive reason was determined for this occurrence.

3. Beginning at about 2000 UTC, when the typhoon was some 500 km to the east of the terrain feature, mesoscale concentrations of positive PV were generated over and on the lee side of the CMR. These regions were termed positive PV "bull's-eyes" due to their circular, concentric shape. Terrain generation and not redistribution within

the storm environment was determined to be the chief mechanism in their production, as a "clear channel" of PV-free air was found to exist between the TC and the mountain. The bull's-eyes were shown to form parallel to the mean flow and perpendicular to the height contours of terrain at both levels analyzed; with the 3 km level the most pronounced in terms of PV magnitude. The bull's-eyes were then observed to advect into the typhoon environment. Cross sections of potential temperature and absolute vorticity subjectively revealed that the vertical potential temperature change $(\partial(\mathrm{THE})/\partial z)$ contributed more to the positive PV on the lee side of the CMR than did the absolute vorticity.

4. Through plots of vertical motion and cloud water content, the positive PV bull's-eyes were found to exist in regions of the strongest upward motion (greater than 1.5 m $s^{-1}$ as a loose threshold). This was true both within the typhoon environment as well as over the terrain feature.

5. Time series of absolute and potential vorticity, vertical potential temperature change and upward motion on the northern, southern and eastern side of the CMR display an overall positive correlation between the parameters. In terms of positive PV generation, each location depicted a

slightly different scenario. Based on horizontal plots and confirmed with the time series analysis, the southern lee side probe location appeared to be the favored region for positive PV generation. The southern probe time series at 1 km verifies this assertion, with several undulations from 0400 to 1200 UTC suggesting generation. Both the north and east probes were relatively close to the typhoon, and while not in a favored PV generation location (per horizontal plots) did display an increase of all parameters after 0600 UTC. This was deemed the result of the proximity of the probes to the typhoon itself and not representative of any positive PV generation.

## 6.2 Recommendations

While the conclusions noted here are merely "observations" or documentation and examination of the model output, little in the way of effects on the structure and environment of the TC is given. A major limitation of this study was the lack of mobility with the data provided. In order to gain further insight into the effects of terrain generated positive PV on the TC environment, further work must be completed with additional case studies. A PV budget analysis with diabatic heating rate

calculations as well as frictional effects of the terrain must be included for a complete and accurate understanding.

Completion and comparison of MM5 sensitivity runs neglecting frictional effects, changing terrain height and orientation relative to the TC, or storm strength itself may prove invaluable to this cause.

Another unanswered question deals with the advection of the positive PV bull's-eyes into the storm environment. Do these features aid in decreasing the strength and intensity (and if so, how?) or assist the TC from becoming absolutely broken down by the terrain? Of interest as well is the magnitude and patterns of positive PV generation on the eastern slopes of the CMR. Does generation occur (and to what extent?) as the eastern half of the typhoon traverses the island and winds become perpendicular to the terrain? This was not addressed in this study.

Finally, how does the zone of transition change with increasing (decreasing) TC intensity or increased (decreased) terrain height? There remain numerous questions to be answered that stem from this study. Further research in this area is necessary in order that a deeper insight into the TC interaction with a terrain feature is better understood.

# LIST OF REFERENCES


Bender, M.A., R. Tuleya, and Y. Kurihara, 1985: A Numerical Study of the Effect of a Mountain Range on a Landfalling Tropical Cyclone. *Monthly Weather Review*, **113**, 567-582.

Bender, M.A., R. Tuleya, and Y. Kurihara, 1987: A Numerical Study of the Effect of Island Terrain on Tropical Cyclones. *Monthly Weather Review*, **115**, 130-155.

Brand, S., and S. W. Blelloch, 1974: Changes in the Characteristics of Typhoons Crossing the Island of Taiwan. *Monthly Weather Review*, **102**, 708-713.

Chang, S., 1982: The Orographic Effects Induced by an Island Mountain Range on Propagating Tropical Cyclones. *Monthly Weather Review*, **110**, 1255-1270.

Dudhia, J., D. Gill, Y.-R. Guo, D. Hansen, and K. Manning, no date: *PSU/NCAR Mesoscale Modeling System Tutorial Class Notes and User's Guide: MM5 Modeling System Version 2.* National Center for Atmospheric Research, Boulder, CO.

Fung, K., 1997: Activity of 1996 Tropical Cyclones in the North Pacific. http://rossby.metr.ou.edu/~spark/AMON/v1_n1/Ken_TC.html.

Holton, J., 1992: *An Introduction to Dynamic Meteorology, Third Edition;* Academic Press, 1992, 511 pp.

Molinari, J., and D. Vollaro, 1990: External Influences on Hurricane Intensity Part II: Vertical Structure and Response of the Hurricane Vortex. *Journal of the Atmospheric Sciences*, **47**, 1902-1918.

Lin, Y.-L., J. Han, D.W. Hamilton, and C.-Y. Huang, 1999: Orographic Influence on a Drifting Cyclone. *Journal of the Atmospheric Sciences*, **56**, 534-562.

Liu, Y., Zhang, D.-L., and M. K. Yau, 1999: A Multiscale Numerical Study of Hurricane Andrew (1992) Part II: Kinematics and Inner-Core Structures. *Monthly Weather Review*, **127**, 2597-2616.

May, P., and G. Holland, 1999: The Role of Potential Vorticity Generation in Tropical Cyclone Rainbands. *Journal of the Atmospheric Sciences*, **56**, 1224-1228.

Molinari, J., M. Dickinson, D. Vollaro, and S. Skubis, 1997: Potential Vorticity, Easterly Waves and Tropical Cyclogenesis. *Monthly Weather Review*, **125**, 2699-2708.

Shapiro, L., and J. Franklin, 1995: Potential Vorticity in Hurricane Gloria. *Monthly Weather Review*, **123**, 1465-1475.

Shapiro, L., 1996: The Motion of Hurricane Gloria: A Potential Vorticity Diagnosis. *Monthly Weather Review*, **124**, 2497-2508.

Stolelinga, M.T., 1996: A Potential Vorticity Based Study of the Role of Diabatic Heating and Friction in a Numerically Simulated Baroclinic Cyclone. *Monthly Weather Review*, **128**, 208-228.

Wu, C.-C., and K. Emanuel, 1995: Potential Vorticity Diagnostics of Hurricane Movement. Part I: A Case Study of Hurricane Bob (1991). *Monthly Weather Review*, **123**, 69-92.

Wu, C.-C. and Y. Kurihara, 1996: A Numerical Study of the Feedback Mechanisms of Hurricane-Environment Interaction on Hurricane Movement from the Potential Vorticity Perspective. *Journal of the Atmospheric Sciences,* **53**, 2264-2282.

Wu, C.-C., Y.-K. Kuo, W. Wang, and T.-Z. Yen, 1998: Numerical Simulation of Typhoon Herb (1996) Using MM5. Preprints, *23rd Conf. on Hurricanes and Tropical Meteorology,* Dallas, TX, Amer. Meteor. Soc., 1008-1011.

Wu, C.-C., and Y.-H. Kuo, 1999: Typhoons Affecting Taiwan: Current Understandings and Future Challenges. *Bull. Amer Meteor. Soc.,* **80**, 67-80.

Wu, L., and B. Wang, 2000: A Potential Vorticity Tendency Diagnostic Approach for Tropical Cyclone Motion. *Monthly Weather Review,* **128**, 1899-1911.

Yeh, T.-C., 1993: Interaction of Typhoons with the Taiwan Orography Part I: Upstream Track Deflections. *Monthly Weather Review,* **121**, 3193-3211.

Zehnder, J. A., 1993: The Influence of Large-Scale Topography on Barotropic Vortex Motion. *Journal of the Atmospheric Sciences,* **50**, 2519-2532.

# PERMISSION TO COPY

In presenting this thesis in partial fulfillment of the requirements for a master's degree at Texas Tech University or Texas Tech University Health Sciences Center, I agree that the Library and my major department shall make it freely available for research purposes. Permission to copy this thesis for scholarly purposes may be granted by the Director of the Library or my major professor. It is understood that any copying or publication of this thesis for financial gain shall not be allowed without my further written permission and that any user may be liable for copyright infringement.

Agree (Permission is granted.)

_____ _____

Student Signature Date

Disagree (Permission is not granted.)

_____ _____

Student Signature Date